Ice, Cloud, and land Elevation Satellite-2 (ICESat-2) Project

Algorithm Theoretical Basis Document (ATBD) for Along Track Inland Surface Water Data
ATL13 Release 006

April 29, 2023

by

Michael Jasinski, PI	*NASA GSFC*
Jeremy Stoll	*SSAI*
David Hancock	*SSAI*
John Robbins	*Craig Technologies, Inc.*
Jyothi Nattala	*SSAI*
James Morison	*University of Washington*
Benjamin Jones	*University of Alaska*
Michael Ondrusek	*NOAA STAR*
Tamlin Pavelsky	*University of North Carolina*
Christopher Parrish	*Oregon State University*
Claudia Carabajal	*SSAI*

This document may be cited as:

Jasinski, M., J. Stoll, D. Hancock, J. Robbins, J. Nattala, J. Morison, B. Jones, M. Ondrusek, T. Pavelsky, C. Parrish, and C. Carabajal (2023). *ICESat-2 Algorithm Theoretical Basis Document (ATBD) for Along Track Inland Surface Water Data, ATL13, Version 6*. ICESat-2 Project, DOI: 10.5067/03JYGZ0758UL.

Goddard Space Flight Center
Greenbelt, Maryland

Abstract

This document describes the theoretical basis of the algorithms employed in the derivation and processing of the ATL13 Along Track Inland Surface Water Data products for ICESat-2, Release 5. These level L3A data products are reported at the continuous, along track rate for each ICESat-2 water body crossing. The ATL13 ATBD includes descriptions of the data products and product parameters, detailed algorithm steps required for the retrieval of those products, a summary of other ancillary ICESat-2 products required in the processing, and a calibration and validation plan. Updates to previously reported products and the addition of new products may be included.

Note that a new higher level L3B product containing the means of the ATL13 along-track products is described and reported in a separate ATBD entitled *Mean Inland Surface Water Data (ATL22)*.

Citation for this ATL13 ATBD Release 006 document:

Jasinski, M., Stoll, J., Hancock, D., Robbins, J., Nattala, J., Pavelsky, T., Morrison, J., Jones, B., Ondrusek, M., Parrish, C., Carabajal C., and the ICESat-2 Science Team (April, 2023). *ICESat-2 Algorithm Theoretical Basis Document (ATBD) for Along Track Inland Surface Water Data, ATL13, Release 6*. ICESat-2 Project, NASA Goddard Space Flight Center, Greenbelt, MD, 178pp. DOI: 10.5067/03JYGZ0758UL

Citation when using ATL13 Inland Water Rel 006 data products from NSIDC:

M. Jasinski, J. Stoll, D. Hancock, J. Robbins, J. Nattala, T. Pavelsky, J. Morrison, B. Jones, M. Ondrusek, C. Parrish, C. Carabajal and the ICESat-2 Science Team, 2023. *ATLAS/ICESat-2 L3A ICESat-2 Along Track Inland Surface Water Data, Release 6*. [Indicate subset used]. Boulder, Colorado USA. NASA National Snow and Ice Data Center Distributed Active Archive Center. DOI:10.5067/ATLAS/ATL13.006

*Note: The name of the ATL13 product (including both the ATBD documentation and the NSIDC data products) were changed to *ATL13 Along Track Inland Surface Water Data* beginning with Release 4. This name change was necessary to more accurately reflect the expanded suite of ATL13 products beyond just water height. It further distinguishes the ATL13 Level 3A continuous along track products from the newly created higher Level 3B *ATL22 Mean Inland Surface Water ATBD* and data being published as a separate product.

Acknowledgements

We gratefully acknowledge the numerous individuals who have made important contributions at various levels toward the development of the ATL13 Inland Water Data Products:

Tom Wagner, *NASA Headquarters*
Thorsten Marcus, *NASA Headquarters*
Jared Entin, *NASA Headquarters*
Woody Turner, *NASA Headquarters*
Tom Neumann, *NASA GSFC*
Lisa Callahan, *NASA*
Jeffrey Lee, *SGT, Inc.*
Kelly Brunt, *University of Maryland*
Kaitlin Harbeck, *SGT, Inc.*
Steve Palm, *SSAI*
Sinead Farrell, *University of Maryland*
Ron Kwok, *NASA JPL*
Ben Smith, *University of Washington*
Christopher Hiemstra, *CRREL*
Bill Cook, *NASA GSFC*
Christopher Arp, *University of Alaska*
Sabrina Delgado-Arias, *SSAI*
Bea Csatho, *University of Buffalo*
Yongwei Sheng, *UCLA*
Huilin Gao, *University of Texas A&M*
Bernhard Lehner, *McGill University*
Anita Brenner, *SGT, Inc.*
Yao Li, *University of Texas A&M*
Jeffrey Danielson, *USGS*
Eric Stengel, *NOAA STAR*
Jeffrey Gerber, *SGT, Inc.*
Steven Kuo-Hsin Tseng, *National Central U., Taiwan*
Hsiao-Jou Hsu, *National Central U., Taiwan*
Lori Magruder, *University of Texas ARL*
David Harding, *NASA GSFC*
Charon Birkett, *NASA GSFC*
Jeremy Kasper, *University of Alaska*
Krista Bartz, *US National Parks Service*
Mark Carroll, *NASA GSFC*
Jennifer Wozencraft, *JALBTCX*
Richard Kelly, *University of Waterloo*

CM Foreword

This document is an Ice, Cloud, and Land Elevation (ICESat-2) Project Science Office controlled document. Changes to this document require prior approval of the Science Team ATBD Lead or designee. Proposed changes shall be submitted in the ICESat-2 Management Information System (MIS) via a Signature Controlled Request (SCoRe), along with supportive material justifying the proposed change.
In this document, a requirement is identified by “shall,” a good practice by “should,” permission by “may” or “can,” expectation by “will,” and descriptive material by “is.”

Questions or comments concerning this document should be addressed to:
ICESat-2 Project Science Office
Mail Stop 615
Goddard Space Flight Center
Greenbelt, Maryland 20771

Preface

This document is the Release 6 Algorithm Theoretical Basis Document for the ATL13 Inland Water Data Products processing implemented at the ICESat-2 Science Investigator-led Processing System (SIPS). It supersedes all previous ATL13 Versions. The SIPS supports the ATLAS (Advance Topographic Laser Altimeter System) instrument on the ICESat-2 Spacecraft and encompasses the ATLAS Science Algorithm Software (ASAS) and the Scheduling and Data Management System (SDMS). The science algorithm software produces Level 0 through Level 3A&B standard data products as well as the associated product quality assessments and metadata information.

The ICESat-2 Science Team, in support of the ICESat-2 Project Science Office (PSO), assumes responsibility for this document and updates it, as required, as algorithms are refined or to meet the needs of the ICESat-2 SIPS. Reviews of this document are performed when appropriate and as needed updates to this document are made. Changes to this document will be made by complete revision.

Changes to this document require prior approval of the Change Authority listed on the signature page. Proposed changes shall be submitted to the ICESat-2 PSO, along with supportive material justifying the proposed change.

Questions or comments concerning this document should be addressed to:
Thomas Neumann, ICESat-2 Project Scientist
Mail Stop 615
Goddard Space Flight Center
Greenbelt, Maryland 20771

Review/Approval Page

Prepared by:

Michael F. Jasinski
ICESat-2 Science Team Lead for ATL13 Inland Surface Water Data
Hydrological Sciences Laboratory, Code 617
NASA Goddard Space Flight Center
Greenbelt, MD 20771

Reviewed by:

Lori Magruder
ICESat-2 Science Team Lead
Applied Research Laboratories
University of Texas, Austin

Tom Neumann
ICESat-2 Project Scientist
Cryospheric Sciences Lab, Code 615
NASA Goddard Space Flight Center
Greenbelt, MD

Change History Log

Revision Level	Description of Change	SCoRe No.	Date Approved
1.0	**ATL13 Release 001**, Initial Release		May 28, 2019
2.0	**ATL13 Release 002** -Replaced GLWD with HydroLAKES. -Water bodies analyzed include: i) All transected lakes and reservoirs > 0.1 km^2 ii) Estuaries and bays iii) 7 km global coast buffer. - Implemented coarse bottom bathymetry algorithm for all water bodies, cloudiness and water clarity permitting. - Implemented dynamic shore finding algorithm		October 1, 2019
3.0	**ATL13 Release 003** -First photon bias (FPB) correction implemented using ATLAS CAL-19 procedure. -Wind speed estimated from standard deviation of water surface (*met_wind10_atl13*). -Updated water body shape file (ANC20) to include global river shapes. - Cloud confidence flag parameters retrieved from ATL09 and rescaled ATL13 at short segments.		March 1, 2020

	ATL13 Release 003 (Cont'd) - Added downscaled ATL09 input wind vector components at 10m height (*met_u10m, met_v10m*). -Included bottom in determining the minimum height to calculate subsurface deconvolution. -Updated threshold counts of photons within short segment histogram multimode. -Included max available ATL03 geolocation segments outside of water mask edges, in height computation. -Added water body transect parameters; *transect_id, sseg_start_lat, sseg_start_lon, sseg_end_lat, sseg_end_lon* and *segment_azimuth*. -Corrected sign in EM bias (*H_bias_EM*) calculation. -Updated expression for orthometric water surface height and depth when *H_bias_EM* is designated as invalid and *H_bias_fit* designated as valid, to omit invalid term. -Implemented number of short segments to be designated as anomalous due to near-shore influences (*shore_buffer*). -Added surface (skin) temperature (*met_ts_atl09*) interpolated from ATL09 inputs at 1 Hz and 25 Hz rate. -Added NOAA snow/ice flag (*snow_ice_atl09*) from interpolation of ATL09. -Added writeup on MABEL Lake Mead bathymetry		March 1, 2020

	ATL13 Release 003 (Cont'd) - Added downscaled ATL09 input wind vector components at 10m height (met_u10m, met_v10m). -Included bottom in determining the minimum height to calculate subsurface deconvolution. -Updated threshold counts of photons within short segment histogram multimode.		
4.0	**ATL13 Release 004** -Fixed adjustment in mean height after deconvolution due to an earlier coding error Eqn 4.23a1. - Added first photon bias (FBC) correction to the estimate of true height as described in Eqns 4.23a-c, Section 4.7.3.6. - Added best publicly available DEM to ATL13 output. - Added quality flags for Clouds, Snow and Ice and Temperature. - Added H adj flag associated with impact of deconvolution surface height -Corrected the algorithm to keep the designated number of photons per short segment, and then start the next short segment with the next photon which could be from the same shot as last short segment's photon. - Input parameters needed to drive algorithms added to Chapter 5 (Table 15). - Output parameters table for ATL13 products updated (Tables 5.2 and 5.3).		April 1, 2021

	ATL13 Release 004 Cont'd - The coding was corrected to subtract the EM bias and the FPB corrections where appearing in Equations 4.23. - Coding corrected to compute along track slope. - Updated the description of the product output parameter segment_geoid to reference water surface heights above WGS84 reference ellipsoid (*ht_water_surf*) from the tide-free system to the mean-tide system (no impact on output water height data product). -Corrected computation of spectral width and updated corresponding quality flag. -Corrected algorithm to not skip out of a water body when due to insufficient photons within the subsurface. -Added additional granularity to the sseg_length quality flag. - Increased maximum range of alpha attenuation coefficient to 1.2. - Implemented exclusion of TEP photons when forming ATL13 short segments. - Added short segment fractions of near and full saturation. - Filtered water body crossings which include geosegments whose composite POD/PPD flag is non-zero, invalidating possibly degraded geolocation solutions. - Updated weak beam interpolation of ATL09 atmospheric profile source data to be aligned by along-track distance and not time.		

	ATL13 Release 004 Cont'd - Developed a new anomalous subgroup relevant to be used in new ATL22 mean surface water products. -Developed trigger flags for eventual use in ATL22 ATBD.		
5.0	**ATL13 Release 005** -Modified creation of short segment length to be based on a variable number of photons depending on water body type. Employs 75 photons for rivers. - Includes analysis of the partial short segments at the very end of a transect that did not include sufficient photons, and were omitted in previous versions. - Updated subsurface refraction correction to also include lat/long position of bottom location. - Updated subsurface analysis to include assumed fresh and salt water indices based on water body type. - Added POD/PPD Flags that indicates quality of input geolocation products for the short segments. - Improved deconvolution algorithm of subsurface profile by expanding the possible range over which α and β are fit.		August 19 2021

	ATL13 Release 005 (Cont'd) - Updated available external links for ATL13 height product validation - Corrected typo on Table 1-1 to read "7 km" shore buffer -Added count in output of signal photons in full and partial non-anomalous and anomalous short segments		
6.0	**ATL13 Release 006**		March 10 2023
	-Modified deconvolution reflectance profile of the integrated Gaussian and subsurface components in Eqn 4.11 and 4.12. Added "2" inside the exponential term to accommodate two-way attenuation. Simplified the backscatter amplitude factor to make analogous to the lidar equation.		
	Expanded iteration range of subsurface parameters within deconvolution scheme, added quality flags		
	Added quality flag for range of surface standard deviation is Section 4.8.1.12		
	-Defined end of partial short segments as the final signal photon, as identified in Section 4.5.5.1		
	-To avoid inadvertently capturing subsurface photons associated with bottom reflection and machine error, such photons are further screened and removed from processing using a mirroring approach applied to the water surface in Section 4.5.5.2. and Section 5.3.C.		
	-Added flags identifying the range of of the Gaussian fit in Section 4.1.8.12.		
	-Included Plain Language Summary in Chapter 5, ALGORITHM IMPLEMENTATION.		
	-Replaced "crossing-number" algorithm with "winding number" algorithm for better determination of ICESat-2 transects within the Inland Water mask shapes.		
	Expanded Table 5-3 Intermediate Variables List		April 1, 2023
	Added note on omission of c1 in deconvolution equations 4.11 and 4.12 affecting estimation of α		April 28, 2023

List of TBDs/TBRs

Item No.	Location	Summary	Ind./Org.	Due Date

Table of Contents

List of Figures

List of Tables

1.0 INTRODUCTION

1.1 Purpose

The L3A Algorithm Theoretical Basis Document (ATBD) describing the Along Track Inland Surface Water Data Product, consists of the Release 6 ATL13 processing algorithms applied to photon cloud observations acquired by the ICESat-2 ATLAS sensor. This newest ATL13 Rel 6 is applied to, and reprocesses, all ICESat-2 Inland Water observations from launch to present. It therefore supersedes all previous ATL13 versions. (E.g. Release 001, Jasinski et al., October 2019a; Release 2, 2019b; Rel 005, Jasinski et al, 2021a, 2021b). ATL13's name was modified in Ver 4 to emphasize that products include not only the high-resolution, along track surface heights across the water body transect, but also a suite of other derived products including wave height, subsurface beam attenuation, wind speed, and bottom elevation when when water clarity permits.

Also note that a higher level L3B companion product containing the means of the ATL13 along-track products has been developed and reported in a separate ATBD entitled "*Mean Inland Surface Water Data (ATL22)*". The difference between the along track ATL13 products and the mean ATL22 products is graphically illustrated in Figure 1-1 below.

This ATL13 ATBD includes background (Chapter 2), details of the theoretical underpinnings of the algorithms together with their testing on ATLAS or ATLAS prototype data (Chapters 3 and 4), a list of the specific ATL13 output product tables (Chapter 5), and several calibration and validation background and opportunities (Chapter 6). Since this ATBD is refined over time due to improvement to the algorithms, a summary of the principal updates to each version or release is also provided in the Change Log and in Chapter 1.

The complete documentation of the ATL13 product including the most recent version of this ATL13 ATBD, Data Product Known Issues, and data acquisition, are available at link https://nsidc.org/data/atl13.

1.2 Justification and Goals of ICESat-2 Inland Water Body Height Data Products

The Inland Water Body Height Data Product is computed as part of an integrated set of six ICESat-2 geophysical products that also include ice sheets, sea ice, atmosphere, vegetation structure and oceans. Climate variability is significantly impacting Arctic hydrology with regard to permafrost dynamics, lake extent and volume, snow accumulation and melt, and basin runoff (Rowland et al, 2010; Hinzman et al. 2005; IPCC, 2014; Serreze et al, 2000; Peterson et al., 2002). Consequently, time series observations of inland water heights and stores will allow a more complete understanding of the linkages among polar system dynamics and provide closure to the pan-Arctic water balance.

Inland water bodies are characterized by contiguous areas of surface water, with irregular disparate shapes spanning a wide range of sizes from small ponds to large inland lakes of $O(10^4)$ sq. km. Compared to open oceans, they possess distinct characteristics. For instance, they contain smaller waves and correspondingly higher water surface reflectances due to lower surface roughness. Inland water bodies are also prone to set-up on the lee shore with wave heights that are fetch dependent. Reflectance characteristics also differ. Inland water bodies generally exhibit unique color signatures and volume scattering characteristics of the local river basin, and greater mineral turbidity due to local runoff events and also under windy conditions due to resuspension of bottom sediments. Shallow depths of many inland and near shore water bodies result in a possible bottom backscatter component to the overall integrated water reflectance. In many regions of the world, seasonal weather and climate extremes can affect a water body's areal extent, which must be accounted for in the height retrieval algorithm.

ICESat-2 observations of inland water will i) enable understanding of the contribution of high-latitude hydrology and lake storage to the pan-Arctic water balance, and contribute to its associated impact on freshwater fluxes into the Arctic Ocean, melting snow, ocean salinity and circulation, methane distribution, ecosystem dynamics, and geomorphology, including the role of small lakes, ii) enable other science and application studies that may benefit from global, seasonal, high resolution Lidar observations of inland and near shore water body heights, such as shallow water bathymetry, and improved reservoir and water resources management, iii) provide geometric hydraulic properties for estimating stream discharge and lake storage/elevation/area relation, iv) serve as a high resolution calibration source for other radar altimeters, that generally perform poorly in ice covered lakes, and v) serve as an accurate high-resolution calibration for other radar altimeters, and provide synergy with the upcoming SWOT mission.

1.3 Definition of ATL13 Inland Water Body

An ATL13 inland water body is defined as a contiguous continental water body of the following types: lakes and reservoirs greater than about $0.1 km^2$, rivers greater than about 50-100m wide, transitional water including estuaries and bays, and a near-shore 7km buffer. In aggregate, the number of water bodies defined above is globally about 1.5 million. In ATL13, each water body is defined by a unique ID using publicly available masks and datasets. The project endeavors to include the most accurate and updated mask available, which also serves the advantage of being consistent with developments within future missions such as the Surface Water Ocean Topography (SWOT) mission.

An ICESat-2 transect is any portion of an ICESat-2 beam crossing over a single water body that is interrupted by land, say due to islands, bays, or peninsulas. A ICESat-2 crossing with no land interruptions would have a single transect. An ICESat-2 transect with a single island would have two transects. It is possible that an island interrupting one beam is not in the path of another beam. Therefore each of the six ICESat-2 beams may have a different transect on that particular crossing.

1.4 ATL13 Inland Water Along Track Data Product, Summary

The ATL13 data product provides the along-track water surface height products for each ATLAS beam. The principal products include the surface water height statistics (mean, standard deviation, slope), significant wave height, subsurface attenuation, and shallow bathymetry (when cloudiness and water clarity permit) as shown in Table 1-2. Additional secondary, supporting products are also computed as listed in Table 5-1. Release 5 data products were computed for global inland lakes greater to 0.10 km^2 traversed by ICESat-2 for which sufficient signal photons are recorded. While the domain of the ATL13 data product is global, the focus is on high-latitude terrestrial regions where the convergence of the ICESat-2 orbits provides spatially dense observations in the pan-Arctic region.

A schematic representation of the Inland Water Height data product is shown in Figure 1-1a. Each green segment represents an along track height, slope and rms product. The target reporting scales of the ATL13 Inland Water Height data product are relatively short segment lengths with a minimum S-signal photons (E.g. Short segments, S 100 signal photons for all water bodies except rivers (75), in order to observe as many small water bodies as practical. The precise photon count depends on the number and quality of observations extracted from the along-track aggregation of ATLAS observations that consist of signal and noise photons.

The frequency of water body crossings depends on the intersection of the water body mask and ICESat-2's orbital pattern that is characterized by a dual, latitude dependent observation strategy. For high latitude polar regions, mission requirements require that ICESat-2 repeats observations along the precisely established reference tracks, similar to ICESat-1. However, for all lower latitudes, ICESat-2 does not repeat during the first two years but rather implements s a systematic off-pointing mapping scenario. The frequency of observing a water body therefore depends also on its size and geographic location.

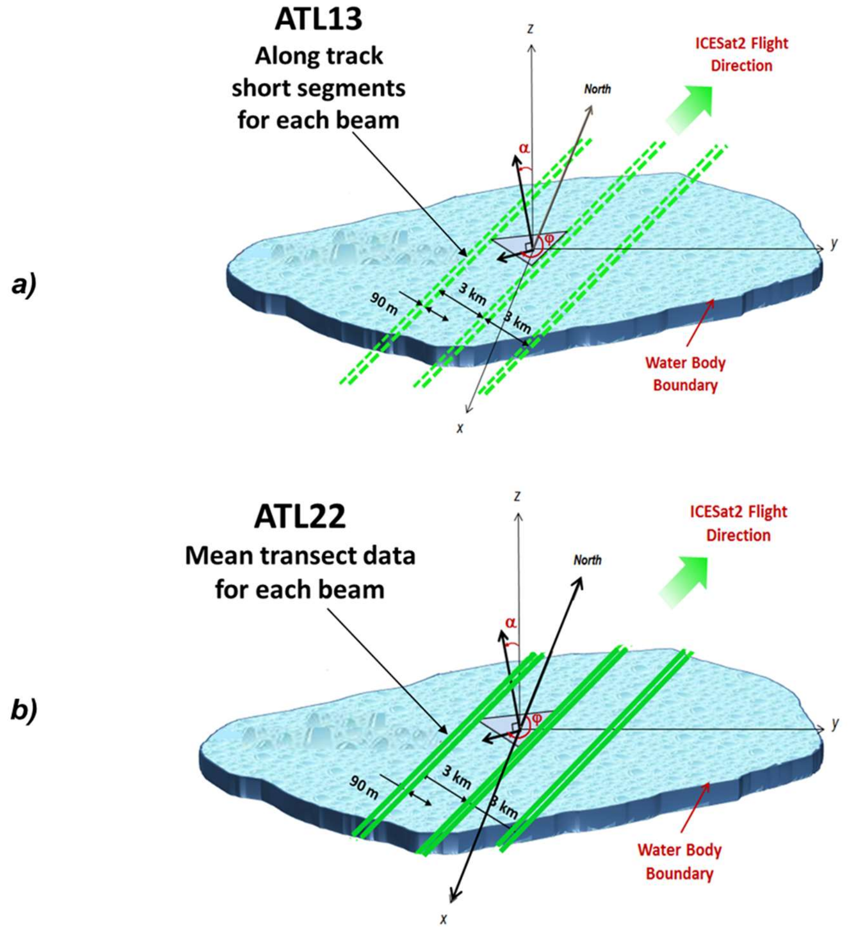

Figure 1-1 a) Schematic of principal ATL13 Inland Surface Water along track data products includes surface height statistics, subsurface attenuation, significant wave height (SWH) and coarse bottom topography. Height statistics are reported for variable segment lengths of 100 signal photons. Estimated accuracy is 5-8 cm per 100 signal photons. b) Comparison schematic of principal ATL22 Release 3 Mean Inland Surface Water data products to be available in mid- 2023.

ATL13 water bodies are identified by a set of polygons in shape-file format.

The ATL13 product draws primarily from the Level 2 ICESat-2 ATL03 product. ATL03 includes: i) Precise latitude, longitude, and height for every received photon, arranged by beam in the along-track direction, ii) photons classified as signal or background, and also by surface type (i.e., land ice, sea ice, land, ocean, inland water) including all geophysical corrections (e.g., Earth tides, atmospheric delay), and iii) photons segmented into several minute granules. Given the low reflectance of water compared to other land and sea ice targets, the rate of observed inland water surface signal photons ranges from about 0.5 to no more than several events per meter (pe/m), based on early analysis of the MABEL data over Lake Mead, Chesapeake Bay, and the near shore Atlantic Ocean coast (Jasinski et al., 2016) and also confirmed with recent analysis of ATLAS data since launch in September 2018. It is expected that statistically representative inland water heights can be calculated over distances of a minimum of 10 to 100 m, depending on atmospheric, solar, and water conditions.

1.5 ATL13 Along Track Inland Surface Water Data Products Summary (Releases 1 to 6)

The Inland Water Data Product is continually updated to include new features and capability. Table 1-1 summaries the evolving features of progression of the data product through Along Track Version 006 and Mean Track ATL22 Version 3.

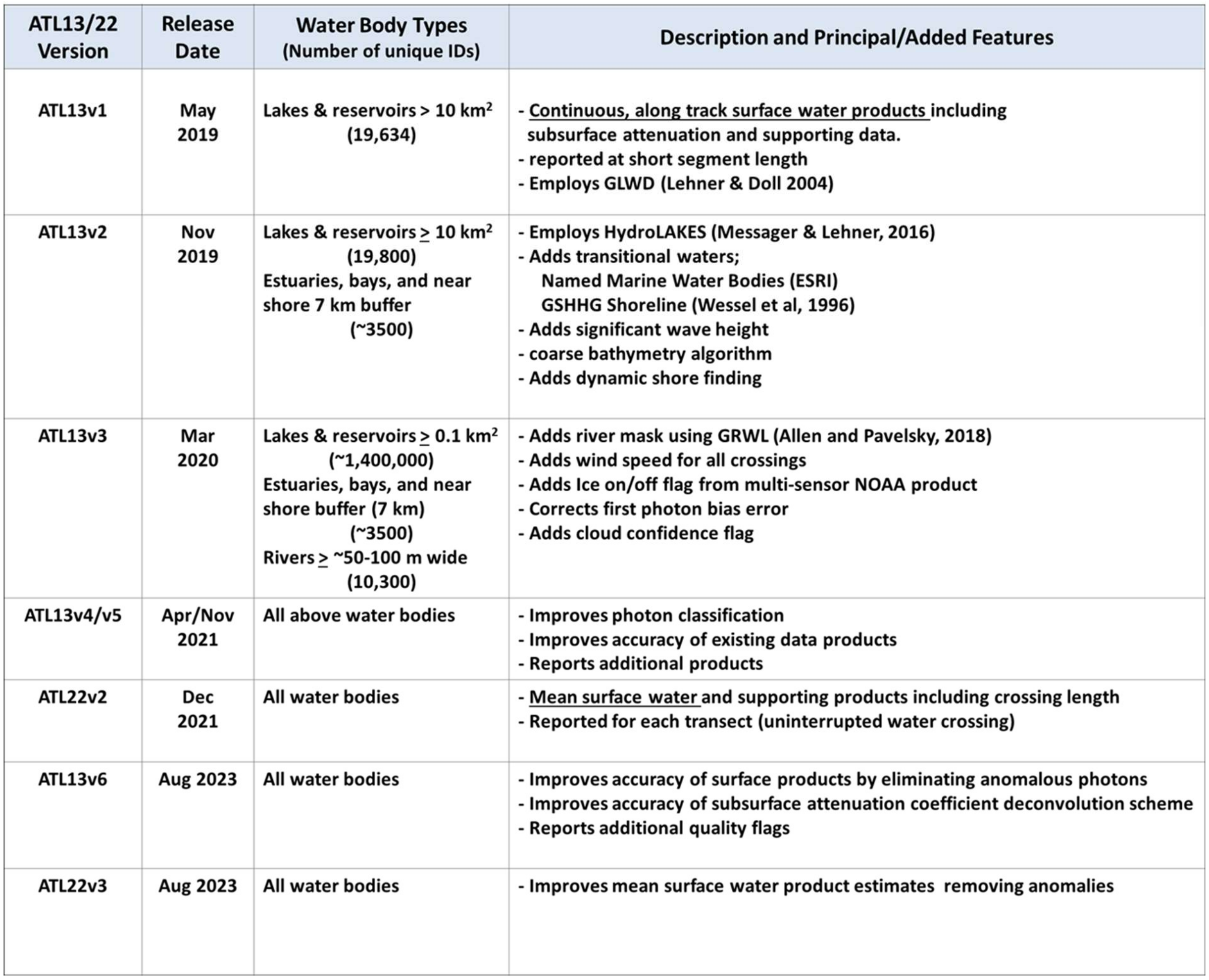

ATL13/22 Version	Release Date	Water Body Types (Number of unique IDs)	Description and Principal/Added Features
ATL13v1	May 2019	Lakes & reservoirs > 10 km^2 (19,634)	- Continuous, along track surface water products including subsurface attenuation and supporting data. - reported at short segment length - Employs GLWD (Lehner & Doll 2004)
ATL13v2	Nov 2019	Lakes & reservoirs ≥ 10 km^2 (19,800) Estuaries, bays, and near shore 7 km buffer (~3500)	- Employs HydroLAKES (Messager & Lehner, 2016) - Adds transitional waters; Named Marine Water Bodies (ESRI) GSHHG Shoreline (Wessel et al, 1996) - Adds significant wave height - coarse bathymetry algorithm - Adds dynamic shore finding
ATL13v3	Mar 2020	Lakes & reservoirs ≥ 0.1 km^2 (~1,400,000) Estuaries, bays, and near shore buffer (7 km) (~3500) Rivers ≥ ~50-100 m wide (10,300)	- Adds river mask using GRWL (Allen and Pavelsky, 2018) - Adds wind speed for all crossings - Adds Ice on/off flag from multi-sensor NOAA product - Corrects first photon bias error - Adds cloud confidence flag
ATL13v4/v5	Apr/Nov 2021	All above water bodies	- Improves photon classification - Improves accuracy of existing data products - Reports additional products
ATL22v2	Dec 2021	All water bodies	- Mean surface water and supporting products including crossing length - Reported for each transect (uninterrupted water crossing)
ATL13v6	Aug 2023	All water bodies	- Improves accuracy of surface products by eliminating anomalous photons - Improves accuracy of subsurface attenuation coefficient deconvolution scheme - Reports additional quality flags
ATL22v3	Aug 2023	All water bodies	- Improves mean surface water product estimates removing anomalies

Table 1-1 Summary of Principal Features of the ATL13 and ATL22 Inland Surface Water Products

1.6 ATL22 Mean Inland Surface Water Data Products Summary

All ATL13 Data Products are reported at the along track, short-segment rate. The new Mean Inland Surface Water Data Product, or ATL22, is currently underway and will include mean transect and associated values as noted in Table 1-1. and Figure 1.1b. The ATL22 ATBD is being published as a separate document.

2.0 BACKGROUND

2.1 Summary of ICESat-2 ATLAS Instrument and Level 2 Data Products

NASA's Ice, Cloud, and land Elevation Satellite-2 (ICESat-2) mission is the second of the ICESat laser altimetry missions launch in September 2018. ICESat-2 carries an improved Advanced Topographic Laser Altimeter System (ATLAS) consisting of a low energy, micropulse, multibeam, high-resolution photon-counting laser altimeter possessing three pairs of beams. Each pair, separated by about 90 m, consists of a high energy (~100 mJ) beam and a low energy (25 mJ) beam each with an approximately 14 m footprint. Pairs of beams are separated by about 3 km. An instrument pulse rate of 10kHz and a nominal ground speed of ~7000m/s allow observations about every 70 cm. A schematic of the shot configuration is shown in Figure 2-1.

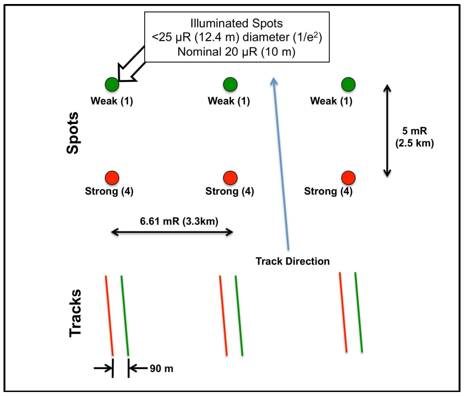

Figure 2-1 ICESat-2 ATLAS six-beam configuration.

ICESat-2/ATLAS is thus significantly different than its predecessor, ICESat/GLAS that fired at a much lower rate (40 Hz) but employed ~80 mJ lasers for full waveform detection (Abshire *et al.* 2005; Schutz *et al.*, 2005). Each returned ATLAS photon is time-tagged with a vertical precision of approximately 30 cm and a geolocation error ranging from 3.6 to 43 cm depending on off-pointing angle (0 to 5 deg respectively, See Luthcke et al., 2019 ATL03g Received Photon Geolocation), and surface and atmospheric characteristics. ATLAS also utilizes a narrower instrument FOV to limit the observation of solar photons. The ATLAS system thus provides higher measurement sensitivity with lower resource requirements. A summary of ATLAS parameters is shown in Table 2-1.

Parameter	**ATLAS**	**MABEL**
Operational altitude	500 km	20 km
Wavelength	532 nm	532 and 1064 nm
Telescope diameter	0.8 m	0.127 m
Laser pulse repetition frequency	10 kHz	Variable 5-25 kHz
Laser pulse energy	Strong beam: 121 μJ Week beam: 30 μJ	Variable, nominal 5-7 μJ per beam
Mean Pulse Width (FWHM)	< 1.5 ns	< 2.0 ns
Laser footprint diameter	17 m	100 μrad (2 m)
Telescope field of view		210 μrad (4.2 m)
Swath width	3.3 km	Variable up to 1.05 km
Inclination	94 deg	N/A

Table 2-1 Summary comparison of the principal ATLAS and MABEL instrument parameters.

An additional unique feature of ICESat-2 is its two orbit modes. Above approximately +/-65 deg latitude, ATLAS operates in a repeat track mode over designated reference tracks similar to ICESat in order to obtain continuous time series of ice sheet change along those tracks. Below +/- 65 deg, however, ICESat-2 will systematically point left or right off the reference tracks in subsequent orbits, in order to conduct a two-year global mapping of vegetation. Additional scheduled off-pointing also is planned to observe targets of opportunity and calibration/validation sites.

2.2 Physics of Open Water

The retrieval of the inland water height requires consideration of several key physical processes including: i) the generation, characterization and statistical representation of surface waves, ii) the propagation and scattering of light, from both ICESat2 and sun sources, especially at the water surface and within the subsurface, and iii) an understanding of the characteristics of the satellite-based transmitted lidar pulse that interacts with the water, a portion that returns to the detector. These are briefly reviewed below and form the basis for the retrieval algorithm.

2.2.1 Dynamics of Inland Water Bodies

Water waves are generated by various mechanisms including wind, storms, seismic events and tides, as shown in Figure 2-2 below (Munk, 1950). Wind generated waves, however, including capillary and gravity waves, are the principal interest to ATL13 as their spatial scales of variability, from centimeters to tens of meters, are commensurate with the lidar observations and the desired Inland Water Body Height data product.

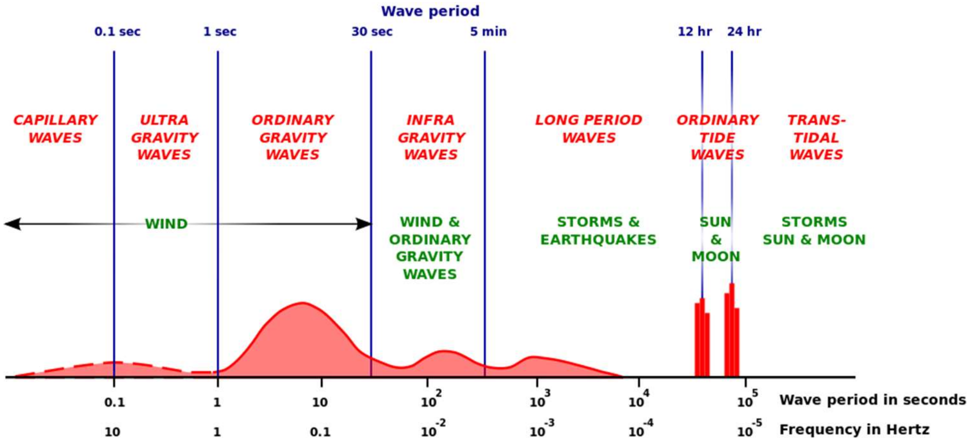

Figure 2-2 Classification of water wave types after Munk (1950).

The smallest water surface perturbations due to wind shear are relatively uniform capillary waves. Possessing short wavelengths of less than 2 cm, they are quickly dampened by the restoring force of surface tension at the cessation of wind. Capillary waves exhibit a rounded crest and a V-shaped trough. Although small, capillary waves play in important role in the retrieval algorithm as they form on flat surface and other gravity waves thus providing numerous facets for specular reflection of both the lidar beam and the sun.

Gravity waves are generated with continued and increasing wind force due to a combination of surface shear and form drag on the face of the wavy surface. Gravity waves exhibit wavelengths from about 10 cm to tens of meters. As their name implies, the restoring force is principally gravity with surface tension playing a small role at the shorter wavelengths. The magnitude of the lake gravity wave is a function of both the properties of the wind including speed, duration, direction, and persistence, and the geometry of the water body including shape, depth and fetch (upwind distance between observation and lee water body shore). As gravity waves approach a sloping shore, bottom friction causes them to slow down and steepen, and eventually break so to dissipate their energy.

A water body surface may exhibit any number of wave types depending on the history of wind events both locally and afar. Waves generated from distance sources that propagate to the region of interest, or that remain after cessation of the wind, are generally smooth in shape and often termed swells.

Waves are described in terms of wavelength (m), period (sec), wavenumber (radians/m) and angular frequency (radians/sec). Wave theories are often based in terms of wavelength and water depth parameter space, as shown in Figure 2-4. By definition, short wave or deep water waves are characterized by a depth to wavelength ratio greater than one-half. Long waves or shallow water waves occur when the depth to wavelength ratio is less than one-half.

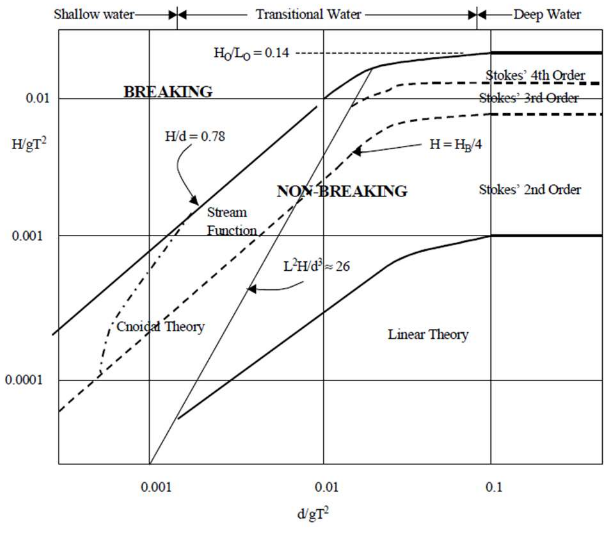

Figure 2-3 Parameter space for wave theories based on normalized height ($H/g\tau^2$) and water depth ($d/g\tau^2$), where g is gravity constant, and τ is wave period, after Le Méhauté, B. (1976).

Two additional properties of open water waves are the significant wave height and significant wave slope. Significant wave height, H_S, is defined the mean wave height (trough to crest) of the highest third of the waves, or equivalently, as four times the standard deviation of the surface height distribution. The significant slope is H_S / λ, where λ is the dominant wavelength. Bourassa et al (1981) described the relation among significant wave height, significant slope, and wind speed, as shown in Fig 2-4. Huang (1981) showed the importance of significant slope relative to mixed layer processes such as mixing efficiency and dissipation for higher frequency surface waves and breaking effects.

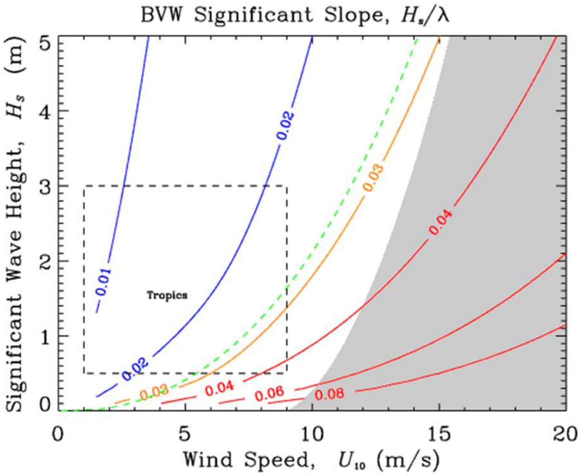

Figure 2-4 Relation among significant wave height, H_S, significant wave slope, H_S/λ, where λ is dominant wavelength, and wind speed U_{10}. Green line shows local-equilibrium values predicted by Bourassa et al. (1996) Blue and red lines represent falling (swells) and rising seas, respectively. (From http://coaps.fsu.edu/papers/use_significant_derived_stress/).

The shape and vertical distribution of open water gravity waves depend on numerous factors including the time history of local wind speed and direction, waves generated from distant sources, changes in water depth, and the reflection of waves from nearby obstacles and shorelines. Open water waves have often been depicted as sinusoidal or trochoidal (Gerstner, 1802; Rod Nave GSU; Bascom, 1964).

Certain simple waves, such as shallow waves approaching a shore, can be modeled explicitly. However, in reality, most wind generated waves are random and require a statistical representation, through the superposition of many waves. Statistically, it has been argued that a random wave field possesses can be modeled with a Gaussian pdf due to the Central Limit Theorem (Longuet-Higgins, 1975; Hu et al, 2008). Caulliez and Gerin (2012) reported on the importance of higher moments as a function of wind speed. Although conducted in a wind tank, they found that the smallest wind speeds yielded the most Gaussian shape.

Waves continue to grow with wind speed, duration and the distance or fetch over which it blows. Wind set-up, or the vertical rise in the water level on the lee side of a water body, as in Figure 2-5, is caused by sustained wind shear on the surface of the water. Set-up ranges from a few centimeters for small lakes to up to two meters for the Great Lakes. After cessation of the wind, lake oscillation or seiching can occur. The relationship between fetch and wind has received significant attention in the literature (Hasselmann et al, 1973; Kahma, 1981, Donelan et al, 1985; Dobson et al, 1989, and Young et al, 1994; and Elfouhaily et al, 1997).

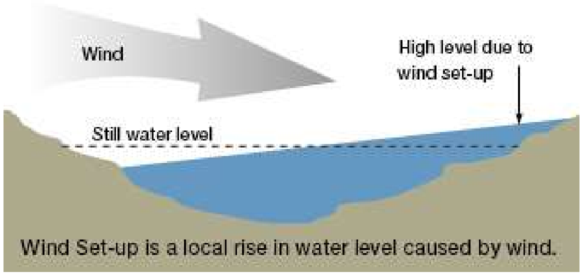

Figure 2-5 Representation of wind set-up due to prevailing winds (graphic from http://www.seagrant.umn.edu/superior/processes).

From the perspective of remote sensing, perhaps more important than surface height, is the slope distribution of the wave facets. Wave facets are critical, especially to optical remote sensing systems such as lidar, since they specularly reflect the majority of signal photons back to the detector. The statistical representation of wave slope has been the subject of much discussion in the literature (E.g. Cox and Munk, 1956; Liu et al., 1997; Ross et al., 2011).
Although published over 50 years ago, one of the most popular and still widely used statistical representations of the water surface slope distribution was proposed by Cox and Munk (1954). Using sun glint analysis, they formulated a near 2D Gaussian distribution or

$$P(Z_{up}, Z_{cr}) = \frac{1}{2\pi\sigma_{up}\sigma_{cr}} \exp\left(-\frac{\xi^2+\eta^2}{2}\right)$$

$$\times \left\{ \begin{aligned} 1 \; & -\tfrac{1}{2}c_{21}(\xi^2-1)\eta \\ & -\tfrac{1}{6}c_{03}(\eta^3-3\eta) \\ & +\tfrac{1}{24}c_{40}(\xi^4-6\xi^2+3) \\ & +\tfrac{1}{24}c_{04}(\eta^4-6\eta^2+3) \\ & +\tfrac{1}{4}c_{22}(\xi^2-1)(\eta^2-1) \end{aligned} \right\} \tag{2.1}$$

where ξ and η are the standardized slope components in the up/downwind and crosswind directions, respectively, σ_{up} and σ_{cr} are the mean standard deviation of the slopes, respectively, and the c_n's are coefficients of five higher moment expansion terms resulting in a two-dimensional Gram Charlier distribution. The expansion terms represent kurtosis and peakedness in the distribution (Cox and Munk, 1953; Liu et al 1996; Breon and Henriot, 2006; many others). Cox and Monk (1954) further demonstrated by empirical regression that σ_{up} and σ_{cr} are linearly related to wind speed height at 12.5 m (41 ft). One dimensional and composite versions also were formulated, or

$$\sigma_c^2 = 0.003 + 0.00192W \tag{2.2a}$$

$$\sigma_u^2 = 0.000 + 0.00316W \tag{2.2b}$$

$$\sigma_c^2 + \sigma_u^2 = 0.003 + 0.00512W \tag{2.2c}$$

where $c_{21} = 0.01 - 0.0086W$ +/- 0.03, $c_{03} = 0.04 - 0.033$ +/- 0.12, $c_{40} = 0.40$ +/- 0.23, $c_{22} = 0.12$ +/- 0.06 and $c_{04} = 0.23$ +/- 0.41. Numerous investigators have proposed modifications or alternatives to the Cox and Munk formulations both theoretically and experimentally (Wu, 1990; Liu et al., 1997, Plant, 2007; Ross, 2007; Elfouhaily et al, 1997; Haltrin 2001; Hu et al., 2008; Breon and Henriot, 2006), although there still appears to be no universally acceptable formulation across the full range of sea states (Su et al, 2002), and some recent satellite studies still assume a Gaussian wave slope distribution (E.g. Hu et al, 2008). Minorov et al (2012) recently asserted that kurtosis increases significantly with wind and that slopes of deep-water waves exhibit much greater kurtosis than shallow water waves. Under a Gaussian assumption, the observations are characterized only by the mean and standard deviation. However, additional cumulants were necessary to reproduce Stokes gravity waves, namely the skewness and kurtosis coefficients in order to take into account vertical asymmetry of waves and flatness of troughs (Minorov et al 2012).

2.2.2 Light Reflection and Transmission in Open Water

There exists extensive literature on light propagation in open water (E.g. Kirk, 1994; Mobley, 1994; and Bukata et al, 1995) including lidar (Churnside, 2014; Montes et al, 2011). The ability of photons to propagate through the water surface and into the water body depends on both the physical reflection properties at the surface governed by Fresnel scattering and wave facet scattering noted above, and the absorption and scattering properties of the water medium governed by various mineral and organic constituents.

The propagation of light within the water column has revealed unique signatures for oceans, coasts and inland estuaries as shown in Figure 2-6 below. As can be seen for 532 nm wavelength which is flown on ICESat-2, the open ocean photic zone representing Case I water can extend to nearly 80 m. However, in the coastal marine and estuary zones, or Case II water, typical light penetration is only up to about 20 m and 6 meters, respectively. Inland water penetration will depend on the clarity of the water body and can vary greatly, but is expected to be from a few meters in turbid water to several tens of meters in clear water.

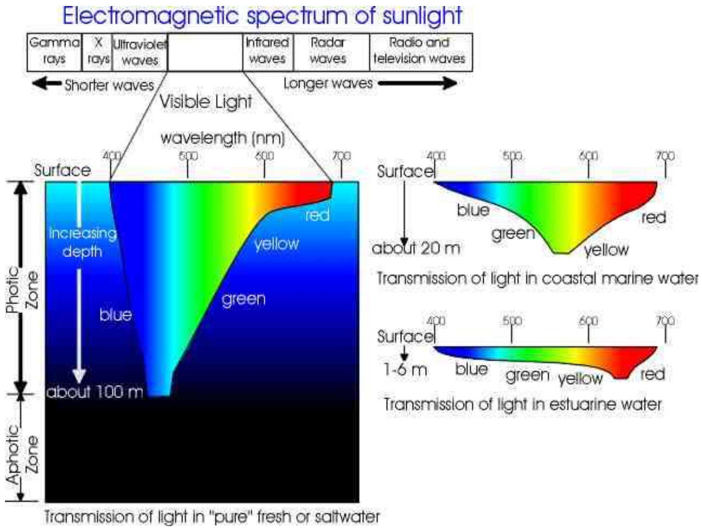

Figure 2-6 Comparative representation of light penetration in natural water including open ocean (left), coastal marine (top right) and estuary (bottom right). (from Buchheim, Oceanography http://www.marinebiology.org/oceanography.htm)

The optical properties of water can be specified in terms of its inherent optical properties (IOP) acting on a vertically stratified water medium. The main properties are wavelength dependent and include: i) the absorption coefficient $\alpha(\lambda)$ (m^{-1}), ii) the scattering coefficient $b(\lambda)$ (m^{-1}), iii) the attenuation coefficient $c(\lambda) = \alpha(\lambda) + b(\lambda)$, and iv) the scattering phase function $\beta(\lambda)$ (sr^{-1}) (Mobley, 1994). The scattering coefficient is often described in terms of forward and backward scattering. The total IOPs of a water body are usually represented as the sum of contributions from water itself and of pertinent optically significant constituents. Such constituents are generally divided into four classes: i) Phytoplankton cells and colonies (Phyt), ii) mineral suspended solids (MSS), iii) colored dissolved organic matter (CDOM), and iv) organic suspended solids or detritus (OSS). The total absorption coefficient is thus,

$$\alpha_{tot} = \alpha_{water} + \alpha_{Phyt} + \alpha_{MSS} + \alpha_{CDOM} + \alpha_{OSS} \qquad (2.3)$$

The scattering and attenuation coefficients and the phase function (β) are also similarly summed.

The above IOPs are widely used in modeling the attenuation of spectral downwelling irradiance with depth, $E_d(\lambda,z)$. In the case of homogeneous water, attenuation is usually represented by the Beer-Lambert Law or

$$E_d(l,z) = E_d(l,0)e^{-c\,z} \tag{2.4}$$

The equation is analogous, although not equal, to the attenuation of subsurface irradiance from diffuse solar light, where the beam attenuation coefficient is referred to as a diffuse attenuation coefficient

$$E_d(l,z) = E_d(l,0)e^{-K_d z} \tag{2.5}$$

and K_d is the sum of specific coefficients for absorption and scattering due to organics and mineral particles as above (See for example Sathyendranath et al 1987; Bricaud et al 1986; Johnsen et al 1994; Babin and Stramski, 2005; Wozniak and Stramski 2004). K_d values generally range from less than 0.1 m^{-1} for clear lakes (Hargreaves, 2003; Morel et al., 2007) to 1.0 for turbid lakes. Coastal New England waters have typical $K_d(532)$ of ~ $0.2m^{-1}$ (Pe'eri et al., 2001, 2004) (Pers. Communication, Christopher Parrish, Oregon State University).

The above equation has important implications for ICESat2 since ATLAS 532 nm beams penetrate into the water column. The retrieval of the surface water height thus needs to account for 532 penetration. However, initial MABEL studies indicate that the mean water surface height correction may be small for inland water, on the order of several centimeters, due to fairly turbid water. Typical attenuation coefficients of several US lakes are shown in Table 2-1.

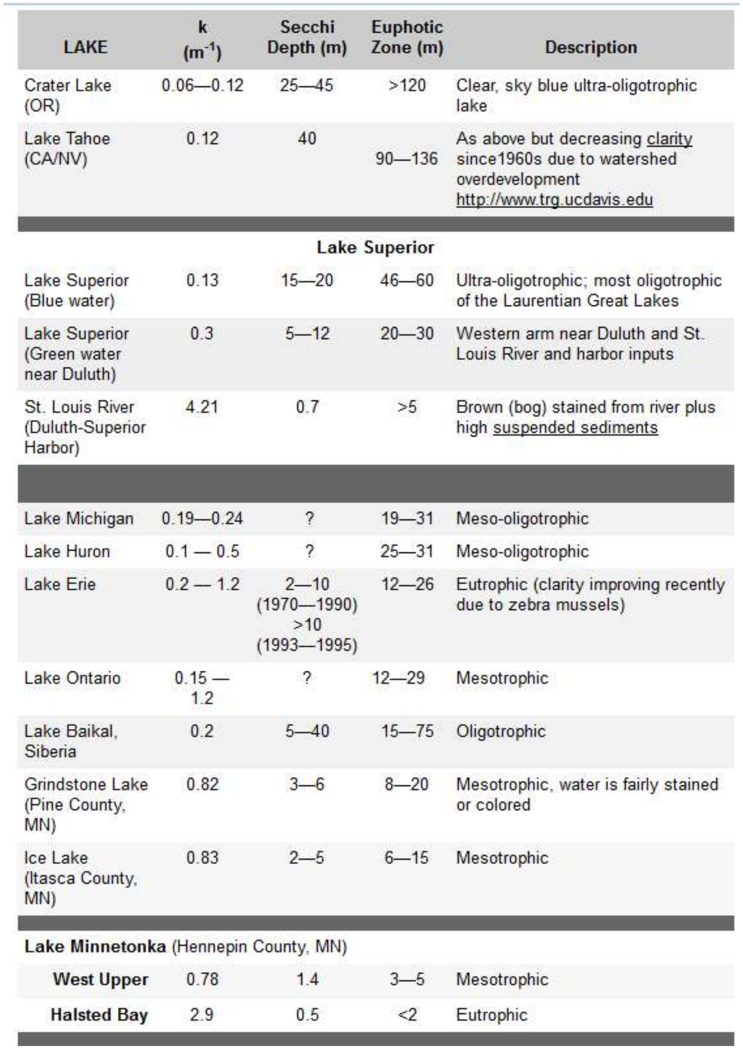

LAKE	k (m^{-1})	Secchi Depth (m)	Euphotic Zone (m)	Description
Crater Lake (OR)	0.06—0.12	25—45	>120	Clear, sky blue ultra-oligotrophic lake
Lake Tahoe (CA/NV)	0.12	40	90—136	As above but decreasing clarity since1960s due to watershed overdevelopment http://www.trg.ucdavis.edu
		Lake Superior		
Lake Superior (Blue water)	0.13	15—20	46—60	Ultra-oligotrophic; most oligotrophic of the Laurentian Great Lakes
Lake Superior (Green water near Duluth)	0.3	5—12	20—30	Western arm near Duluth and St. Louis River and harbor inputs
St. Louis River (Duluth-Superior Harbor)	4.21	0.7	>5	Brown (bog) stained from river plus high suspended sediments
Lake Michigan	0.19—0.24	?	19—31	Meso-oligotrophic
Lake Huron	0.1 — 0.5	?	25—31	Meso-oligotrophic
Lake Erie	0.2 — 1.2	2—10 (1970—1990) >10 (1993—1995)	12—26	Eutrophic (clarity improving recently due to zebra mussels)
Lake Ontario	0.15 — 1.2	?	12—29	Mesotrophic
Lake Baikal, Siberia	0.2	5—40	15—75	Oligotrophic
Grindstone Lake (Pine County, MN)	0.82	3—6	8—20	Mesotrophic, water is fairly stained or colored
Ice Lake (Itasca County, MN)	0.83	2—5	6—15	Mesotrophic
Lake Minnetonka (Hennepin County, MN)				
West Upper	0.78	1.4	3—5	Mesotrophic
Halsted Bay	2.9	0.5	<2	Eutrophic

Table 2-2 Typical values of attenuation coefficient for US lakes from (www.lakeaccess.org)

2.3 Lidar Remote Sensing Over Water

2.3.1 Airborne Lidar

The application of airborne scanning lidar over water including surface and subsurface targets is well documented (E.g. Churnside, 2014, Guenther, 1985). Much of the US interagency work is coordinated through the Joint Airborne Lidar Bathymetry Technical Center of Expertise (JALBTCX) supporting the US Army Corps of Engineers (USACE) and National Oceanic and Atmospheric Administration (NOAA) , the U.S. Naval Observatory (NAVO) and the U.S.

Geological Survey (USGS). Mapping generally includes coincident 532 and 1064 nm lidar in conjunction with hyperspectral imagery. However, several systems that only employ 532 include the NASA/USGS EAARL, the more recent EAARL-B (Wright, 2014), and the Riegl VQ-820-G.

Although both 532 and 1064 nm light only reflects approximately 2% at the water surface due to Fresnel refraction, the 1064 nm wavelength absorbs nearly all the remaining 98% within the first meter, while the 532 nm wavelength both scatters and absorbs at depths to several tens of meters depending on water IOPs. The difference between 1064 and 532 backscatter thus facilitates identification of the water surface height, limited profiling of water depth optical properties associated with mineral and other particulate scattering, and also bottom topography.

The depth dependent lidar signal from airborne sensors has been described in terms of one expression that combines the instrument properties, the scattering properties of the water surface and subsurface attenuation (Churnside, 2014) or

$$S(z) = \frac{EAO(z)T_O T_S^2 \eta n v}{2(nH+z)^2}\beta(\pi,z)\exp[-2\int_0^z \alpha(z')\mathrm{d}z'] + S_B, \tag{2.6}$$

where the instrument properties include, the detector photocathode current *S(z)*, the transmitted pulse energy, *E*, the receiver area, *A*, the overlap function, *O* between the laser beam and the received field of view, the transmission of the receiver optics, T_O, the transmission through the water surface, T_S, the responsivity of the photodetector, η, the distance from the lidar to the surface, *H,* and the photocurrent due to background light, S_B. Water properties include the path length in water *z*, the refractive index of water, *n*, the speed of light in vacuum *v*, the volume scattering coefficient at a scattering angle of π radians β, and the wavelength dependent lidar attenuation coefficient, $\alpha = \alpha(\lambda)$. In homogeneous water, the return signal in Eqn (2.6) effectively reduces to

$$S(z) = C\frac{\exp(-2\alpha z)}{(nH+z)^2} \tag{2.7}$$

Where S(z) is the signal at depth z and C is a parameter that depends on geometry, wavelength and lidar characteristics (Churnside et al, 1998).

A schematic of the scattering and absorption processes resulting from a lidar beam impinging on the water surface is shown in Figure 2.7 (Guenther, 2000). After surface refraction, the approximately 98 % of the lidar beam that impinges the water surface penetrates into the subsurface where it scatters and absorbs, spreading out into a cone of increasing angle. Beam spreading from the original surface footprint occurs over 360 degrees and represents the greatest effect in the dissipation of the lidar beam. Depending on the depth and attenuation of the water column, a relatively small portion of light reaches the bottom, where it exhibits lambertian scattering back up through the water colum, where it is further attenuated, and further scattered at the water air interface. The bottom reflected energy, like the volume scattered energy, will be spread out over a much larger diameter than the incident beam. As a result, only small a fraction of both the volume scattered and bottom reflected energy returns to the receiver. However, in very shallow areas, the 532 nm beam can have nearly no surface return, with the dominant return coming from the bottom, especially in very clear water (Nayegandhi, 2014).

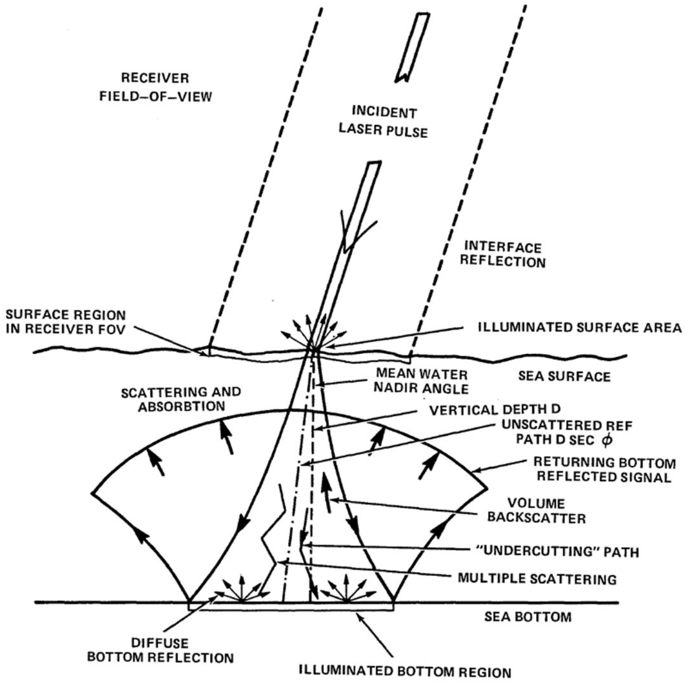

Figure 2-7 Sketch of process lidar subsurface backscattering processes in shallow water

(from Guenther, 2000)

Once the laser beam has penetrated the surface, each photon may be scattered elastically or inelastically, or absorbed (Exton et al., 1983). Elastic scattering is primarily due to Mie scattering from suspended particles (Browell, 1977). Inelastic scattering is a result of either the Raman effect or fluorescence. Both processes result in energy being re-emitted at a different wavelength that was initially transmitted by the lidar. An example for the 532 wavelength is shown in Figure 2-8 below.

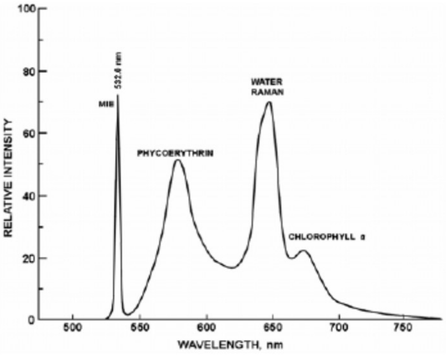

Figure 2-8 Backscattered spectra from natural water sample excited at 532 nm (based on Exton et al., 1983, and Pe'eri et al, 2007).

2.3.2 **Satellite Lidar**

Most satellite ranging studies over oceans have focused on wind speed analysis rather than subsurface bathymetry. Wind speed studies rely on modeling ocean surface backscatter from wave facets (E.g. Lancaster et al,2005; Menzies et al, Hu et al, 2008). Satellite based lidar water profiling over coasts have not been developed due to the high lidar power requirements, and also due to the lack of for 2D satellite scanning observations.

The specular reflectance of lidar and radar from the water surface has been investigated by Barrick (1968), Bufton et al (1983) and (others), including satellite-based studies (Menzies et al, 1998; Lancaster et al, 2005). Lancaster et al (2005) focused on ICESat GLAS reflectance of the ocean surface, although off- nadir pointing was not included. Menzies et al (1997) were the first to examine sea surface directional reflectance and wind speed using the LITE instrument aboard the space shuttle. Hu et al (2008) examined surface wind speed variability using NASA's Cloud-Aerosol Lidar with Orthogonal Polarization (CALIOP) Lidar backscatter data employing the Cox and Munk slope variance – wind speed relations.
The capability of satellite lidar to detect subsurface scattering has been examined by a number of investigators including (Jasinski et al, 2016; Lu et al, 2014; Churnside et al, 2013; Behrenfield et al, 2013; Barton and Jasinski, 2011) using CALIOP profiling and other high altitude lidar.

The feasibility of ICESat-2/ATLAS retrievals of inland water have been established in numerous airborne lidar engineering and science studies and the ICESat/GLAS mission, including lakes. The ICESat/GLAS instrument was a single beam analog sensor with an approximately 70 m footprint and along track spacing of about 180m. Inland water observations were successfully explored with accuracies in the cm to decimeter range, and its height products were used in a number of research and operational programs. The data were utilized in both lake and river studies (e.g. Harding and Jasinski, 2004, Birkett et al., 2010, Calmant et al., 2008, Zhang et al., 2011) that require both height and surface water slope. ICESat heights were also used to validate radar altimetry measurements from ENVISAT and OSTM in the absence of in situ gauge data.

Barton and Jasinski (2011) developed a formulation using CALIOP lidar to retrieve subsurface backscatter as the residual term in the total water backscatter equation. They incorporated the Hu et al (2008) surface specular reflectance that is wind and view angle dependent. The depth-integrated attenuated backscatter (at wavelength λ, in nm) from the water surface viewed by the satellite was represented as a linear sum of surface and subsurface scattering. Results indicated the feasibility of using satellite lidar for observing both surface and subsurface reflectance characteristics in Case II coastal waters.

2.3.3 The Multiple Altimeter Beam Experimental Lidar (MABEL)

The Multiple Altimeter Beam Experimental Lidar (MABEL) was built as a high-altitude prototype of the ATLAS instrument (McGill *et al*. 2013) but possessing additional beams and flexibility to test variations in the ICESat-2 concept. In this capacity, it served several purposes including validation of ICESat models of instrument performance, evaluation of the photon counting system in the 532 nm band, providing experiment data over actual ICESat-2 targets, and development of retrieval algorithms of ICESat-2 data products. From 2012 through 2015, major flight experiments were conducted in Greenland, the east coast United States, the western US, and Alaska. In all these experiments, MABEL was flown aboard either the ER-2 or Proteus Aircraft, at 20 km or above 95% of the Earth's atmosphere. The high-altitude platform more realistically replicates the impact of clouds that ICESat-2 encounters, and that needs to be addressed in the retrieval algorithms. A summary comparison of the relevant ATLAS and MABEL instrument parameters is provided in Table 1-1. The configuration of MABEL beams is shown in Figure 2-9.
Figures 2-10 and 2-11 show typical results from MABEL flights over the Chesapeake Bay and the Atlantic Coast near Virginia Beach, respectively. The figures indicate raw MABEL geolocated photon clouds. Given that the MABEL instrument sampling design scales well with ATLAS, it has proven to be an important instrument for testing the ATL13 algorithm, described in Chapter 6 (Jasinski et al., 2016).

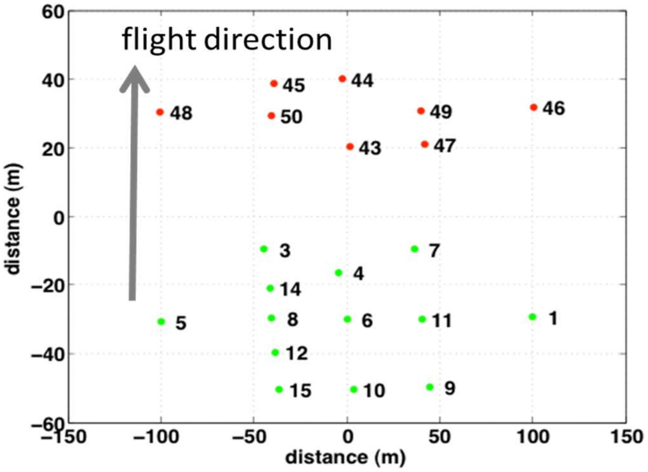

Figure 2-9 Configuration of MABEL beams.

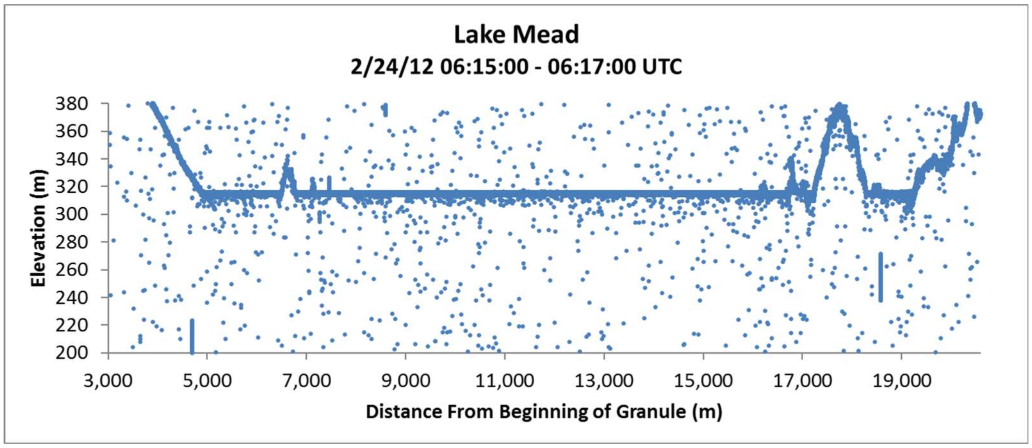

Figure 2-10 Photon cloud data from 2012 MABEL flight over Lake Mead (Jasinski et al., 2016).

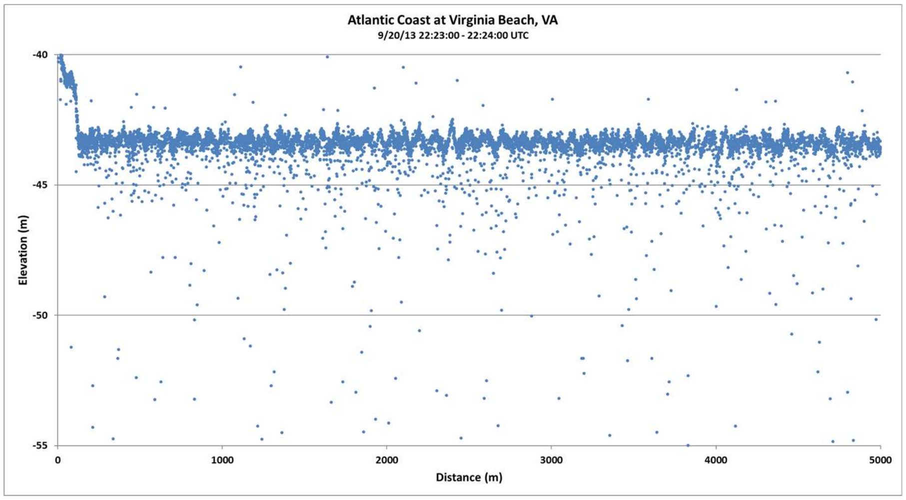

Figure 2-11 Photon cloud data from 2013 MABEL flight over Atlantic Coast near Virginia Beach (Jasinski et al., 2016).

3.0 INLAND WATER PRODUCTS

3.1 Conceptualization of ATLAS observed inland water reflectance

The photon returns reflected back to the satellite are conceptualized by the backscatter model shown in Figure 3.1. The photons received at the ATLAS sensor include backscatter from a number of atmospheric and water targets, including signal photons from ATLAS as well as noise photons from the sun and moon. The relative contribution of the sun will depend on solar zenith and azimuth angles, as compared to the ATLAS zenith and azimuth angles.

The depth-integrated attenuated backscatter γ^{tot} at 532 nm wavelength received by ATLAS from the water can be represented as a sum of backscatter components returning from the water, attenuated by the atmosphere, or mainly:

$$\gamma^{tot} = T_A\left[\gamma^{wA}(1-W) + \gamma^{fA}W + \gamma^{uA} + \gamma^{bA} + \gamma^{wS}(1-W) + \gamma^{fS}W + \gamma^{uS} + \gamma^{bS}\right] \tag{3.1}$$

where,

T_A = atmospheric 532 transmittance along the ATLAS look direction,
γ^{wA} = ATLAS specular backscatter from water surface back to receiver,
γ^{fA} = ATLAS Lambertian backscatter from foam on water surface back to receiver,
γ^{uA} = ATLAS volume backscatter from the water column back to receiver
γ^{bA} = ATLAS Lambertian backscatter light from the bottom
γ^{wS} = Sun specular backscatter from wavy water surface back to receiver,
γ^{fS} = Sun Lambertian backscatter from foam on water surface back to receiver,
γ^{uS} = Sun volume backscatter from the water column back to receiver
γ^{bS} = Sun Lambertian backscatter light from the bottom
W = fraction of foam covered water surface

Other possible components not listed in (3-1) include scattering from surface slicks, and scattering by spray in regions of high winds, solar background, lidar background, and dead count.

Since ATLAS photons are pulsed at 10kHz and subsequently received by the ATLAS detector, their time of travel and hence range can be determined. Solar photons, however, are generated in a continuous stream, so that individual ranges cannot be determined and are thus treated as background.

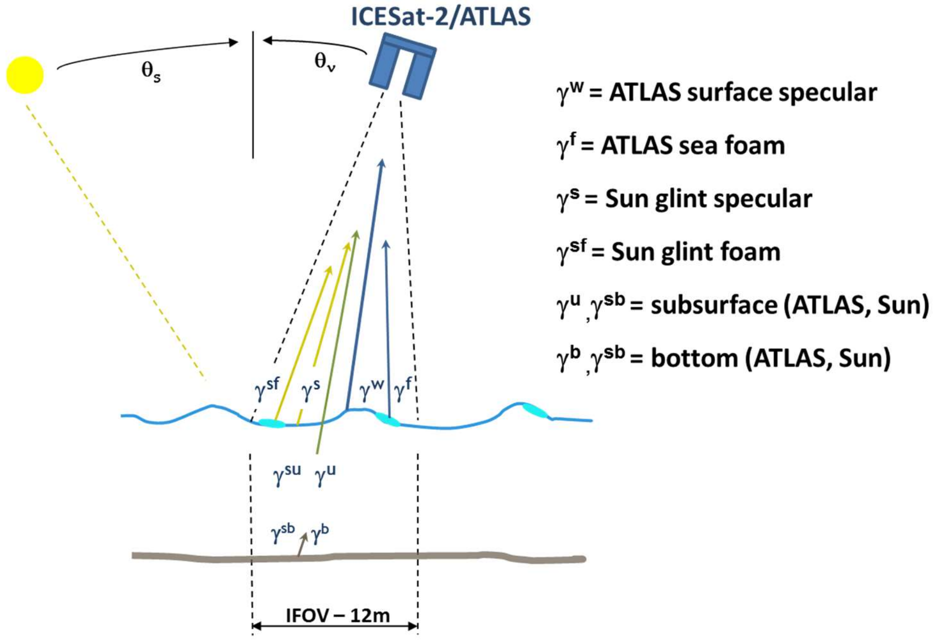

Figure 3-1 Components of the inland water height backscatter model, from Barton and Jasinski, 2011.

The relative magnitude of the backscatter components contributing to the total depth integrated backscatter equation (See Section 4.2) is computed for each L-signal photon segment (E.g. long segment, 1000 signal photon default) for both strong and weak beams. The main purpose is to understand the relative contribution of solar glint, solar foam scattering, and bottom scattering to the overall reflectance equation. The backscatter quantities include, for both ATLAS and Solar sources respectively, the specular backscatter from smooth water surface back to receiver (γ^{wA} , γ^{wS}) and the Lambertian backscatter from foam on water surface back to receiver (γ^{fA} , γ^{fS}). Also computed are the ATLAS volume backscatter from the water column back to receiver (γ^{uA}), and the total ATLAS plus solar Lambertian backscatter light from the bottom (γ^{bA}), and the fraction of foam covered water surface (W). The sum of the solar terms represents the principal contributions to the observed background count.

3.2 Conceptualization of ATLAS observed inland water altimetry

The analysis of the surface signal photons for each beam provides for each segment i) the vertical probability distribution of the height of the wave facets observed by ATLAS, including mean, standard deviation, and along track slope, ii) the distribution of the surface water height including mean, standard deviation, and skewness, iii) the distribution of volume scattering photons and the lidar beam attenuation coefficient, and iv) the identification of potential bottom signal if it exists.

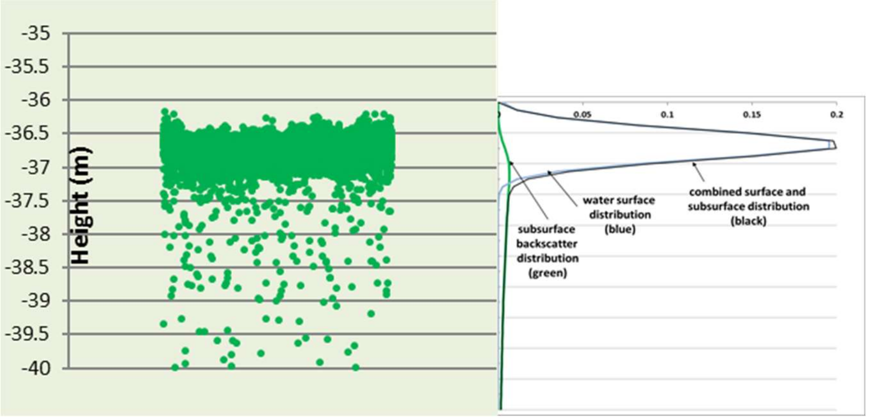

Figure 3-2 Conceptual interpretation of ATLAS vertical photon cloud histogram over inland water consisting of surface water photons and subsurface volume scattering photons.

3.3 Segment height statistics for strong and weak beams

For long signal photon segment (L_seg) lengths, the analysis provides along track mean height, slope, standard deviation, and attenuation coefficient as previously shown in Figure 1-1.

For each reported short segment length (S_seg1) of each strong and weak beam, analysis provides along track mean height, standard deviation, slope and attenuation coefficient, given sufficient data. The attenuation coefficient is the same as that reported by the L_seg covering that short segment.

3.4 The ATL03 Inland Water Mask (Flag)

In order to facilitate processing of data over only land and near coastal regions that possess water bodies, three types of hydrologic masks are created: i) an ATL03 Inland Water Mask, ii) an ATL13 Regional Basin Mask, and iii) an ATL13 Inland Water Body Mask.
The Inland Water team (for ATL13) has worked with AT03 team to construct a gridded water mask of 0.1 km2 that flags whether or not one or more water bodies exist in that grid. Water bodies include lakes, reservoirs, impoundments and permafrost. The purpose of this fixed "Inland Water Mask", shown as the shaded regions in Fig 3-3 below, is one of efficiency. The implementation of ATL13 algorithm draws only on ICESat-2 observations that have been flagged as falling within an AT03 Inland Water Mask. The data base of the ATL03 Inland Water Mask does not identify the type of water body, only that one exists.

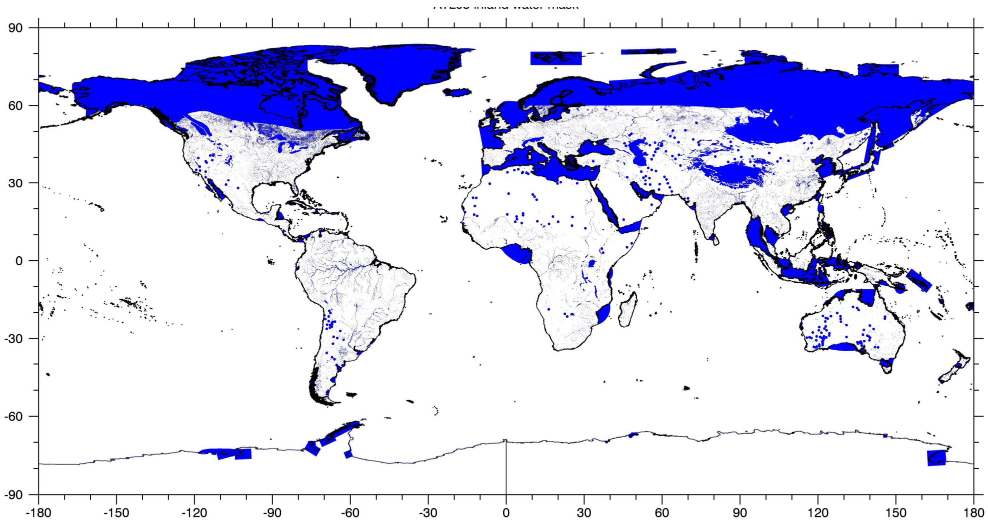

Figure 3-3 ATL03 Inland Water Mask (gridded, non-contiguous).

The ATL03 Inland Water Mask is a high resolution gridded mask developed to extract data for analysis from only those areas required for inland water analysis. The ATL03 mask was created by overlaying the ATL13 inland water body shape file mask, developed by the ATL13 team, onto the global grid. It has been developed from a number of coastline and inland water databases including the Global Self-consistent, Hierarchical, High-resolution Geography (GSHHG) coastlines, various lake database shapefiles including ephemeral lakes, permafrost extent, and a custom set of shapes to close gaps in larger bays where not otherwise included. (ref: ATL03 ATBD)

3.5 ATL13 Regional Basin Mask (Shape File)

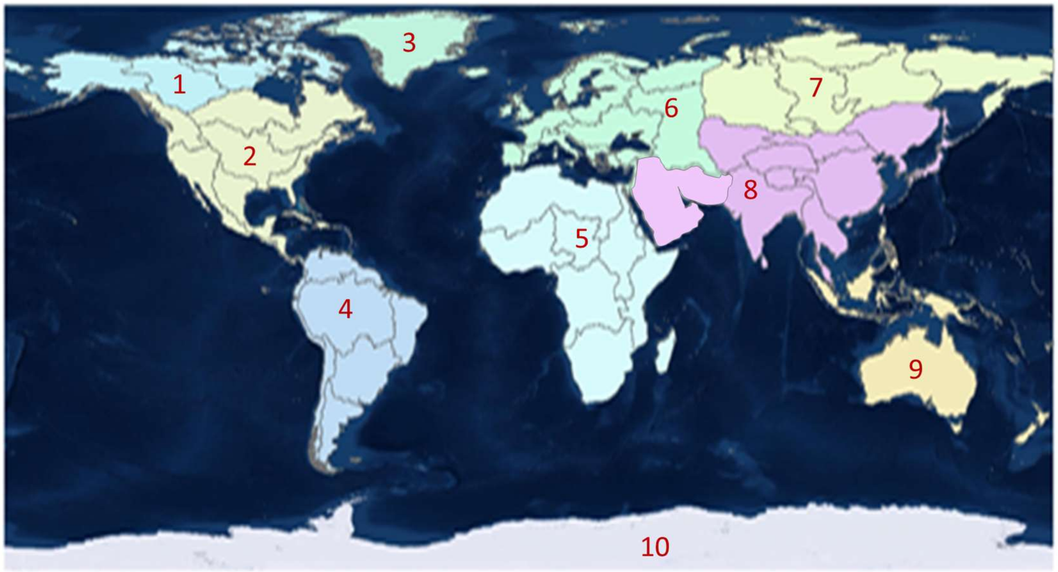

Figure 3-4 ATL13 Regional Basin Mask.

The ATL13 Regional Basin Mask is used to organize the ATLAS data used for inland water calculations and hydrologic data products in a logical manner. It consists of polygons that represent principally the outline of entire large river basins and some adjacent intervening area. Each polygon contains all the lakes and rivers within that river basin. Archiving data products in this manner eliminates the problem of having to store ATLAS inland water data products of contiguous lake and rivers within different files. The regional basins are: 1= Northern North America; 2 = Southern North America; 3- Greenland; 4 = South America; 5 = Africa; 6 = Europe; 7 = Northern Asia; 8 = Southern Asia; 9 = Australia & Oceania; 10 = Antarctica.

3.6 ATL13 Inland Water Body Shape Mask (Shape file)

The ATL13 Inland Water Body Shape Mask facilitates identification of ICESat-2 crossings over individual water bodies. It delineates the shape and spatial distribution of contiguous individual water bodies. These include a composite of lakes, reservoirs, rivers, and transitional waters including estuaries and bays, and near shore coastal waters assembled by the inland water team for use in the ATL13 algorithm. An ATL13 Inland Water Body Shape Mask is employed as a shape-file (E.g. HydroLAKES, Lehner and Messager, 2016; Global River Width from Landsat (GRWL) (Allen and Pavelsky, 2018); Named Marine Water Bodies, ESRI), unlike the ATL03 flag above which is a gridded product. The ATL13 Mask consists of polygons, each representing either an entire single lake or reservoir, 7-km wide coast segment, bay, or river segment including its tributaries. The ATL13 Inland Water Body Shape Mask includes an approximately 100m buffer extended over the land so that the land/water interface is identified. An example of what the Water Body Mask looks like is shown in Figure 3-7 below for North America. Each lake is identified by number, lat/long, and local name if available.

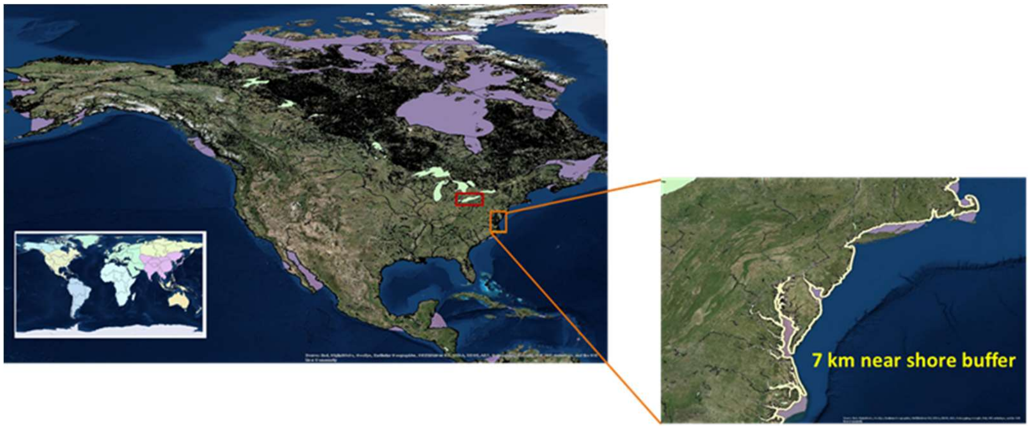

Figure 3-5 Example of ATL13 Inland Water Body Shape Mask for North America Shape file (Jasinski, Stoll et al, AGU 2019)

It is estimated that the multi-beam ATL13 ICESat-2 coverage contains potentially over 1.4 million water bodies, allowing the overpass of about 650 lakes ≥ 100km2, of which 50% are in Canada, and 25% in Eurasia. For lakes ≥ 10km2, the estimate is about 19,300 lakes.With 100 photon along-track aggregation there is the potential to record heights of the more numerous smaller impoundments (> 1-5 km2) which number in tens of thousands. Height accuracy will depend on aggregation level and water state but is expected to be about 10cm for the strong beam.

4.0 ALGORITHM THEORY

4.1 Overall Approach

ATLAS observations provide information on both the altimetry and the backscatter of the water surface and subsurface. Of principal interest for ATL13 is the altimetry that will provide information on along track height statistics. However, knowledge of backscatter also will contribute to understanding the water apparent reflectance, slope distribution, wind speed and subsurface backscatter attenuation.

The overall goal is to estimate short (~75-100 signal photons) segments of mean height for each ATLAS beam that crosses a water body in the along track direction. In general, although the far majority of the returned photons are specular photons returned from the water surface, up to several percent are returned as part of the subsurface volume backscatter. Thus, prior to estimating the short segments height statistics, it is necessary to first analyze and estimate the volume scattering parameters which require long segments of 1 to 3 km that provide the sufficient number of subsurface photons.

The retrieval of the inland water height algorithm for ATL13 thus involves a combination of physical and statistical modeling of key physical processes related to open water surface dynamics and light propagation, as outlined in Chapters 2 and 3. Analysis primarily uses data from ATLAS ATL03 products, and also from external sources including meteorological data. The key steps include i) identifying the intersection of a contiguous water body and beginning and ending water edges of individual ICESat2 beam, ii) modeling the reflectance components that contribute to the integrated signal exiting the water surface toward the receiver, iii) analyzing models of the surface water height statistical distributions, subsurface volume scattering, and their relation to the distribution of the signal photons that emanate from water surface facets and back to the receiver, iv) extraction of the true representation of water reflectance and height by removing background photons, v) deconvolving of the ATLAS observations with its instrument response function, and vi) reporting the statistics of along track data products including principally the surface water height, but also the subsurface attenuation, significant wave height, and mean maximum water surface slope and azimuth from two adjacent strong beams. An evaluation of the accuracy and quality of the measurement is made.
The overall approach is to choose algorithm components that i) are commensurate with the range of scales of the inland water body product, and ii) that allow for a robust operational computation of surface height over the vast range, types and conditions of inland water bodies that ICESat-2 encounters during its lifetime.

The essential theoretical basis to implement the above strategy is briefly reviewed below.

4.2 Satellite Inland Water Backscatter Model

4.2.1 Water surface specular model

Water surface specular reflection is the largest component to the backscatter. Since specular returns reflect back toward the lidar receiver only if the wave facet surface slope equals the off-pointing angle, reflection models are based on the distribution of wave facets. Both Gaussian and near Gaussian distributions have been employed. Specular reflection decreases with increasing wave size and is therefore greatest in calm waters.

ATL13 employs either i) the Gaussian or the Gram-Charlier (Cox and Munk, 1954) wave facet slope model for the water surface distribution, and ii) the Cox and Monk type wind variance model shown in Eqn 2-2. Various combinations of these models have been used by previous investigators (E.g. Hu *et al.* 2008, Platt, 1973; Menzies *et al, 1998*, Tratt *et al, 2002*, Lancaster et al, 2005) that depend, in some cases, on the source of the input data. For instance, in analysis of wind speed fields using CALIOP observations using AMSR-E wind fields, Hu et al (2008) assumed a Gaussian surface height distribution for specular reflectance or

$$\gamma_\lambda^w = \frac{\rho_\lambda}{4\,\pi\,\sigma_s^2\,cos^4\theta}\,exp\left[\frac{-tan^2\theta}{2\sigma_s^2}\right] \tag{4.1}$$

where ρ_λ is the Fresnel specular reflection coefficient ($\rho_{532} \approx 0.0209$), σ_s^2 is the wave slope variance (or mean square slope, MSS), and θ is the zenith angle of the sensor. The Hu *et al* (2008) composite model for the wave slope variance, modified at the upper and lower ends of the wind speed spectrum from that of Cox and Munk, is

$$\sigma_s^2 = \begin{cases} U < 7m/s & 0.0146\sqrt{U} \\ 7 \le U < 13.3\ m/s & 0.003 + 0.00512\ U \\ U \ge 13.3\ m/s & 0.138\log_{10} U - 0.084 \end{cases} \tag{4.2}$$

where U is wind speed.

4.2.2 Water surface foam model

The scattering of the lidar from whitecaps and foam streaks on the water surface can be significant, although this component is mainly a factor at wind speeds higher than about 10 m/s. At this speed, the magnitude of foam scattering approaches the volume scattering of low turbidity natural waters. Moore *et al.* (2000) modeled the reflectance of foam as a function of wind speed. In this model the reflectance of the foam is expressed as an “additional” contribution to reflectance, representing the increased reflectance of the ocean surface due to the foam. At 532 nm, the foam backscatter is modeled as a Lambertian process or,

$$\gamma^{fA} = W\gamma^{wA} + 3.14 \times 10^{-6} U^{2.55} \frac{\cos\theta}{\pi} \tag{4.3}$$

from foam covering a fractional area, *W*, described by Callaghan and White (2009) or

$$W = \begin{cases} U < 3.70 & 0 \\ 3.70 \leq U < 10.1874 & 3.18 \times 10^{-5}(U - 3.70)^3 \\ U \geq 10.1874 & 4.82 \times 10^{-6}(U + 1.98)^3 \end{cases} \tag{4.4}$$

4.2.3 Volume scattering model

Models of subsurface scattering applied to airborne lidar have been developed (e.g. Gordon, 1982; and Phillips and Koerber, 1984) in terms of the water optical properties including volume backscatter and attenuation coefficients. These may be applicable to ATLAS, however, they need to be tested on MABEL data. Because many of the atmospheric and instrument parameters are not precisely known, the subsurface backscatter is modeled similar to Equation (2.5)

$$\gamma^{uA}(d) = \rho_s(d) = \beta * \alpha * c_l * \exp(-\alpha * d) \tag{4.5}$$

where α is the attenuation coefficient, β is coefficient that includes both instrument and backscatter magnitude, c_l is a correction for light speed (assumed =1/1.3) and d is depth.

4.2.4 Bottom reflectance

Bottom reflectance is treated as a Lambertian surface.

4.2.5 Relative magnitude of anticipated returns

The relative magnitudes of typical ATLAS backscatter terms for the strong beam is shown in Figure 4-1 below following the approach by Barton and Jasinski (2011). Results are presented as a function of wind speed. The typical scenario shown in Figure 4-2 represents an ATLAS strong beam and 0.3 deg off Nadir view, and a solar zenith angle of 30 deg. Results exhibit a strong dependency on wind speed. For instance, for wind speeds greater than about 7 m/s, the contribution from sunglint and sun foam are over an order of magnitude smaller than their

ATLAS counterpart. However, the sunglint contribution is about the same magnitude as ATLAS foam scattering for wind speeds greater than about 10 m/s.

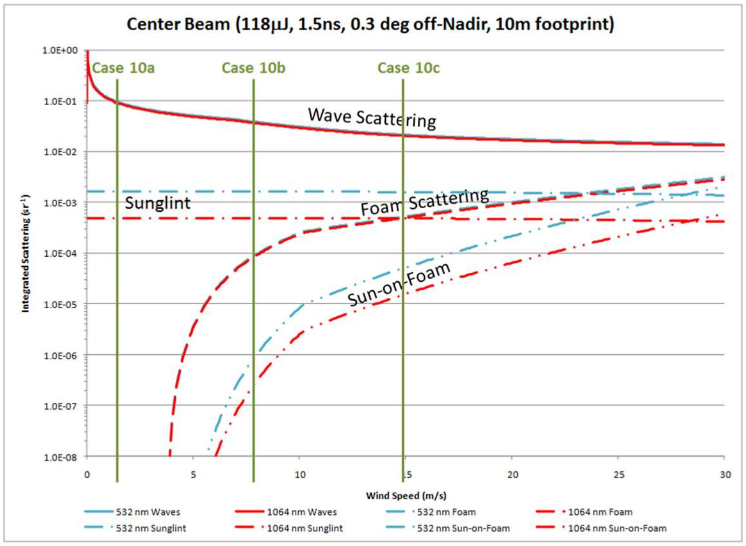

Figure 4-1 Relative contribution of water backscatter terms (Barton and Jasinski, 2011).

4.2.6 Atmosphere and Meteorology input

The specular water surface and foam backscatter models requires wind speed and atmospheric transmittance, *T*, including Raleigh, cloud, and aerosol effects. When *T* or cloud cover are known, wind speed can theoretically be estimated using Hu et al.'s equation in 4.1. Otherwise, wind speed is obtained externally from ATL03 through modeled sources, such as the European Centre for Medium-Range Weather Forecast (ECMWF) model. Cloud cover may be available from GOES imagery depending on location.

4.3 Water surface height model

4.3.1 Photons contributing to the water surface height

The signal photons contributing to the water surface height distribution are those associated with the ATLAS related scattering terms in Equation 4.1. The signal photons not associated with the surface height need to be identified and, in some cases, removed. These generally appear as somewhat uniformly distributed background photons in the vertical profile, both above and below surface. Their source primarily consists of the solar background, although some ATLAS dark count background also may exist. Background is obtained from the ATL03 data product.

Removing background effects in ATL13 is implemented by subtracting off the uniform amount from the surface height histogram, leaving only the terms $\gamma^{wA}(1-W)+\gamma^{fA}W+\gamma^{uA}$.

For a given water body crossing, analyses are executed for each transect, where a transect is a portion of the ICESat-2 crossing uninterrupted by land such as islands, peninsulas or meanders. Transects are defined by the mask and are buffered based on water body type. The transect is tested to identify if anomalous short segment(s) exist at either the beginning and/or the end of the transect.

4.3.2 **Estimation of Background and Signal to Background Noise Ratio**

An expression of the vertical profile of ATLAS's 's observable subsurface backscattered signal photons is required to separate the surface water and subsurface photons, and to understand the depth of penetration. This is estimated based either on i) classified ATL03 photons or ii) formulated as the ratio of the depth dependent signal photon density to mean background density, SBR(d), written (after Schroeder 1999; Jasinski et al., 2016).

4.3.2.1 Estimation of background count based on classified photons

ATL13 utilizes the signal classification designations from ATL03 to compute background. The ATL03 computes background counts obtained over a 50-shot time interval (200 Hz), reduced by the signal photons and potential TEP photons, over a variable altimetric range window height that is reduced by the signal photon span height. The ATL13 background density (counts/m) is computed as:

Bckgrd_Dnsty_50sht = ***bckgrd_counts_reduced/bckgrd_int_height_reduced***. (4.6a)

The background density per 50 shots over each ATL13 5cm histogram bin is thus

Bckgrd_Dnsty_50sht_5cm = Bckgrd_Dnsty * 0.05. (counts). (4.6b)

Bckgrd_Dnsty_50sht_5cm is the same for each bin but can change along track.
The background density over an ATL13 short segment must account for the length of the segment and thus the sum of each 50-shot reporting within that segment.
Bckgrd_Dnsty_50sht_5cm_Sseg = $\Sigma_{i=1,\ N\_50sht\_Sseg}$ Bckgrd_Dnsty_50sht_5cm$_i$. (counts) (4.6c)

Where "i" is the index of 50-shot (200 Hz) reportings in the short segment, or
N_50sht_Sseg = Length_short seg/(G_spd/200) (unitless) (4.6d)

where G_spd is obtained from ATL03 (nominally 7000 m/s). If Bckgrd_Dnsty_50sht_5cm$_i$ only partially overlaps the leading or trailing ends of the short segment, only include the respective fractional overlap of those background photons. Report the background density for each short segment in terms of flags based on threshold values.

4.3.2.2 Estimation of ATL13 signal to noise ratio

The signal to noise ratio is expressed

$$SBR(d) = \frac{\rho_L(d)}{\rho_{SB} + \rho_{LB} + \rho_{DC}} \tag{4.7a}$$

where $\rho_L(d)$ equals the observed lidar signal photon density (m^{-2}) as a function of depth, d, and the denominator represents the sum of the mean of all background noise densities (m^{-2}) including solar background, ρ_{SB}, lidar background, ρ_{LB}, and dead count, ρ_{DC}. Mean background density, constant throughout the vertical column, was computed as the mean number of non-signal photon counts in the atmosphere above the water surface, per meter depth per meter transect (m^{-2}). During daytime, the background consists mostly of solar backscatter. At night, the background density drops significantly and is primarily due to lidar backscatter.
Because both the total observed return and the mean background can be computed directly from the observed vertical profile, and because the background can range over several orders of magnitude, Equation 4.6 is more conveniently rewritten as

$$LSBR(d) = Log_{10}\left[\frac{\rho_L(d) + \rho_{SB} + \rho_{LB} + \rho_{DC}}{\rho_{SB} + \rho_{LB} + \rho_{DC}} - 1\right] \tag{4.7b}$$

where the numerator in the brackets represents the total return observed by MABEL including both signal and background photons. Prior to computing *LSBR(d),* a vertical histogram of the total return is created at 0.05 m bin increments using all water photons observed along flight path. The mean background in the denominator is estimated from observed atmospheric photons. *LSBR(d)* is computed and smoothed employing a 0.5 to 1.0 m moving average as necessary depending on the specific site.
A threshold value where LSBR(d) = -1 or $LSBR_{-1}$ represents where the SBR =0.1 (Alternately, $LSBR_0$ represents where the SBR =1).
Although computed successfully using MABEL observations (Jasinski et al., 2016) the robustness of the LSBR is currently under evaluation. A default value of 5 -10 m can be used as $LSBR_{-1}$ over open water of most lakes.

4.3.3 **Estimation of water surface height and slope variance**

A Gaussian distribution of water surface height is assumed, defended scientifically (E.g. Mobley, 1994) and based on the Central Limit Argument. Use of the Gaussian may also be the most practical assumption given the operational nature of the ATL13 data product, and it having to compute, globally, a wide range of lake types, sizes and wind speed conditions. Further, there is some justification for the Gaussian water based on MABEL analysis and smaller heights compared to open ocean. Thus, the Gaussian distribution may be more suitable for small water bodies (< 5-50 km), where it can be assumed fetch and wave height is small.

Recent analysis of MABEL flights over inland water targets appear to support the Gaussian assumption. Examples of this approach applied to MABEL data showed very good accuracy, as shown in Section 2.4.3. For large water bodies, where wave heights can be large especially for winds > 7m/s, a greater number of signal photons from larger segment lengths allows better characterization of the surface height distribution including its higher moments. Analysis thus employs empirical relations among wave slope variance, water height variance, significant wave height, significant slope and wind speed.

4.3.4 **Estimation of water surface slope variance**

A key step in retrieving wave reflectance properties is knowledge of the mean square slope of the wave facets. The mean square slope (MSS) can be estimated from the elevation spectrum, or the Fourier transform of the autocovariance function of the surface height. The MSS in the omnidirectional context is expressed (E.g. Elfouhaily et al, 1998)

$$MSS = \int_0^\infty k^2\, S(k) dk$$

where k is wavenumber and $k^2S(k)$ is the omnidirectional slope spectrum.
A simpler approach is employed in ATL13, is estimating MSS based on histogramming the photon cloud. Literature review indicates there are only few studies directly relating the distribution of water height to water slope including non-Gaussian (Longuet-Higgins, 1963; Tayfun, 1980; Huang et al, 1984). There is unfortunately little available literature on the correlation between wave slope and wave height distribution.
However, an estimate of the water surface variance can be made using recently published results by Kay et al (2011). Drawing on results from other investigators (Apel, 1994; Cox and Munk, 1954; Elfouhaily et al, 1997; Zaneveld, 2011), they pointed out that the mean square slope is proportional to wind speed, while the height standard deviation is proportional to the square of wind speed. Their graphical results are shown below in Figure 4-2. They also indicate very good agreement with the Cox and Munk (1954) wave slope - wind speed relation.

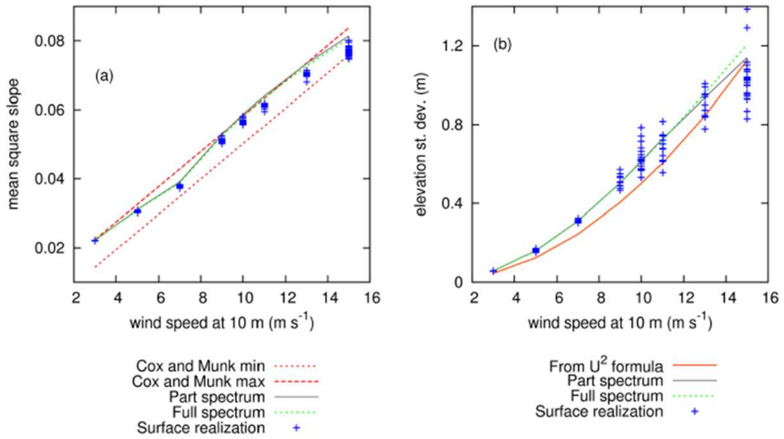

Figure 4-2. Wind speed dependence of mean square slope (left) and height standard deviation (right) (After Kay et al, 2011).

By combining the above two figures, a relationship is developed between the mean square slope (MSS) and the water height standard deviation when wind is present. For this, use the σ_h height wind speed relation (Fig 4-2 left., summarized by Kay et al, 2009) or

$$\sigma_h = 0.005 * U^2 \tag{4.8}$$

in conjunction with the MSS-wind speed relations by Hu et al (2008) in Equation 4.2 (or the Cox and Munk (1954) relations in equation 2.2) which lead to Figure 4-3 below.

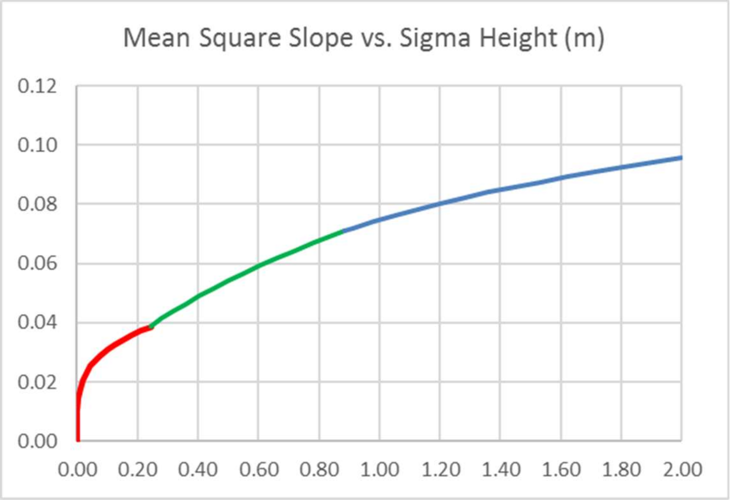

Figure 4-3 Relationship between MSS (or σ_s^2) and σ_h derived by combining Eqn. 4.8 from Kay et al (2011) with Eqn. 4.2 from Hu et al (2008), as shown in Eqn. 4.15. Colors represent different wind speed ranges.

Results show good consistency with analysis by Hwang et al, 2009, shown in Figure 4-4 below.

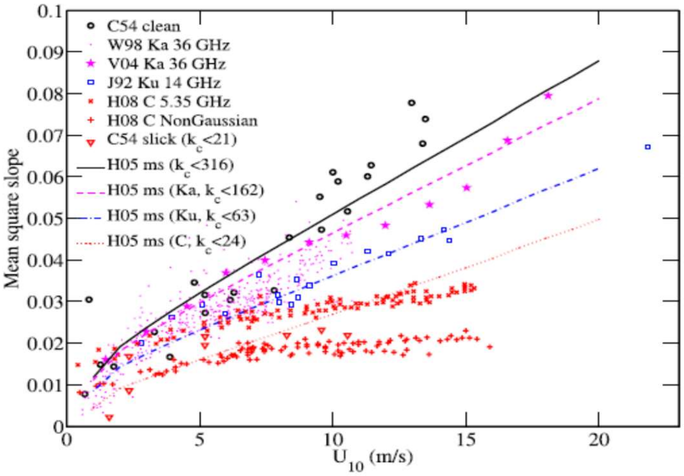

Figure 4-4 Filtered MSS as a function of wind speed based on measurements of airborne radars with different frequencies. [Jackson et al., 1992; Walsh et al., 1998; Vandemark et al., 2004; Hauser et al., 2008] and sun glitter analysis [Cox and Munk, 1954]. The smooth curves are the corresponding mss obtained from integration of the wave number spectral model (mixed sea condition) of Hwang [2005] with the upper cutoff wave number defined by Jackson et al. [1992]. J92, Jackson et al. [1992]; W98, Walsh et al. [1998]; V04, Vandemark et al. [2004]; H08, Hauser et al. [2008]; C05, Cox and Munk [1954]; H05, Hwang [2005]. (From Hwang, 2009).

When wind is not present, residual waves exist as swells. In this case, the relation between wave height and wave slope variance are determined from the observations.

4.4 Instrument response function (transmitted pulse shape)

All the photons within a given pulse are assigned the same time of departure. Since the instrument response function may extend over one or two thousand mm (See MABEL response function in Figure 4-5 below), the observed ATLAS signal photons' return time from the surface facet and foam height distribution represent an integration of all the photons from that pulse that may have slightly different start times depending on their position within the pulse. Consequently, a technique to deconvolve the distribution of the ensemble of surface signal photons from the instrument response distribution needs to be implemented.

A critical step in the surface water height retrieval algorithm is the deconvolution of the instrument transmitted response function (or histogram) from the observed histogram, in order to extract the actual water response histogram. Experience with MABEL indicates that the lidar pulse can be spread out over 2500 mm. See Figure 4-5 below obtained from the ICESat-2 Project Office. This long response function affects the observations by broadening the distribution of the returns, thereby distorting the true pdf of the combined surface height, volume scattering, and bottom reflected signal photons.

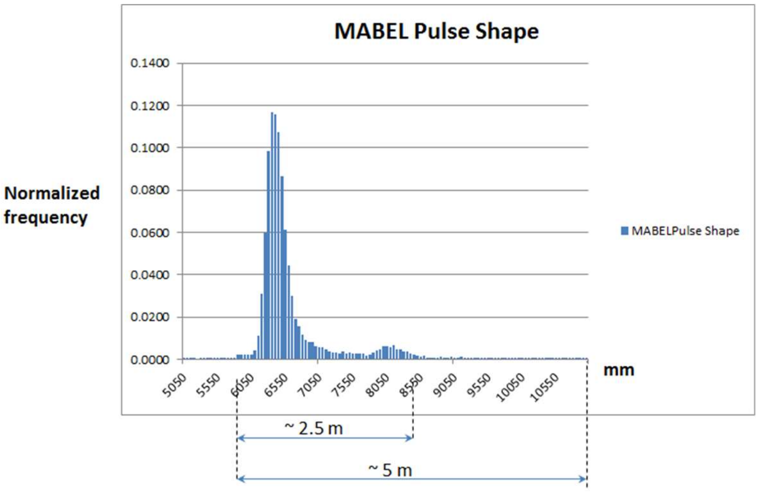

Figure 4-5 MABEL response function (from B. Cook NASA, 2012)

Figure 4-5 exhibits the typical histogram of the MABEL instrument in 5 mm bins ranging from 6000 to 8550 mm. The overall shape indicates a half-width, half max width of about 500 mm with after pulse peak about 2 m to the right. Although small, this tail must be considered in the full deconvolution order to improve retrieval accuracy and to fully understand the volume scattering effect which can be of the same magnitude as the tail.

4.5 Deconvolution of instrument response from lidar returns

4.5.1 Constrained Deconvolution Method

The Impulse Response Functions (IRF) of prototype photon counting sensors such as MABEL and SIMPL have shown to exhibit much variability, especially with regard to the existence of an afterpulse with varying magnitude. Further since all photons pulsed are assigned the same time of departure, the true vertical distribution of observed photons can only be determined through a deconvolution of the observed IRF functions. The impact of the instrument response function thus needs to be removed in order to determine the true surface and subsurface distribution. The height of the ATLAS signal photons represents the convolution of the instrument transmit pulse, and the water surface response. Thus, the true water surface response can only be obtained by deconvolving the instrument and surface response, given knowledge of the integrated observations.

This can be achieved using various parametric and non-parametric methods. However, experience based on MABEL analysis over several inland water bodies using non-parametric approaches, including spectral analysis and matrix inversion, indicates these approaches may not be robust for smaller inland water bodies. This is thought to be a result of the relatively small number of signal photons (several hundred) available to effectively compute at least a somewhat smooth histogram required for inversion.
Based on the above experience, a parametric, “Constrained Deconvolution” approach has been developed for ICESat-2 ATLAS measurements over inland water. The constrained deconvolution approach requires an assumption of an *a priori* functional form of the individual components of inland water backscatter. **It therefore solves the deconvolution problem while at the same time estimating the parameters of the model.**

A standard deconvolution integral is assumed for a linear system with finite time steps. Assigning the probability density function (pdf) of the instrument response function as x(t), and the actual or true unit vertical distribution of the water signal photons per unit pulse as h(t), then the integrated pdf of all signal photons returned to the receiver from the entire instrument response function, y(t), can be written as the convolution of x(t) and h(t). In continuous form,

$$y(t) = \int_0^t h(\tau)x(t-\tau)d\tau \tag{4.9}$$

In discrete form, (4.9) can be expressed

$$y_j = \Sigma\, h_{i-j}\, x_i \tag{4.10}$$

i = the number of instrument pulse bins and j is the number of output height bins. The y_j represents the histogram of the observed water photons for a given segment length, x_i is the lidar pulse histogram (IRF) measured over i bins. Finally, h_{i-j} represents the actual or true unit water surface response of the water, before bias correction.

4.5.2 Solution Approach

The solution to (4.10) is obtained by first assuming a functional form for the actual or unit water column h(t) with unknown parameters. The h(t) and x(t) are then convolved over a range of model parameters until a best fit of the model with the histogram of the observed signal photons is achieved. Thus, the model parameters of the water column including the true water surface height distribution, and the subsurface distribution, are resolved together within the deconvolution scheme.

A key element in the implementation is that each bin (5 cm width) of the IRF is convolved with the model. This is shown in Figure 4-6 for the particular MABEL response function during a 2012 flight over the Chesapeake Bay.

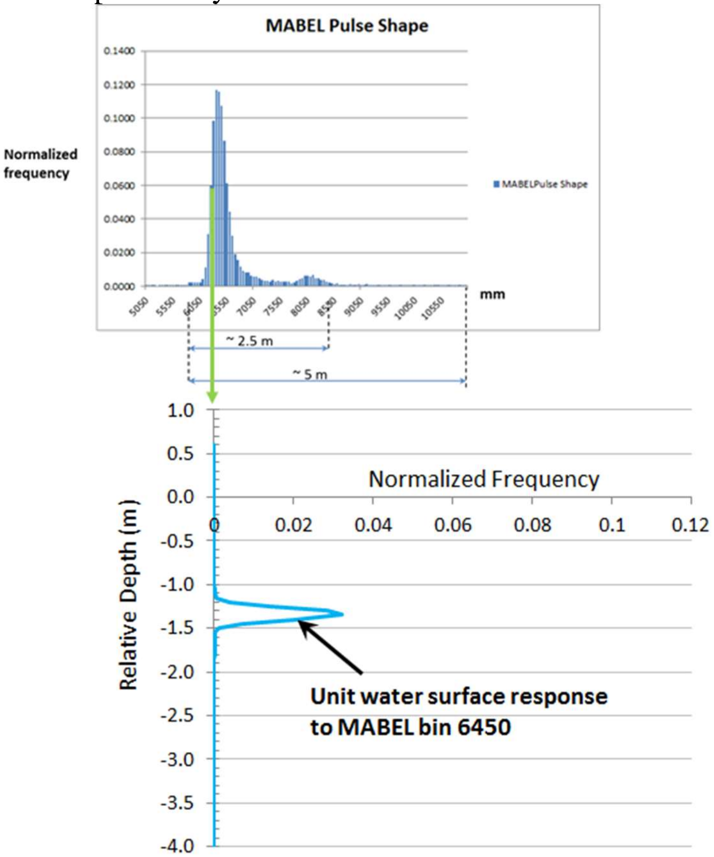

Figure 4-6 Constrained Deconvolution Method- Unit water surface response for one 5cm MABEL bin, arbitrarily selected as 6450 mm.

In the example, a Gaussian water surface height distribution is assumed with an exponential subsurface decay. Figure 4-6 shows MABEL bin 6450, with a normalized frequency of 0.0600, convolved with the model and an initial set of assumed parameters, resulting in a unit water response associated with that bin. Figure 4-7 shows the full convolution of all MABEL bins which are then summed and compared to the original MABEL observation. The optimal solution occurs when the convolved model best fits the observed data. The best fit analysis that partitions the subsurface and surface deconvolution and based on estimation of the standard error allows a better fit of the tails.

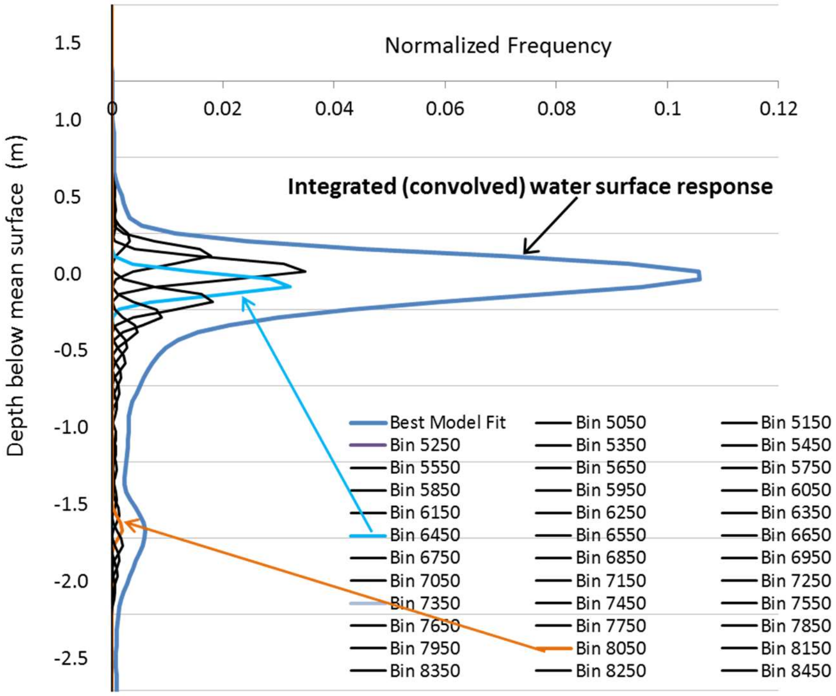

Figure 4-7 Constrained Deconvolution Method – Integrated response to all MABEL bins.

4.5.3 **Deconvolution of subsurface backscatter profile**

The integrated vertical profile of the photon returns is modeled as a Gaussian surface with a subsurface decay. It contains four parameters: the mean (μ) and standard deviation (σ_h) of the unit Gaussian water surface, and the with an effective backscatter amplitude coefficient, B, analogous to Eqn 2.6, and an attenuation coefficient, α, of the subsurface exponential, assumed constant throughout the profile. In order to estimate the parameters, the deconvolution is solved separately, first for the two subsurface profile parameters, and then for the two surface profile parameters. To facilitate analysis, photons are aggregated into 5 cm vertical bins. Implementation identifies and excludes bins associated with non-exponential anomalies and the water body bottom prior to computing subsurface profile, as described in section 4.5.5.5.

The subsurface profile, analogous to Eqn. 2.6, is defined as:

$$y\_sub_j \quad = \sum_{i=1}^{i=j} \{\mathrm{B} \, * \exp(-2\alpha d)\}_{j-i+1} \, * X\_IRF_i * bin\_size$$

(4.11)

where X_IRFi is the discrete IRF, d is depth, α is the beam attenuation coefficient, and B is the subsurface backscatter amplitude parameter that includes both instrument and backscatter effects. Depth is corrected by c_l, the speed of light speed in water by

$$c_1 = n_1/n_2 \tag{4.11b}$$

where n_1 and n_2 are the refractive indices of air and water respectively (either fresh or salt water) depending on water body type, and assigned based on typical values obtained from the literature. (Note: The c_l correction was inadvertantly omitted in ATL13 Rel 6 resulting in an overestimation of α by ~ 30%, and will be reinstated in Rel 7).

The β and α are estimated using a fitting routine over the range of minus 8-sigma below the mode of the detrended water surface (upper limit) to the mean minus 3-sigma of the subsurface profile or -10m, whichever is shallower, i.e. higher (lower limit). The solution is implemented by minimizing the error difference between the integrated model and an exponential fit to the ATLAS photon histogram developed *a priori* using only the non-zero bins, or

$$\min \ \mathrm{Err} = \Sigma(\mathrm{y\_sub}_j - \mathrm{y\_obs}_j) \tag{4.11c}$$

However, other approaches (E.g. Method of Moments) can be used.

4.5.4 **Deconvolution of surface water profile**

Once B and α are estimated, μ and σ_h are estimated within the convolution over the unit profile in 4.12 below. The B and α already computed above are held constant.

$$y\_tot_j = \sum_{i=1}^{i=j} \left(\left\{ \frac{1}{\sqrt{2\pi\sigma_h^2}} \exp\left(\frac{-(d-\mu)^2}{2\sigma_h^2}\right) \right\} + \left\{ 0.5 * \left[1 + \mathrm{erf}\left(\frac{d-\mu}{\sigma_h\sqrt{2}}\right)\right] * \mathrm{B} * \exp(-2\alpha d) \right\}_{j-i+1} \right) * X\_IRF_i * bin\_size \tag{4.12}$$

The solution is achieved by iteration over μ and σ_h until the difference between the integrated model and the ATLAS histograms are minimized, similar to that described in 4.11b above. The solution is fit over the upper 80% of the integrated Gaussian height.

Results include the mean and standard deviation of surface height of that segment of surface photons analyzed, reported at the center of the segment, together with the lidar attenuation coefficient. Mean surface height is determined as the mean of the deconvolved surface Gaussian distribution.
The solution trades off the simplicity of a non-parametric approach to deconvolution, for a highly robust solution that is more practical given the global domain of all the lakes, rivers and other water bodies that ICESat-2 traverses.
For the MABEL cases tested from 2012-2014 during the development of this ATL13 ATBD, the results provide a generally robust solution with very good comparison with observed data as shown in Figures 6-4, 6-7, and 6-9.

4.5.5 **Implementation of deconvolution**

4.5.5.1 Identification of water signal photons.

Photons are identified through a process of histogramming the vertical profile of all photons over a water body detected within the range of +20m to -40 m of the water surface. Short segment lengths are defined on the basis of a fixed number of consecutive, ATL03 classified signal photons based on water body type. For water body Types 1, 2, 3, 4, 6, and 7, short segment lengths require 100 signal photons. For Type 5 (rivers), the number of signal photons in a short segment is set = 75 photons.. The coarse water surface is identified by computing the mode of each short segment within a group of three long segments. All photons within about 1.5 m+/- of the mode are selected for further analysis.

Photon Quality Flags: PODPPD flags from ATL03, available at the geosegment rate, are ingested and rescaled into the ATL13 algorithm at the short segment increments using the higher value whenever more than one ATL03 geosegment flag value exists within an ATL13 short segment. Short segments are processed where the ATL13-scaled PODPPD flag is equal to either “0” (NOMINAL), or “4” (CAL_NOMINAL). Short segment processing is terminated with any other PODPPD flag value.

<u>Partial Short Segments:</u> Note that After construction of the transect short segments based on the usual fixed number of signal photons (=s_seg1), additional signal photons will remain (count < s_seg1). These remaining photons are used to construct one additional “partial short segment” at the end of the transect if: i) the preceding short segment is non-anomalous, and ii) a least a fixed fraction of photons remains (count/s_seg1 >= nominally 0.10). Only the mean water surface

height and standard deviation are computed for this partial short segment using only the signal photons. If the fraction of signal photons < count/s_seg1, no short segment is constructed.

Partial short segments end on final signal photon, and non-signal photons beyond it are excluded from subsequent segment analysis.

4.5.5.2 Detrend observed data.

Observed data are detrended prior to deconvolution. Detrending is achieved on a long-segment basis (1000 signal photons or 10 short segments) on the basis of fitting a linear line through all the photon data within +/- 1.5 meters of the coarse water surface. Once identified, the photon data within the short segment are trimmed to include only the range +10m (above) the to -20m (below) the zero-mean water surface. Histograms of each long segment are created at 5 cm bin resolution.

In order to avoid inadvertently capturing subsurface photons associated with bottom reflection and machine error, such photons are further identified and further screened from processing using an empirical mirroring approach, as described in Section 5.3.3 (C).

4.5.5.3 Remove background from observed data.

Once histogrammed, the background density is subtracted off each 5 cm bin rectangle. Calculation of the background density is described in Section 4.3.2.1. The value is the same for each bin. If the bin rectangle value after subtracting is less than zero, assume the value is zero. For each short segment, two indices of saturation fraction are computed: i) the fraction of full saturation ($\geq$16 photons/shot) and ii) the fraction of near saturation (strong beam 10$\leq$ photons/shot< 16 weak beam > 4 photons/shot). The approach is to compute each based on the weighted average of the fractions of the corresponding geosegments contained within a short segment. The full and near saturation fractions for each geosegment are obtained from ATL03.

4.5.5.4 Alignment of IRF and observed histograms.

During deconvolution, it is critical that the beginnings of the IRF, the observed histogram, and the integrated histogram (convolved profile) all begin at the same bin, near or slightly above, the very top of the observed water surface. The IRF is resampled to 5 cm bins and normalized to 1.0. The beginning of the IRF is defined as $3\mathrm{x}\sigma_{h\_IRF}$ above the mean (to the left) of the best fit Gaussian to the IRF. The end of the IRF is defined as $8\mathrm{x}\sigma_{h\_IRF}$ below the mean (to the right) of the best fit Gaussian to the IRF. The beginning point to which the IRF is pinned is defined as

“$3x\sigma_{h\_obs}$ + 1.0m above the mean of the best fit Gaussian fit to the observed water surface returns.

4.5.5.5 Deconvolution

The “deconvolution“ is solved through constrained “convolution” of the IRF histogram with the unit (or true) water profile histogram. The solution is achieved by iterating through the four parameters of the unit water profile (mean, σ_h, β and α) until the mean, standard deviation and peak of integrated histogram best matches the observed (ATLAS) histogram, as described in sections 4.5.1 through 4.5.4.

4.5.6 **Estimation of coarse bottom topography, bathymetry, other subsurface anomalies**

ATL13 Release 002 provides an estimate of the along track bottom topography and water depth over the telemetry range, assuming favorable water clarity and cloudless skies. The overall approach relies on the above ATL13 analysis of surface water height combined with ideas developed by Nagle and Wright 2016, modified for ICESat-2 data.

During long segment histogramming, the vertical profile below the surface gaussian is checked for bottom and other anomalies, between the depth range of 12 standard deviations below the observed gaussian mean and the ATLAS telemetry window (20 m). The subsurface anomalies are initially computed relative to the apparent height of the normalized mean water body transect bin values. The actual subsurface or water depth is reported after correcting for refractive index (speed of light only). The algorithm is as follows:

1. The mean and standard deviation of the vertical subsurface profile for each long segment is computed. Also computed is the mean subsurface profile across all long segments in a water body transect.
2. Three anomaly threshold profiles are created; Anomaly threshold profiles, are defined as the 2* bin count of the mean subsurface histogram plus 3, 5 and 7 times the subsurface standard deviation of the subsurface bin counts of each long segment profile, respectively.
3. A subsurface anomaly profile is created corresponding to each threshold profile. For each profile, the corresponding height is identified for each occurrence when its bin value is greater than that of the threshold. The minimum height of all occurrences is then identified for each sigma level..
4. Three flags are designated “Flag 1 = Bottom or other subsurface anomaly detected”; Flag 2 = Subsurface anomaly detected, bottom possible”; Flag 3 = “Subsurface anomaly detected, bottom unlikely”
5. Whenever a long segment profile representing “2*mean+ 7*sigma” contains a minimum, it is designated as Flag 1 and its observed bin height is identified for that long segment.

6. For the remaining long-segments, when the profile representing "2*mean+5*sigma" contains a minimum, it is designated as Flag 2 and its bin height is identified for that long segment.
7. For the remaining long segments (not already determined for the 7*sigma and 5*sigma levels) above, when the profile representing "2*mean+3*sigma" contains a minimum, it is designated as Flag 3 and its bin height is identified for that long segment.
8. When no anomaly is found, designate as "No subsurface anomaly detected" or invalid.
9. The subsurface profile depths and location are computed as mean surface height minus the subsurface anomaly height, for refraction as described in Parrish et al., 2019.
10. The bottom anomalies for ATL13 are reported for each long segment at the short segment rate. Values reported are i) the actual water depth (m) from the mean water surface, ii) ΔX and ΔY offset to the location of each short segment, and iii) flag value.

An example of a retrieved bottom topography is shown for an ICESat-2 transect over Eagle Lake, CA on October 19, 2018. Results are reported at the subsurface rate. Additional subsurface anomalies not associated with bottom may also be detected.

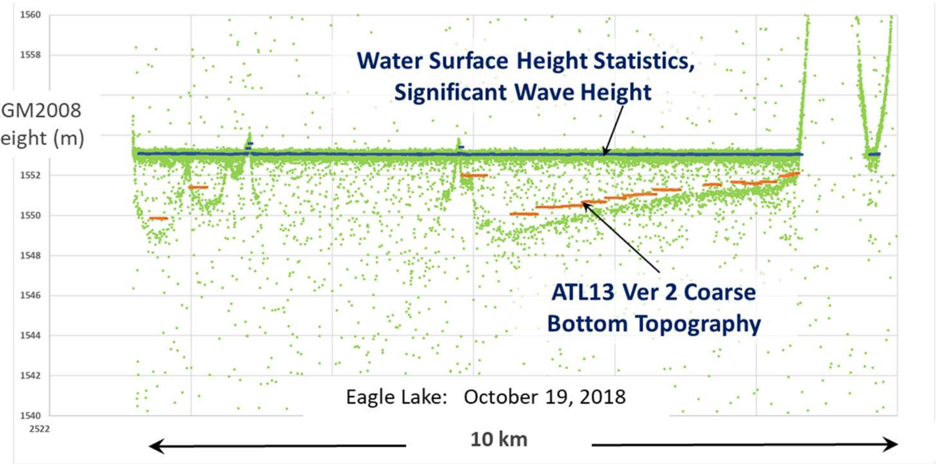

Figure 4-8 ATL13 Ver 002 identification of coarse bottom topography subsurface anomaly product for Eagle Lake CA on October 19, 2018..

4.6 Estimation of Mean Square Slope

Kay et al (2009) validated modeled surface by comparing their mean slopes and height standard deviation against empirical values. For mean square slope, a sample of 108 surfaces were within the range specified by Cox and Munk, or

$$\sigma_c^2 + \sigma_u^2 = \sigma_s^2 = 0.003 + 0.00512U \qquad (4.13)$$

Where U is in m/s and σ_c and σ_u are in radians (dimensionless).

Kay et al compared height standard deviation to the empirical formula given by Apel (1994), confirming,

$$\sigma_h = 0.005U_{10}^2 \qquad (4.14)$$

Where U10 is the 10m wind speed. Inverting 4.14 provides an estimate of the wind speed when σ_h is the unit surface profile obtained from the deconvolution algorithm. Combining 4.2, 4.13 and 4.14 yields the σ_s vs. σ_h relationship for wind driven waves,

$$\sigma_s^2 = 0.0549\sigma_h^{0.25} \qquad \sigma_h \leq 0.245 \text{ m} \qquad (4.15a)$$
$$\sigma_s^2 = 0.003 + 0.0724(\sigma_h)^{0.5} \qquad 0.245 < \sigma_h \leq 0.885 \text{ m} \qquad (4.15b)$$
$$\sigma_s^2 = 0.069\text{LOG}_{10}[\sigma_h] + 0.0748 \qquad 0.885 \text{ m} < \sigma_h \qquad (4.15c)$$

previously plotted in Figure 4-3.

4.7 Data Product Output

The overall procedure is to process global inland water body height products and associated products based on the ATL03 processing interval. The algorithm loops through the global inland water body database organized within regional basins during each processing period, completely analyzing all the ground tracks of one water body before proceeding to the next. Along- and cross- track data products are computed for all the new ground tracks observed for that water body since the previous processing period. Inland water bodies are delineated by shape files defined in the ATL13 Inland Water Body Shape mask.

4.7.1 Single Beam Analysis

4.7.1.1 Overall Scheme:

The principal data product for each water body type consists of along track mean height, rms height, slope, 532nm attenuation coefficient and bottom anomaly depth (if observed) for short segment lengths of each strong and weak beam, although several additional products are under evaluation. The ATL13 short segment resolution is 100 along track signal photons for all water bodies (default) except rivers which only require 75 signal photons as of Version 5. Also note that for the last short segment in a transect, the number of available signal photons is usually less than required and it is therefore designated as a “partial short segment” (See details in Section 4.5.5.1). Due to water and meteorology conditions, any segment length can vary from approximately 30 to several hundred meters. Data products are reported throughout the span of the identified water body as shown in Figure 3.3. Lidar data products are analyzed in orthometric units. Thus, data obtained from ATL03 in WGS84 ellipsoid reference data are converted to the EGM2008 Geoid.

Water bodies often have irregular shapes including dendritic or branching patterns. When an ATLAS transect crosses over an internal branch (completely entering then exiting the water body), then enters another branch of the same water body, the ATL13 analyses treats and reports each crossing as separate (not connected to the first) transect, even though the water body ID is the same.

Analyses occurs as follows. The heights of long segment lengths equaling 10 sequential short segments (~1000 signal photons) are computed including deconvolution of the satellite IRF and observed water body histogram. The mean height of each short segment is adjusted based on the mean deconvolved height of the Gaussian portion of the long segment. Very long segments composed of 30 subsequent short segments (~3000 signal photons) are required for estimation of the subsurface attenuation. All short and long segments within a given very long segment are assigned the same attenuation coefficient.

4.7.1.2 Water Body Reference Identification Scheme:

Each water body is assigned a unique 10 digit descriptive reference number for each shape in the ATL13 Inland Water Body Mask. The digits are defined as follows: 1 = water body type; 2 = size range in km2; 3 = citation of water body information; 4 through 10 = unique shape ID associated with a given type. ATL13 water body types are defined as: Type 1 = lake; Type 2 = known reservoir; Type 3 = Reserved for future use; Type 4 = Ephemeral water; Type 5 = river; Type 6 = transitional water (estuary or bay); Type 7 = transitional water (coastal); Type 8 = Reserved, Type 9 = Reserved. Each type possesses unique features including shapes, sizes, depths, and water surface dynamics.

The lake size range delimitation is as follows:
Size 1: Area >10,000 km^2; Size 2: 10,000 >Area ≥1,000; Size 3: 1,000 > Area ≥100, Size 4: 100 > Area ≥10; Size 5: 10 >Area ≥1; Size 6: 1 > Area ≥0.1; Size 7: 0.01 > Area; Size 8: Reserved; Size 9: Not assigned.

The lake type and size numbers are also used internally to control processing of selected water body types and sizes.

The current citations for the Inland Water Body shapes are:

Source 1= HydroLAKES (Messager, M.L., Lehner, B., Grill, G., Nedeva, I., Schmitt, O. (2016): Estimating the volume and age of water stored in global lakes using a geo-statistical approach. Nature Communications: 13603. doi: 10.1038/ncomms13603. Data is available at www.hydrosheds.org.)

Sources 2= Global Lakes and Wetlands Database (Lehner, B. and Döll, P. (2004): Development and validation of a global database of lakes, reservoirs and wetlands. Journal of Hydrology 296/1-4: 1-22.)

Source 3= Named Marine Water Bodies (ESRI http://mappingcenter.esri.com/index.cfm?fa=arcgisResources.gisData)

Source 4=GSHHG Shoreline (Wessel, P., and W. H. F. Smith, A Global Self-consistent, Hierarchical, High-resolution Shoreline Database, *J. Geophys. Res., 101*, 8741-8743, 1996)

Sources 5 through 9 = Reserved.

Source 5= Global River Widths from Landsat (Allen and Pavelsky (2018) Global Extent of Rivers and Streams. *Science*. https://doi.org/10.1126/science.aat0636),

Sources 6=Reserved, 7=Reserved, 8=Reserved, 9=Reserved.

4.7.1.3 Contingency Analyses Due to Water Body Type and Transect Length:

Contingencies are implemented based on transect length to provide reasonable estimates of height, the main data product over the full range of water body types.

Large transects: Large transects are defined as water body crossings or portions of water body crossings equal or greater than 30 short segments (~3000 signal photons). Large transects are analyzed according to the full algorithm described in Section 4.5 and shown in Figure 5.2. Subsurface parameters are estimated using the very long segment length equal to 30 short segments. Long segments, each comprised of 10 short segments, are analyzed with the full deconvolution algorithm, while using the subsurface parameters estimated from the very long segments.

Medium transects: Medium transects are those possessing from 10 to 29 short segments. Each long segment is analyzed as in Section 4.5 and Fig. 5.2 except fixed attenuation coefficients are assumed. In the case where a previous very long segment from that water body has been analyzed, the procedure is to apply the same (subsurface) coefficients for the subsequent ~~very~~ long segment(s). If no previous very long segments have been analyzed, use default values (α=0.5; beta=0.02). Proceed with deconvolution for long segments. For remaining 6 to 9 segments, use short segment transect contingency described below.

Short transects: Short transects are those possessing from 6 to 9 short segments. Use fixed subsurface parameters as follows. When this situation occurs after a long segment, assume the same subsurface parameters as that long segment and biases as described in 4.7.3.5. For small water bodies with no long previous long segments, report no attenuation coefficients (α, beta= invalid). Do not implement full deconvolution scheme. Rather, compute height adjustment as the difference between the mean of the Gaussian fitted to the top 80% of the observation histogram, and the mean of the Gaussian fitted to the top 50% of the IRF histogram. This difference is effectively implemented by assuming:

$$\text{Hd} = \text{Hdss} = \text{Invalid.} \tag{4.17a}$$

Compute the unit model σ_h as:

$$\sigma_h = \sqrt{\sigma^2_{h\_OBS\_80} - \sigma^2_{h\_IRF\_50}} \tag{4.17b}$$

Where $\sigma_h{}^2{}_{\_OBS\_80}$ is the variance of the Gaussian fitted (top 80%) to the observations and $\sigma_h{}^2{}_{\_IRF\_50}$ is variance of the gaussian fitted (top 50%) to the IRF.

If ABS[$\sigma_{h\_OBS\_80}{}^2$ - $\sigma_{h\_IRF\_50}{}^2$] $\leq$ 0.000025, assume $\sigma_h = 0.005$.
If [$\sigma_{h\_OBS\_80}{}^2$ - $\sigma_{h\_IRF\_50}{}^2$] < -0.000025, assume σ_h = invalid.

Very Short transects : Very short transects are those possessing from 1 to 5 short segments. When this situation occurs after a long segment, assume the same subsurface parameters as that long segment, and biases as described in 4.7.3.5. Report no subsurface parameters (α, beta= invalid) if no previous long segments. Compute height adjustment as the difference between the mean elevation of the observation photons for the detrended segments, and the mean of the Gaussian fitted to the IRF (top 50%). This difference is effectively implemented as follows:

$$\text{Hd} = \text{Hdss} = \text{Invalid.} \tag{4.17c}$$

Assume H_F, H_{EM}= invalid.

For all transects (large, medium, short and very short), assign Inland Water Segment Processing Flags as described in Section 4.8.1.

4.7.1.4 Rivers

ATL13 data products over rivers are treated as a unique inland water body type (Type=5). However, a global river mask was developed for Release 3 based on the RivWidth data product by Allen and Pavelsky, 2018. The new ATL13 river mask is merged with the current ATL13

Inland Water Body Mask. Typical specific features that are being addressed are i) very long rivers that can extend over hundreds of long segments, while possessing narrow widths of only several segments, ii) meandering and braided reaches that introduce a large fraction of surface height anomalies to the transect, and iii) steep water gradients depending on terrain and the orientation of ATLAS tracks.

The overall ATL13 surface elevation retrieval scheme is the same as for other water body types. River height analyses follows that described in Section 4.7.1.2.

4.7.2 **Significant Wave Height**

The significant wave height, H_S, is estimated as

$$H_S = 4 * \sigma_h \tag{4.17d}$$

Where σ_h is the estimated standard deviation of the unit water surface. H_S is invalid if σ_h is invalid.

4.7.3 **Estimation of Inland Water Body Bias**

The solution to the deconvolution yields the modeled vertical height distribution of both the true unit water surface and the subsurface backscatter based on the processed ATLAS photon returns. The vertical height difference between the observed profile (ATLAS histogram) and the true profile (unit water surface), or bias, can arise due observation, instrument, and retrieval algorithms errors. ATL13 considers two bias errors as described below.

4.7.3.1 Goodness of Fit Bias

Bias is introduced from imperfect fit of the assumed water surface profile distribution to the observed histogram. This bias, H_F, is estimated as the difference between the centroid elevations (or equivalently the mean heights) of the observed surface water histogram, H_{OH}, and fitted integrated water surface model histogram, H_{IM} over the Gaussian range (+/- $3\sigma_h$)., or

$$H_F = H_{OH} - H_{IM} \tag{4.18a}$$

First compute the Gaussian mean and standard deviation of both the observed histogram and the integrated model histogram using its upper 80%. Then calculate the difference in centroids between the two histograms by summing over all the vertical bins within +/- 3 standard deviations of the integrated Gaussian mean, or

$$H_F = \left[\frac{\sum_{i=1}^{n} (H_{OH_i} * d_i)}{\sum_{i=1}^{n} H_{OH_i}}\right] - \left[\frac{\sum_{i=1}^{n} (H_{IH_i} * d_i)}{\sum_{i=1}^{n} H_{IM_i}}\right] \tag{4.18b}$$

where i is bin number, *n* is the total number of bins within +/- 3 standard deviations of the integrated model mean, and d_i is bin depth.

4.7.3.2 Electromagnetic Bias

Elevation error is also introduced through observation bias of the wavy surface, slope, and view angle of the detector. This observation bias, H_{EM}, is computed based on the shift in centroid of the cross section of the joint probability density function of slope and height. Dudis (1986) derived a theoretical expression based on Longuet-Higgins (1963), or

$$H_{EM} = 3\pi S_s(\nu^2 - 1) * \sigma_h \tag{4.19}$$

where, S_s is the significant slope defined after Huang et al. (1983),

$$S_s = \sigma_h / \lambda_{pk} \tag{4.20}$$

σ_h is the standard deviation of the derived unit gaussian, and λ_{pk} is the wavelength at its spectral peak (defined in Section 4.7.3.3 below). The parameter ν is the normalized satellite view angle or

$$\nu = \theta / (\sigma_s^2)^{0.5} \tag{4.21}$$

where θ is the satellite view angle (E.g. from ATL03, nominally 0.006 rad reference track side beam need other off pointing angles) and σ_s is the root-mean-square wave slope derived in Eqn 4.15.

For the above, if σ_h is invalid, then H_{EM}, S_s, and ν are also invalid.

4.7.3.3 Wavelength and Wave Period at Spectral Peak

The wavelength at the spectral peak, λ_{pk}, is estimated from the detrended, long segment, signal photons assuming deep water. First, the parameter T_{pk_ATLAS} is estimated as the longest time between two sequential zero up-crossing wave surface signal photons within a long segment (See Figure 4-8 below for definition of zero up-crossing). Only those photons within +/- 3 σ of the detrended zero mean surface are employed. From this, the wavelength at spectral peak, λ_{pk}, and wave period at spectral peak (assumes deep water waves), T_{pk}, are estimated as

$$\lambda_{pk} = T_{pk\_ATLAS} * V_{gt} \tag{4.22a}$$

$$T_{pk} = ((\lambda_{pk} * 2\pi / g)^{0.5} \tag{4.22b}$$

respectively, where g is acceleration due to gravity (9.807 m/s^2) and V_{gt} is the ATLAS ground track speed (Obtained directly from ATL03 or nominally 7000m/s).

4.7.3.4 Reported ATL13 Height Data Product

ATL13 reports heights at the short segment level. The short segment height product is computed as the sum of the following elements:

1. H_d -The adjusted height due to deconvolution of the long segments.. ,.
When deconvolution is implemented for long or very long segments:

$$H_d = \mu - 3\sigma_{h\_IRF\_80} - \mu_{detrend} \tag{4.23a1}$$

Where μ is the mean of the true water surface defined in Eqn 4.12, $\sigma_{h\_IRF\_80}$ is the standard deviation of the IRF, and $\mu_{detrend}$ is the residual mean height of the integrated, fully convolved Gaussian portion of the fitted histogram of the apparent profile after detrending. (Note: subtraction of the $\sigma_{h\_IRF\_80}$ and $\mu_{detrend}$ terms are required due to a coding requirement in the deconvolution scheme).

For short transects, assume Hd = Hdss = as defined in Section 4.7.1.2, Equations 4.17a and 4.17c.

2. The H_F and H_{EM} biases.

3. H_M - The apparent mean of the surface signal photons originally defined by the mode of the short segment heights before detrending. Only the surface signal photons of each segment that fall within +/- 3 sigma of the short segment mode (using the integrated histogram sigma) are used in the calculation of the mean.

4. FPB_corr – The first photon bias correction as identified in 4.7.3.6 below.

$$H_{ATL13\_EGM2008} = H_M + H_d + H_F - H_{EM} - FPB\_corr. \tag{4.23a}$$

If H_F is designated invalid, then replace Eqn. 4.23a with 4.23b below,

$$H_{ATL13\_EGM2008} = H_M + H_d - H_{EM} - FPB\_corr. \quad (4.23b)$$

If H_F and H_{EM} are both designated invalid, then replace Eqn. 4.23a with 4.23c below,

$$H_{ATL13\_EGM2008} = H_M + H_d - FPB\_corr. \quad (4.23c)$$

The ATL13 reporting elevation above the ellipsoidal height (WGS84) is also provided, or

$$H_{ATL13\_WGS84} = H_{ATL13\_EGM2008} + H_{GeoidEGM2008}. \quad (4.24)$$

In any case where **H_bias_fit**, **H_bias_EM**, or **H_d** are invalid, exclude the invalid term(s) from the calculation of te short segment heights $H_{ATL13\_EGM2008}$ and H_{ATL13_WGS84}.

Product Output Table reports $H_{ATL13\_EGM2008}$, H_{ATL13_WGS84}, H_M, H_F, H_{EM} and FPB_corr, as well as quality flags for H_d, H_F and H_{EM}.

The height and geolocation are reported at the closest signal photon location.

4.7.3.5 Contingency for transects less than one long segment.

If the number of short segments is less than the ten required for one long segment but is preceded by a complete long segment, then assume that within Eqn 4.23a, H_F and H_{EM} are equal to that in the previous long segment. If the number of short segments is less than the ten required for one long segment and is not preceded by a complete long segment, then assume that H_F and H_{EM} are invalid.

4.7.3.6 First photon bias correction.

First photon bias (FPB) is the term applied to the reduction in the number of received photons actually recorded by the ATLAS detectors for high photon rates of return. This can occur for each detector for a short interval of time after a series of initial photon are received. The actual count is thus biased on the low side and depends on the rate of return.

ATL13 provides a correction for users to apply, as it is not automatically applied. It corrects the estimated mean water surface height in Equations 4.23 and 4.24 using the FPB correction procedure outlined in the CAL_19 Calibration Product of ATL03. The following steps are employed:

i) First, the apparent width of the full-width half-max (FWHX) standard deviation of the ATL13 surface is computed based on the previously estimated standard deviation (σ_h) or

$$\sigma_{h\_OBS\ FWHM} = 2.355\ \sigma_{h\_OBS\_80} \quad [m] \quad 4.24b$$

or in terms of time of flight $\sigma_{h\_OBS\ FWHM} = 15.7*\sigma_{h\_OBS\_80}$ [ns] 4.24c
(where, in Chapter 5, $\sigma_{h\_OBS\_80}$ = *detrend_sigma2* for long segments or *L_surf_inc_stdev2* for contingency cases), and converted time of flight by 2*3.333 ns/m.
ii) Second, the apparent strength of the return in terms of photons/shot is estimated based on the previously computed short segment photon rate, or

Strength_ATL13 sseg = s_seg1*0.7/Length_sseg [pe/shot] 4.24d
where 0.7 equals spacecraft velocity (m/s) divided by 10,000 or distance per Atlas shot.
iii) Third, dead time is assumed equal to the mean of the detectors used for each beam.
iv) Fourth, the FPB correction, or ffb_corr from ATL03, is obtained in terms of native ps units.
v) Finally, the mean short segment water surface height FTB correction is estimated in cm as

Segment_fpb_correction = 0.00015 * ffb_corr [m] 4.24e

Note: The user should subtract the_fpb_correction from the mean height products such as ht_ortho (EGM2008) and ht_water_surf (WGS84). The above correction is not applied when all detectors are saturated. A future ATL03 correction for such severely biased returns is will be applied to future ATL13 Releases.

4.7.3.7 Inclusion of best publicly available DEM.

As indicated in the ATL13 output table, also included is the best publicly available Digital Elevation Model) DEM (based on resolution and quality) at the ATL13 short segment rate together with the source of the DEM. DEM location is assigned to the short segment index photon. DEM selection sources include all available from ATL03. The currently available selection source and hierarchy among those are:

1) ArcticDEM
2) DTU13 Mean Sea Surface (MSS).
3) Reference Elevation Model of Antarctica (REMA)
4) Multi-Error-Removed Improved-Terrain (MERIT) DEM.

Inclusion of additional future ATL03 DEM products may alter the above hierarchy.

4.7.4 Dynamic Atmospheric Correction and Ocean Tides

Three fields associated with dynamic atmospheric correction and ocean tides were added to the output table. They include: i) the Dynamic Atmospheric Correction (DAC) that includes inverted barometer (IB) effect (±5 cm), ii) the ocean tides that include diurnal and semi-diurnal (harmonic analysis (±4 m), and iii) the long period equilibrium tide self-consistent with ocean tide model (± 0.04 m). Although the above values are made available at short segment rate for all water body types, they are not included in the standard inland water height products, They are provided mainly for convenience use at user's discretion, for possible use with the transitional tidal and coastal water (types 6 and 7) and the largest lakes of Type 1 (~> 10,000 km^2).

4.8 Quality and classification flags throughout flow of analysis

Quality flags are provided at the following steps in the analysis:

4.8.1 Inland Water Segment POD/PPD Flag

Composite POD/PPD flag that indicates the quality of input geolocation products for the utilized ATL03 segments on an ATL13 short segment output basis. A non-zero value may indicate that geolocation solutions are degraded or that ATLAS is within a calibration scan period (CAL). Flags set as follows:0=NOMINAL; 1=POD_DEGRADE; 2=PPD_DEGRADE; 3=PODPPD_DEGRADE; possible CAL values are: 4=CAL_NOMINAL; 5=CAL_POD_DEGRADE; 6=CAL_PPD_DEGRADE; 7=CAL_PODPPD_DEGRADE

4.8.2 Inland Water Segment Processing Flag

This flag describes the level of processing using to estimate the surface and subsurface parameters. Set Flags as follows:
= 7 designates 30 or more short segments analyzed using the full deconvolution scheme,
= 6 designates10 to 29 short segments used,
= 5 designates 8 to 9 short segments used,
= 4 designates 6 to 7 short segments used
= 3 designates 3 to 5 short segments used
= 2 designates 2 short segments used
= 1 designates 1 short segment used
= 0 designates partial short segment.

4.8.3 Background Flag

This flag describes the intensity of the background rate in each short segment. The flags are:
= 0 if ***bckgrd_dnsty_50sht_bin_Sseg ≤ bckgrd_dnsty_threshold1***
= 1 if ***bckgrd_dnsty_threshold1 > bckgrd_dnsty_50sht_bin Sseg≤ bckgrd_flag_threshold2***

= 2 if ***bckgrd_dnsty_threshold2*** > ***bckgrd_dnsty_50sht_bin Sseg*** ≤ ***bckgrd_dnsty_threshold3***
= 3 if ***bckgrd_dnsty_threshold3*** > ***bckgrd_dnsty_50sht_bin Sseg*** ≤ ***bckgrd_dnsty_threshold4***
= 4 if ***bckgrd_dnsty_threshold4*** > ***bckgrd_dnsty_50sht_bin Sseg*** ≤ ***bckgrd_dnsty_threshold5***
= 5 if ***bckgrd_dnsty_threshold5*** > ***bckgrd_dnsty_50sht_bin Sseg*** ≤ ***bckgrd_dnsty_threshold6***
= 6 if ***bckgrd_dnsty_50sht_bin*** > ***bckgrd_dnsty_threshold6***

bckgrd_dnsty_threshold1 = 0.001 (counts per bi per Lseg)
bckgrd_dnsty_threshold2 = 0.010 (counts per bin per Lseg)
bckgrd_dnsty_threshold3 = 0.050 (counts per bin per Lseg)
bckgrd_dnsty_threshold4 = 0.10 (counts per bin per Lseg)
bckgrd_dnsty_threshold5 = 0.300 (counts per bin per Lseg)
bckgrd_dnsty_threshold6 = 0.500 (counts per bin per Lseg)

4.8.4 **Bias Fit Flag**

The bias fit flag

= -3 when $H_F < -0.10$ (m)
= -2 when $-0.10 \leq H_F < -0.05$
= -1 when $-0.05 \leq H_F < -0.01$
= 0 when $-0.01 \leq H_F < 0.01$ (m)
=1 when $0.01 \leq H_F < 0.05$
=2 when $0.05 \leq H_F < 0.10$
=3 when $0.10 \leq H_F$
=4 when H_F is invalid.

4.8.5 **EM Bias Flag**

The EM Bias Flag is defined as follows:

= -3 when $H_{EM} < -0.10$ (m)
= -2 when $-0.10 \leq H_{EM} < -0.05$
= -1 when $-0.05 \leq H_{EM} < -0.01$
= 0 when $-0.01 \leq H_{EM} < 0.01$ (m)
=1 when $0.01 \leq H_{EM} < 0.05$
=2 when $0.05 \leq H_{EM} < 0.10$
=3 when $0.10 \leq H_{EM}$
=4 when H_{EM} is invalid.

4.8.6 **Short Segment Length Flag**

The Short Segment Length Flag is defined as follows:
== 0 if ***sseg_length*** < 10 (meters)
= 1 if 10 ≤ ***sseg_length*** < 20 (meters)
= 2 if 20 ≤ ***sseg_length*** < 30 (meters)
= 3 if 30 ≤ ***sseg_length*** < 50 (meters)
= 4 if 50 ≤ ***sseg_length*** < 75 (meters)
= 5 if 75 ≤ ***sseg_length*** < 100 (meters)
= 6 if 100 ≤ ***sseg_length*** < 150 (meters)
= 7 if 150 ≤ ***sseg_length*** < 200 (meters)
= 8 if 200 ≤ ***sseg_length*** < 300 (meters)
= 9 if 300 ≤ ***sseg_length***

4.8.7 **Long Segment Length Flag**

= 0 if ***Lseg_length*** < 500 (meters)
= 1 if 500 ≤ ***Lseg_length*** < 1500 (meters)
= 2 if 1500 ≤ ***Lseg_length*** < 3000 (meters)
= 3 if 3000 ≤ ***Lseg_length***

4.8.8 **Clouds Flag**

Cloud confidence flags derived in ATL09 are convert to ATL13 short segment rates using a nearest neighbor approach. They include Cloud_Flag_ASR, Cloud_Flag_Atm and Layer_Flag.

4.8.9 **Flags Associated with Snow and Ice**

The ATL13 snow and ice flags are (snow_ice_ATL09), obtained from the ATL09 Snow_Ice flag and the NOAA GMASI product, are assigned at the short segment rate as: 0 = ice free water, 1 = snow free land, 2 = snow, and 3 = ice. When there is more than one overlap, they are assigned the greatest value.

4.8.10 **Flags Associated with Surface Temperature**

ATL13 reports the ATL09 MET surface (skin) temperature at the short segment rate based on a linear interpolated nearest neighbor approach.

4.8.11 H_d Adjust Flags

The H_d Adjust flags are included that indicate the level of surface water height adjustment due to deconvolution.

= -4 when $H_d < -0.20$ (m)
= -3 when $-0.20 \leq H_d < -0.1$
= -2 when $-0.10 \leq H_d < -0.05$
= -1 when $-0.05 \leq H_d < -0.01$
= 0 when $-0.01 \leq H_d < 0.01$
=1 when $0.01 \leq H_d < 0.05$
=2 when $0.05 \leq H_d < 0.10$
=3 when $0.1 \leq H_d < 0.20$
=4 when $0.20 \leq H_d$
=5 when H_d is invalid.

4.8.12 Detrended Surface Quality Flags

Flags indicate the standard deviation of the Gaussian fit to the detrended surface at both long and very long segment scale.

Long segment standard deviation flag:
= 0 if ***detrend_sigma2*** < 0.5 (meters)
= 1 if 0.5 ≤ ***detrend_sigma2*** < 1.5 (meters)
= 2 if 1.5 ≤ ***detrend_sigma2*** < 2.5 (meters)
= 3 if 2.5 ≤ ***detrend_sigma2*** < 3.5 (meters)
= 4 if 3.5 ≤ ***detrend_sigma2*** < 4.5 (meters)
= 5 if 4.5 ≤ ***detrend_sigma2*** < 5.5 (meters)
= 6 if 5.5 ≤ ***detrend_sigma2*** < 6.5 (meters)
= 7 if 6.5 ≤ ***detrend_sigma2*** < 7.5 (meters)
= 8 if 7.5 ≤ ***detrend_sigma2*** < 8.5 (meters)
= 9 if 8.5 ≤ ***detrend_sigma2***

For short transects (where ***detrend_sigma2*** is not calculated), apply the above flag based on the value of ***L_surf_inc_stdev2*** instead.

Very long segment standard deviation flag:
= 0 if ***detrend_sigma2_Lsub*** < 0.5 (meters)

= 1 if 0.5 ≤ ***detrend_sigma2_Lsub*** < 1.5 (meters)
= 2 if 1.5 ≤ ***detrend_sigma2_Lsub*** < 2.5 (meters)
= 3 if 2.5 ≤ ***detrend_sigma2_Lsub*** < 3.5 (meters)
= 4 if 3.5 ≤ ***detrend_sigma2_Lsub*** < 4.5 (meters)
= 5 if 4.5 ≤ ***detrend_sigma2_Lsub*** < 5.5 (meters)
= 6 if 5.5 ≤ ***detrend_sigma2_Lsub*** < 6.5 (meters)
= 7 if 6.5 ≤ ***detrend_sigma2_Lsub*** < 7.5 (meters)
= 8 if 7.5 ≤ ***detrend_sigma2_Lsub*** < 8.5 (meters)
= 9 if 8.5 ≤ ***detrend_sigma2_Lsub***

4.9 Data Product Precision and Evaluation

The Inland Water Data Product quality relies on the precision of the ATL03 georeferenced photons and associated products which are evaluated prior to their use within ATL13. The plan for evaluating ATL13 data products is presented in Section 4.9.2.

4.9.1 ICESat-2 Precision

The precision of the ICESat-2 retrieval is estimated from root mean square of five error sources:

i) Radial orbit error, RO_{RMS}
ii) Tropospheric delay error, TD_{RMS}
iii) Forward scattering error, FS_{RMS}
iv) Geolocation Knowledge uncertainty, GK_{RMS}
v) ATLAS ranging precision per photon, σ_{RMS}.

Actual rms error for each source are obtained from ATL03. The current default values are $RO_{RMS} = 4.0$ cm, $TD_{RMS} = 3$ cm, $FS_{RMS} = 3$ cm, $GK_{RMS} < 0.5$ cm (over water) and $\sigma_{RMS} = 24.0$ cm. For 100 photon short segments, the ranging precision is estimated as $\sigma_{RMS100} = \sigma_{RMS}/(100^{1/2}) = 24/(100)^{1/2} = 2.4$ cm.

The overall ensemble error per 100 inland water photons is estimated as

$$\sigma_{ICESat2} = \sqrt{[RO^2_{RMS} + TD^2_{RMS} + FS^2_{RMS} + GK^2_{RMS} + \sigma^2_{100\ shots}]}$$
$$= \sqrt{37.25} = 6.1 \text{ cm} \qquad (4.29)$$

This precision error is updated as post-launch ATLAS data sets are evaluated.
Previously analyzed MABEL data (Jasinski et al., 2016) scale well with the anticipated ATLAS observations. Results indicate a MABEL water return rate of 0.36 to 2.90 photon events per meter (pe/m) depending on surface and atmospheric conditions. The ranging precision for a 100 shot segment would vary from 2.0 to 5.0 cm, respectively.

We also offer standard tide corrections for the coastal zone.

4.9.2 **Data Product Evaluation**

A plan for evaluating the Inland Water Data Product was formulated during the development of ATL13 by collaborating with relevant U.S. agencies, university researchers, and other various organizations. Data product quality is achieved through monitoring, assessment and validation at various levels of effort depending on available resources. The overall approach is i) to compare ATL13 data products with *in situ* data and satellite radar altimetry where available, ii) evaluate several components of the ATL13 algorithm through threshold monitoring with model diagnostics, and iii) conduct in situ validation and calibration when resources are available or synergistic field opportunities arise. Evaluation can be conducted over all ATL13 Inland Water Body types including lakes, reservoirs, rivers, estuaries and near shore coasts. Sites are located primarily in the US and North America, but also at several international sites. Every effort is made to be aware of, and participate in, other sponsored field programs by NASA and other agencies including satellite mission CAL/VAL plan.

4.9.2.1 External Products Available for Monitoring ATL13 Data

Monitoring refers to active and continuous evaluation of ICESat-2 data-product parameters, primarily through data visualizations and threshold monitoring. Monitoring can occur through comparison of ATL13 time series data plots with other independent data. Time series can be evaluated with respect to mean water surface segment heights, variances, slopes, significant wave height, subsurface attenuation, presence of ice, and identifiable bottom location, as a function of water body type, location, water clarity and prevailing meteorological conditions. For the Inland Water Data Product, monitoring occurs principally by leveraging off existing databases supported by numerous organizations in the US and internationally, including radar altimetry missions. Principal sources include:

a) Reservoir and lake elevations based on satellite radar altimetry from Jason 3, Sentinel 3A and 3B sensors and compiled at online archives. Example online data bases include:

i) Center for Topographic Studies of the Ocean and Hydrosphere (CTOH) data
    http://ctoh.legos.obs-mip.fr/data
ii) HYDROWEB (Theia, LEGOS, other international)
    http://hydroweb.theia-land.fr
iii) Global Reservoir and Dam Database (GWSP)
    http://globaldamwatch.org/grand/
iv) G-REALM (USDA)

https://ipad.fas.usda.gov/cropexplorer/global_reservoir
v) Global River Database
https://gaia.geosci.unc.edu/rivers/
vi) River and Lakes (ESA) (historical data)
http://altimetry.esa.int/riverlake/shared/main.html
vii) Database for Hydrological Time Series of Inland Waters (DAHITI)
https://dahiti.dgfi.tum.de/en/
viii) Global Water Monitor
https://blueice.gsfc.nasa.gov/gwm/lake/Index

b) *In situ* water level gauges primarily at reservoirs, lakes, and other water bodies monitored by the: i) US Geological Survey (USGS), ii) National Oceanic and Atmospheric Administration (NOAA), iii) Bureau of Land Management (BLM), and iv) US Army Corps of Engineers (USACE). Although there are hundreds of available sites, the principal water bodies being considered include Lake Fort Peck, MT; Lake Mead, NV; all Great Lakes; Lake Tahoe, CA; Chesapeake Bay; Lake Teshekpuk and Toolik Lake, AK; Lake Issyk-Kul, Kyrgyzstan; water bodies within the Mississippi, Connecticut, and Yukon River basins. All these water bodies are well gaged by the USGS, NSF, or other US agencies with accessible online data. Analyses can include evaluation mainly of root mean square error, bias, and mean absolute error. Databases include:

i) NOAA Great Lakes Environmental Research laboratory
https://www.glerl.noaa.gov/data/wlevels/levels.html#observations
ii) Lake Levels (GWSP)
http://www.lakelevels.info
iii) Lakes Online
http://www.lakesonline.com/
iv) USGS National Water Information System
https://waterdata.usgs.gov/nwis

4.9.2.2 Assessment and Validation Activities

Assessment refers to a single post-launch evaluation of ICESat-2 data-product accuracy and/or precision, generally against in situ data. Validation' refers to an aggregate of post-launch 'assessments' to determine global ICESat-2 accuracy or precision. Instruments will be included that observe water surface height statistics, wind speed and direction, and basic water quality constituents that affect optical transmission and turbidity such as mineral particles, dissolved organic carbon and chlorophyll, among others.

Several opportunities have been planned with the following programs:

a) <u>United States Great Lakes and near shore transitional zones.</u> Field experiments are planned in collaboration with the Joint Airborne Lidar Bathymetry Technical Center of Expertise (JALBTCX) mission performs operations, research, and development in airborne lidar bathymetry to support the coastal mapping and charting requirements of the US Army Corps of Engineers (USACE), the US Naval Meteorology and Oceanography Command, the National Oceanic and Atmospheric Administration (NOAA), and the U.S. Geologic Survey (USGS). JALBTCX executes survey operations worldwide using the Coastal Zone Mapping and Imaging Lidar (CZMIL) system and other industry-based coastal mapping and charting systems. CZMIL is integrated with an ITRES CASI-1500 hyperspectral imager and a true-color digital camera. CZMIL collects 10-kHz lidar data concurrent with 5-cm digital true-color and 48-band hyperspectral imagery. JALBTCX research and development supports and leverages work in government, industry, and academics to advance airborne lidar and coastal mapping and charting technology and applications. An example of planned JALBTCX coverage in 2018 and 2019 is shown below.

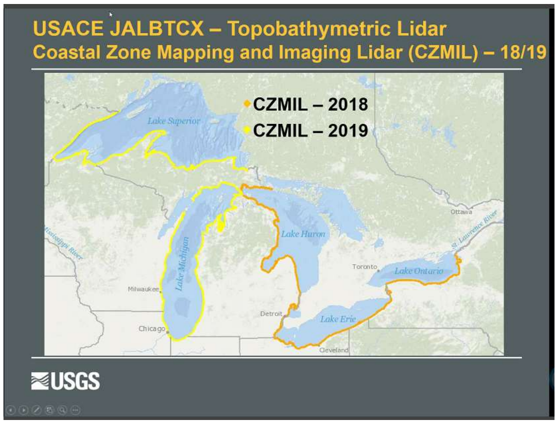
USACE JALBTCX – Topobathymetric Lidar
Coastal Zone Mapping and Imaging Lidar (CZMIL) – 18/19

Figure 4-9 An example of planned US Army Corps of Engineers Coastal Zone Mapping and Imaging Lidar Surveys, 2018-19. http://shoals.sam.usace.army.mil/CZMIL.aspx

b) <u>Alaska Sites</u>

ATL13 has planned collaboration with researchers from the Alaska USGS, the University of Alaska, Fairbanks, and NASA GSFC, for in situ monitoring during overflights. Sites include NSF sponsored Lakes Teshekpuk and Inigot, Toolik Lake; and the Yukon River and the Mackenzie River deltas as shown below. Participation in NASA GSFC field experiments at the mouths of the Yukon River and the near-shore region off Northern Alaska to the Mackenzie River mouth are currently under consideration.

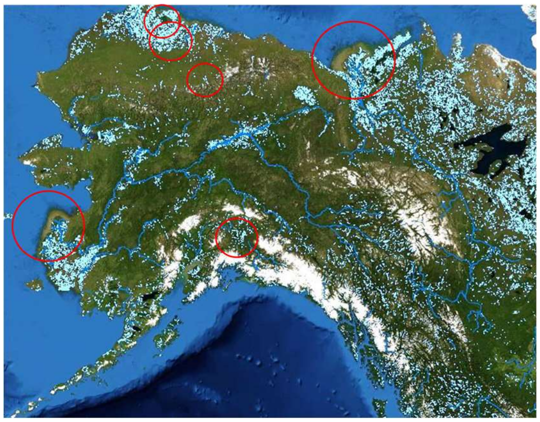

Figure 4-10 Examples of potential collaborative calibration/validation sites (red circles) in Alaska.

c) <u>Mid-Latitude Lakes and Reservoirs</u>
Assessment sites include collaboration a several sites with various groups including the Great Lakes (JALBTCX, Illinois State geological Survey), Lakes Mead (US Bureau of Reclamation), Lake Fort Peck (USACE), Lake Tahoe and Western Lake Erie (Kent State). For the Great Lakes, ATL13 is collaborating with efforts to measure Great Lakes surface water conditions at the locations shown below.

Figure 4-11 Lake level gauge and monitoring stations on the Great Lakes.
https://www.glerl.noaa.gov/data/wlevels/levels.html#monitoringNetwork

d) <u>Transitional Water Bodies (Estuaries, Bays, Near Shore Coasts)</u>

Principal areas would include the Chesapeake Bay, and the estuaries of the Mississippi/Atchafalaya River deltas, Everglades, Mackenzie River, and Yukon River, together with the near shore regions surrounding the East and West coast of the continental U.S. and Northern Alaska.

Collaboration with personnel from NOAA STAR for in situ measurements on the Chesapeake Bay is planned.

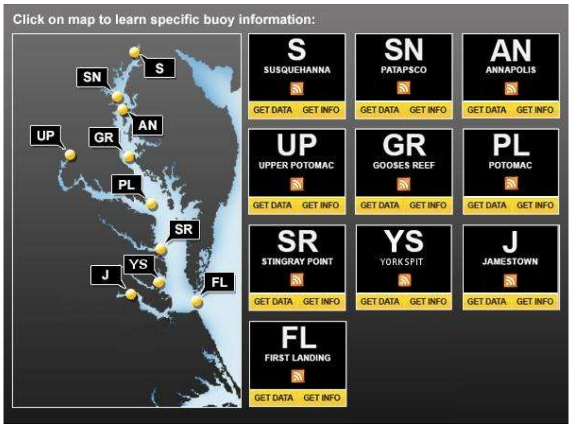
Click on map to learn specific buoy information:

Figure 4-12 Examples of potential collaborative calibration/validation sites in Chesapeake Bay region, based on buoy locations. https://buoybay.noaa.gov/locations

4.9.2.3 Calibration Activities and Measurements

Data product calibration consists of the application of post-launch ‘assessments’ or ‘validations’ to either ICESat-2 instrument settings, or to future data releases, in an effort to improve measurement accuracy and/or precision. Necessary measurements for validation include the following:
i) Meteorology: Wind speed and direction, optical depth, cloud cover
ii) Water Surface Physical Properties: GPS, wave height statistics, temperature, water depth
iii) Subsurface Radiative Properties: Upwelling and downwelling radiance, at 532 nm.
iv) Water Inherent Optical Properties: subsurface attenuation, suspended particulate matter, CDOM, Chlorophyll, temperature, salinity, turbidity (NTU) and Secchi Depth.

5.0 ALGORITHM IMPLEMENTATION – PLAIN LANGUAGE SUMMARY

5.1 Outline of Procedure

The overall procedure is to process global inland water bodies on a regular basis based on the ATL03 processing interval. The algorithm loops through the global inland water body database organized within regional basins, during each processing period, completely analyzing all the ground tracks of one water body before proceeding to the next. Along- track data products are computed for all the new ground tracks observed for that water body since the previous processing period.

Inland water bodies are delineated by shape files defined in the ATL13 Inland Water Body Shape mask. Inland water bodies include lakes, reservoirs, rivers, and transitional waters including estuaries, bays, and near coasts. The Regional Basin contains all the water bodies within its boundaries.

Specific steps in the implementation of the Inland Water Body Height algorithm are detailed below. Overview and detailed flowcharts are provided in Figures 5-1 and 5-2, respectively.

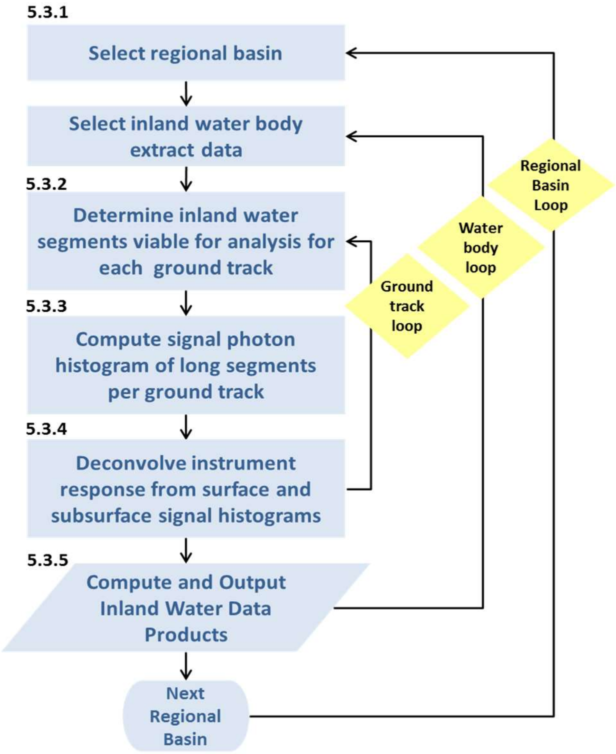

Figure 5-1 Overview Flowchart of Inland Water Height Algorithm for ATL13.

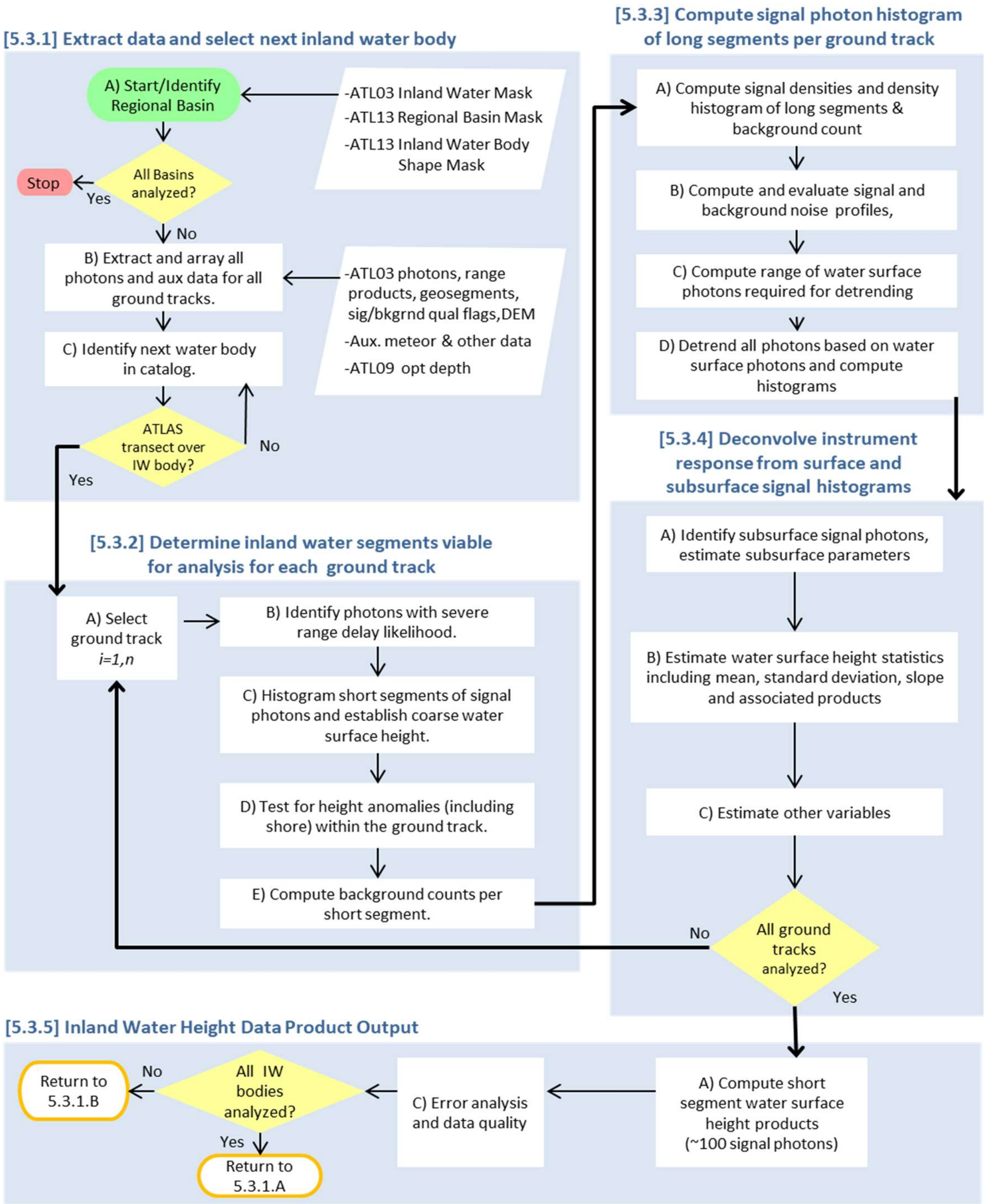

Figure 5-2 Detailed Flowchart of Inland Water Height Algorithm for ATL13

5.2 Input Variables and Parameters

Table 5-1 Input Variables for ATL13 Inland Water Algorithm

Name	Description	Units	ATL0x/Other Source
Water_body_type	Water body type	unitless	ATL13 Inland Water Body mask. See 4.7.1.2
Elap_time	Elapsed GPS seconds since start of the granule for a given photon.	seconds	ATL03/gtx/heights/delta_time
P_sig_flag	Confidence level associated with each photon event selected as signal (0-noise. 1- added to allow for buffer but algorithm thinks is noise, 2-low, 3-med, 4-high).	counts	ATL03/gtx/heights/signal_conf_ph
RGT	The reference ground track (RGT) is the track on the Earth at which a specified unit vector within the observatory is pointed. Under nominal operating conditions, there will be no data collected along the RGT, as the RGT is spanned by GT2L and GT2R. During slews or off-pointing, it is possible that ground tracks may intersect the RGT. The ICESat-2 mission has 1,387 RGTs.	unitless	ATL03/orbit_info/rgt
cycle_number	Tracks the number of 91-day cycles in the mission, beginning with 01. A unique orbit number can be determined by subtracting 1 from the cycle_number, multiplying by 1,387 and adding the RGT value.	unitless	ATL03/orbit_info/cycle_number
grtrck	Array of 6 groundtracks (GT1L through GT3R) contained within each RGT	unitless	ATL03/
P_ht	Height of each received photon. Bounce point height relative to WGS-84 ellipsoid.	meters	ATL03/gtx/heights/h_ph

Name	Description	Units	ATL0x/Other Source
P_lat	Latitude of each received photon. Computed from the ECF Cartesian coordinates of the bounce point.	degrees	ATL03/gtx/heights/lat_ph
P_lon	Longitude of each received photon. Computed from the ECF Cartesian coordinates of the bounce point.	degrees	ATL03/gtx/heights/lon_ph
geoid	Geoid value per geosegment (EGM2008)	Meters	ATL03/gtx/geophys_corr_geoid
segment_id	~20m geosegment identification number	unitless	ATL03/gtx/geolocation/segment_id
ph_index_beg	The index of the first photon in a given segment.	unitless	ATL03/gtx/geolocation/ph_index_beg
segment_ph_cnt	Number of photons in geosegments 1:i	unitless	ATL03/gtx/geolocation/segment_ph_cnt
surf_type	Surface type as determined by ATL03 surface masks	unitless	ATL03/gtx/geolocation/surf_type
segment_length	The along-track length of the along-track segment. Nominally these are 20 meters, but they vary from 19.8 meters to 20.2 meters.	meters	ATL03/gtx/geolocation/segment_length
dist_ph_across	Across-track distance projected to the ellipsoid of the received photon from the reference ground track. This is based on the along-track segment algorithm described in section 3.1.	meters	ATL03/gtx/heights/dist_ph_across
dist_ph_along	Along-track distance in a segment projected to the ellipsoid of the received photon, based on the along-track segment algorithm. Total along-track distance can be found by adding this value to the sum of segment lengths measured from the most recent equatorial crossing	meters	ATL03/gtx/heights/dist_ph_along
CAL_19	First photon bias correction table	picosec	ATL03/ancillary_data/calibrations/ first_photon_bias

Name	Description	Units	ATL0x/Other Source
P_time_start	start time of granule	seconds	ATL03/metadata/granule_start_seconds
geoid	Geoid height above WGS-84 reference ellipsoid (range -107 to 86 meters).	meters	ATL03/gtx/geophys_corr/geoid
dac	Dynamic atmospheric correction (DAC) includes inverted barometer (IB) effect (±5 cm).	meters	ATL03/gtx/geophys_corr/dac
tide_ocean	Ocean tides including diurnal and semi-diurnal (harmonic analysis (±4 m).	meters	ATL03/gtx/geophys_corr/tide_ocean
tide_equillibrium	Long period equilibrium tide self-consistent with ocean tide model (± 0.04 m).	meters	ATL03/gtx/geophys_corr/tide_equillibrium
tx_pulse_width_lower	Average distance between lower threshold crossing times measured by start pulse detector.	seconds	ATL03/atlas_impulse_response/start_pulse_det
tx_pulse_width_upper	Average distance between upper threshold crossing times measured by start pulse detector.	seconds	ATL03/atlas_impulse_response/start_pulse_det
Delay_R	Range delay flag	unitless	ATL09
bckgrd_rate	The background count rate from the 50-shot altimetric histogram.	counts per second	ATL03/gtx/bckgrd_atlas/bckgrd_rate
bckgrd_delta_time	The beginning time interval for the bckgrd_rate estimation.	seconds	ATL03/gtx/bckgrd_atlas/delta_time
tlm_top_bandx	The ellipsoidal heights with respect to WGS-84 of the top of the telemetry bands, with all geophysical corrections applied.	meters	ATL03/gtx/bckgrd_atlas/tlm_top_bandx
tlm_height_bandx	The height in meters of the telemetry band. May be multi-valued if there is more than one telemetry band.	meters	ATL03/gtx/bckgrd_atlas/tlm_height_bandx

Name	Description	Units	ATL0x/Other Source
bckgrd_counts_reduced	Number of photon counts in the 50-shot sum after subtracting the number of signal photon events, defined as in section 5, and potential TEP photons in that span	counts	ATL03/gtx/bckgrd_atlas/
bckgrd_int_height_reduced	The height of the altimetric range window after subtracting the height span of the signal photon events in the 50-shot span	meters	ATL03/gtx/bckgrd_atlas/
full_sat_fract	The fraction of pulses within the segment determined to be fully saturated.	unitless	ATL03/gtx/geolocation/
near_sat_fract	The fraction of pulses within the segment determined to be nearly saturated.	unitless	ATL03/gtx/geolocation/
uncert_lat	Estimated geodetic Latitude uncertainty (1-sigma), for the reference photon.	degrees	ATL03/gtx/geolocation/sigma_lat
uncert_lon	Estimated geodetic Longitude uncertainty (1-sigma), for the reference photon.	degrees	ATL03/gtx/geolocation/sigma_lon
uncert_h	Estimated height uncertainty (1-sigma) for the reference photon.	meters	ATL03/gtx/geolocation/sigma_h
V_gt	Spacecraft Velocity vector array East component, North component, Up component. While values are common to all beams, this parameter is naturally produced as part of geolocation.	m/s	ATL03/gtx/geolocation/velocity_sc
time_ATL09	ATL09 output reporting time.	seconds	ATL09
MET_U10M	Eastward component of wind at 10m height.	m/s	ATL09
MET_V10M	Northward component of wind at 10m height.	m/s	ATL09

Name	**Description**	**Units**	**ATL0x/Other Source**
Snow_Ice	NOAA snow/ice flag scaled by ATL09 (0=ice-free water, 1=snow-free land, 2=snow, 3=ice)	unitless	ATL09
MET_TS	Surface (skin) temperature from ATL09	K	ATL09
T_atm	Atmospheric transmittance	unitless	ATL03 (standard met data)
gamma_app	Apparent water surface reflectance	unitless	ATL09
num_iw_bdy	Total number of inland water bodies	counts	ATL13 Inland Water Body Shape Mask
iw_bdy_region	ATL13-created shapefile representing relevant bodies of water over which to implement the ATL13 water surface finding algorithm only within a region of processing interest	shapefile	ATL13 regional Inland Water Body Shape Mask
iw_bdy_mask	ATL13-created shapefile representing relevant bodies of water over which to implement the ATL13 water surface finding algorithm	shapefile	ATL13 Inland Water Body Shape Mask
ATL13_reference_id	Unique aggregate reference number for each shape in the ATL13 Inland Water Body Mask, where digit 1 = type, digit 2 = size, digit 3 = source, and digits 4-10 = shape id	unitless	ATL13 Inland Water Body Shape Mask
iw_bdy_catalog	Array of inland water bodies ID, lat/long, etc	unitless	ATL13 Data File
iw_bdy_area	Area of each water body in the ATL13 Inland Water Body Shape Mask	meters^2	ATL13 Inland Water Body Shape Mask
iw_bdy_max_len	Longest axis of possible instrument transverse of water body shape	meters	ATL13 Inland Water Body Shape Mask

Name	Description	Units	ATL0x/Other Source
iw_bdy_type	Type of water body identified in ATL13 Inland Water Body Shape Mask (0=Lake, 1=River, 2=Wetland)	unitless	ATL13 Inland Water Body Shape Mask
cld_cover	Fractional clouds cover (unknown temporal/vertical/horizontal resolution)	unitless	ATL03/ATL09 (?)
atlas_azm	The direction, eastwards from north, of the laser beam vector as seen by an observer at the laser ground spot viewing toward the spacecraft (i.e., the vector from the ground to the spacecraft). When the spacecraft is precisely at the geodetic zenith, the value will be 99999 degrees. 40 Hz.	radians	ATL03/gtx/geolocation/ref_azimuth
atlas_zen	Co-elevation (CE) is direction from vertical of the laser beam as seen by an observer located at the laser ground spot.	radians	ATL03/gtx/geolocation/ref_elev
solar_azm	The direction, eastwards from north, of the sun vector as seen by an observer at the laser ground spot.	degrees_east	ATL03/gtx/geolocation/solar_azimuth
solar_zen	Solar Angle above or below the plane tangent to the ellipsoid surface at the laser spot. Positive values mean the sun is above the horizon, while negative values mean it is below the horizon. The effect of atmospheric refraction is not included. This is a low-precision value, with approximately TBD degree accuracy.	degrees	ATL03/gtx/geolocation/solar_elevation

Table 5-2 Parameters Needed to Drive the ATL13 Algorithm

Name	Var Type	Description	Default*
anmly_test	R*4	Array containing threshold values against which to test segments for heights that are anomalous to the rest of the water surface. The ***anmly_test*** value is selected based on the corresponding length of the water body crossing, calculated in the code as ***iw_bdy_xlen_flag***. The mode of each segment histogram will be tested against ***ht_water_coarse*** and marked as anomalous if the difference is greater than the anomaly test value associated with the segment's crossing length.	Body type 1,2,6,7 =[0.10,0.10,0.10,0.20,0.20,0.25,0.25,0.50,0.75,1.00,3.00,5.00] Body type 5 =[0.50,0.50,0.50,0.50,0.50,0.75,1.0,3.0,5.0,5.0,5.0,5.0]
atm_window1	R*4	Lower limit of height above coarse water surface height for atmospheric background count calculation.	100 meters
atm_window2	R*4	Upper limit of height above coarse water surface height for atmospheric background count calculation.	500 meters
b1_sseg1	R*4	Bin size to be used for histogramming of each small segment.	.05 meter
b2_sseg1	R*4	Bin size to be used for histogramming of small segment heights.	.05 meter
b_long	R*4	Bin size to be used by which to establish a histogram of long segments.	0.05
bckgrd_threshold	R*4	Thresholds outside of which computed background rate is flagged (High, Low).	[10^6,10^2] counts/sec
bin_detrend	R*4	Bin size used to establish a band of heights over which to determine the detrending equation.	0.05 meter
refr_idx_air	R*4	Refractive index, air (n_1).	1.00029
refr_idx_water	R*4	Refractive index, water (n_2) [seawater, freshwater]	[1.34116 , 1.33469]

c_fresnel	R*4	Fresnel specular reflection coefficient @ 532 nm	0.0209
detrend_width	R*4	Number of standard deviations +/- mode to include in detrend band.	1.25
f2_d_min	R*4	Minimum distance threshold between photons required for inclusion in algorithm.	0.05
gauss_pk_thres	R*4	Fraction of the peak amplitude above which Gaussian fit error analysis is executed (i.e., calculate error on Gaussian only between the peak amplitude and gauss_pk_thres * peak)	.20
geoseg_edge_buffer	I*2	Number of geosegments to include in the water surface calculation that are outside of both water body edges, as identified by reference photon location comparison to water body shapes	(1:9, 1): 5, 5, 5, 5, 5, 5, 5, 5, 5 (1:9, 2): 5, 5, 5, 5, 5, 5, 5, 5, 5 (1:9, 3): 5, 5, 5, 5, 5, 5, 5, 5, 5 (1:9, 4): 5, 5, 5, 5, 5, 5, 5, 5, 5 (1:9, 5): 5, 5, 5, 5, 5, 5, 5, 5, 5 (1:9, 6): 5, 5, 5, 5, 5, 5, 5, 5, 5 (1:9, 7): 5, 5, 5, 5, 5, 5, 5, 5, 5 (1:9, 8): 5, 5, 5, 5, 5, 5, 5, 5, 5 (1:9, 9): 5, 5, 5, 5, 5, 5, 5, 5, 5
h_mavg_a	I*2	Number of depth bins over which to compute H_mavg_a	3
h_mavg_b	I*2	Number of depth bins over which to compute H_mavg_b	11

h_mavg_c	I*4	Number of bins over which to calculate moving average	3
L_sub	I*4	Long segment size, operationally used as unit over which to characterize the subsurface, and deconvolve the instrument pulse and subsurface effects from the water surface response.	3000 photons
L_surf	I*4	Long segment size, operationally used as unit over which to detrend the water surface, characterize the surface, and deconvolve the instrument pulse and subsurface effects from the water surface response.	1000 photons
LSBR_threshold	R*4	Threshold at which the LSBR indicates a significant transition from signal photon richness to noise.	-1.0
m_avg_d	I*2	Number of depth bins over which to compute P_ht_long_subsurf_mavg	5
max_gseg_search	I*4	Maximum number of geosegments in either direction to search for reported water surface heights	25
ref_dist_iw_bdy	R*4	Maximum distance from a water body that a geosegment reference photon indicates the need for overlap testing each individual photon in the geosegment	100 meters
s_seg1	I*4	Short segment size, operationally used as unit over which to identify water surface height anomalies such as islands, bridges, etc.	100 photons
shore_buff_sseg_length	I*4	Maximum length of a short segment that can be marked as anomalous due to shore buffering.	30 meters
shore_buffer	I*4	Number of near-shore short segments to ignore in analysis due to near-shore influences.	(1:9, 1): 1, 1, 0, 0, 0, 1, 1, 0, 0 (1:9, 2): 1, 1, 0, 0, 0, 1, 1, 0, 0 (1:9, 3): 1, 1, 0, 0, 0, 1, 1, 0, 0 (1:9, 4): 1, 1, 0, 0, 0, 1, 1, 0, 0 (1:9, 5): 0, 0, 0, 0, 0, 1, 1, 0, 0

			(1:9, 6): 0, 0, 0, 0, 0, 1, 1, 0, 0 (1:9, 7): 0, 0, 0, 0, 0, 1, 1, 0, 0 (1:9, 8): 0, 0, 0, 0, 0, 1, 1, 0, 0 (1:9, 9): 0, 0, 0, 0, 0, 1, 1, 0, 0
sig_threshold	I*4	Minimum signal confidence required to be included in analysis	2
signal_window_bottom	R*4	Lower limit below coarse water surface to include photons for analysis.	50 meters
signal_window_top	R*4	Upper limit above coarse water surface to include photons for analysis.	50 meters
size_to_process	I*1	Water body sizes that are to be processed by the ATL13 algorithm for each water body type. This parameter is a rank 2 array of size 9x9, where array subscripts 1 through 9, coincide with body type digits along columns, and body size digits along rows. Array elements are binary values, if 0 then process body size for that type, 1 otherwise. Water body sizes are described in ATL13 chapter 4.7.1.2 and in Table 5-4.”	(1:9, 1): 0, 0, 0, 0, 0, 0, 1, 1, 1, (1:9, 2): 0, 0, 0, 0, 0, 0, 1, 1, 1, (1:9, 3): 1, 1, 1, 1, 1, 1, 1, 1, 1, (1:9, 4): 1, 1, 1, 1, 1, 1, 1, 1, 1, (1:9, 5): 1, 1, 1, 1, 1, 1, 1, 1, 0, (1:9, 6): 1, 1, 1, 1, 1, 1, 1, 1, 0, (1:9, 7): 1, 1, 1, 1, 1, 1, 1, 1, 0,

			(1:9, 8): 1, 1, 1, 1, 1, 1, 1, 1, 1, (1:9, 9): 1, 1, 1, 1, 1, 1, 1, 1, 1
sseg_length_test	R*4	Threshold by which to test the length of a short segment to determine anomalous or not anomalous, varying by water body type.	[500,500,500,500,500,500,500] meters
sseg_mode_cnt_test	I*4	Threshold to test number of values contained in short segment histogram multimodes against for inclusion or exclusion of short segment.	[10,10,7,7,7,7]
sseg_mode_freq_test	I*4	Threshold to test number of short segment histogram modes against for inclusion or exclusion of short segment.	3
sseg_mode_spread_test	R*4	Threshold to test distance between short segment histogram multimodes against for inclusion or exclusion of short segment.	50 cm
sub_max	R*4	Maximum vertical profile of water subsurface to include in estimation of subsurface characteristics	20 m
type_to_process	I*1	Water body types that are to be processed by the ATL13 algorithm. This parameter is a rank 1 array of extent 9, with the body type digits coinciding with the array subscripts 1 through 9. Array elements are binary values, if 0 then process body type, 1 otherwise. Water body types are described in ATL13 chapter 4.7.1.2 and in Table 5-4.	[0, 0, 1, 1, 0, 0, 0, 1, 1]
lidar_coeff_alpha_unit_min	R*6	Coefficient multiplier of unit exponential distribution and subsurface alpha_unit minimum values of iteration loops used in deconvolution, described in section 5.3.4 (A), based on water body type.	[5e-4, 0.02, 5e-4, 0.02, 5e-4, 0.02, 5e-4, 0.04, 5e-4, 0.04, 5e-4, 0.04, 5e-4, 0.02, 5e-4, 0.02, 5e-4, 0.02]

lidar_coeff_alpha_unit_max	R*6	Coefficient multiplier of unit exponential distribution and subsurface alpha_unit maximum values of iteration loops used in deconvolution, described in section 5.3.4 (A), based on water body type.	[0.015,3.0, 0.015, 3.0, 0.015, 1.2, 0.015, 5.0, 0.015, 5.0, 0.015, 3.0, 0.015, 3.0, 0.015, 1.2, 0.015, 1.2]
lidar_coeff_alpha_unit_incr	R*6	Iteration loop coefficient multiplier of unit exponential distribution and subsurface alpha_unit step increments used in deconvolution, described in section 5.3.4 (A), based on water body type.	[5e-5, 0.02, 5e-5, 0.02, 5e-5, 0.02, 5e-5, 0.02, 5e-5, 0.02, 5e-5, 0.02, 5e-5, 0.02, 5e-5, 0.02, 5e-5, 0.02]
lidar_coeff_alpha_unit_initial	R*6	Subsurface alpha_unit value of initial iteration estimate used in deconvolution, described in section 5.3.4 (A).	.01
alpha_unit_default	R*4	Default alpha value used to estimate subsurface contribution to surface deconvolution when one cannot be determined by subsurface deconvolution.	0.3
beta_unit_default	R*4	Default beta value used to estimate subsurface contribution to surface deconvolution when one cannot be determined by subsurface deconvolution.	0.0067
coarse_surface_top	R*4	Relative to coarse water height, top of coarse range of surface width for initial Gaussian fitting extent of observations.	5 meters
coarse_surface_bottom	R*4	Relative to coarse water height, bottom of coarse range of surface width for initial Gaussian fitting extent of observations.	-5 meters
coarse_detrended_width	R*4	Multiplier of sigma to establish width of Gaussian fit of detrended observations.	3
min_mirror_cnt	R*4	Minimum number of signal photons required in a fully-filled long or very segment (consisting of only full member short segments) in each step of mirroring approach to estimating observed surface mean and standard deviation.	(250, 200, 200, 600, 600)

min_mirror_multp	R*4	Multipliers of bin depth by which to lower the bottom of the vertical range used for identifying photons to mirror when necessary to meet the minimum count.	1, 2, 8

Table 5-3 Intermediate Variables

Name	Units	Description	Section
iw_bdy_overpass	counts	Number of transects over selected water body	5.3.1(B)
iw_bdy_grtrck	counts	Number of ground tracks over the selected water body for a given orbit_number	5.3.1(B)
iw_bdy_xlen	meters	Length of transect crossing of the identified inland water body (meters)	5.3.1 (B)
iw_bdy_xlen_flag	unitless	Flag characterizing the length of the crossing (1= iw_bdy_xlen<=1km, 2= 1km<iw_bdy_xlen<=10km, 3= 10km<iw_bdy_xlen<=100km, 4= iw_bdy_xlen>100km)	5.3.1 (B)
iw_bdy_area_flag	unitless	Flag characterizing the area of the crossing (1= iw_bdy_area<=50km^2, 2= iw_bdy_area>50km^2)	5.3.1 (B)
orbit_number	unitless	Calculated unique orbit identifier	5.3.1(B)
P_count	count	The number of photons in a given ground track	5.3.1(B)
P	N/A	Photon characteristics array of a single ground track.	5.3.1 (B)
shore_flag	unitless	Flag to indicate position of photon relative to water boundary (0 = water at a satisfactory buffer from shore, 1 = near-shore, within buffered length, 2 = land, 3 = in-water height anomalies)	5.3.1 (B)

Name	Units	Description	Section
iw_masked_NX	meters	First/last point locations along a track within water mask	5.3.1 (B)
iw_masked_EX	meters	First/last point locations along a track within water mask	5.3.1 (B)
GSeg	unitless	Array containing geosegment characteristics	5.3.1(B)
seg_ref_ph_lat seg_ref_ph_lon	degrees	The location of the reference photon of a given geosegment	5.3.1(B)
ref_count_iw_bdy	unitless	Number of water bodies within the threshold distance from given geosegment reference photon	5.3.1(B)
ref_id_iw_bdy	unitless	Identifying numbers of water bodies within the threshold distance from given geosegment reference photon	5.3.1(B)
crossed_id_iw_bdy	unitless	Identifying number of a water body actually intersected by a given photon	5.3.1(B)
P_geoseg	unitless	Geosegment to which a given photon belongs	5.3.1 (B)
P_geoid	meters	Geoid value assigned to a given photon.	5.3.1 (B)
P_atlas_azm	radians	Azimuth assigned to a given photon.	5.3.1 (B)
P_atlas_zen	radians	Zenith assigned to a given photon.	5.3.1 (B)
P_solar_azm	degrees_ east	Solar azimuth assigned to a given photon.	5.3.1 (B)
P_solar_zen	degrees	Solar zenith assigned to a given photon.	5.3.1 (B)
inland_water_body_ id	Unitless	ATL13 Inland Water Body ID; unique for each water body in the ATL13 Inland Water Body Mask	5.3.1 (C)
Inland_water_body_ type	unitless	Type of Inland Water Body, where 1=Lake, 2=Known Reservoir, 3=(Reserved for future use), 4=Ephemeral Water, 5=River, 6=Estuary or Bay, 7=Coastal Water, 8=Reserved, 9=Reserved	5.3.1 (C)

Name	Units	Description	Section
inland_water_body_size	unitless	Size of Inland Water Body, A=area, where 1=A>10,000 km^2, 2=10,000>A≥1,000, 3=1,000>A≥100, 4=100>A≥10, 5=10>A≥1, 6=1>A≥0.1, 7=0.01>A, 8=Reserved, 9=Not Assigned.	5.3.1 (C)
inland_water_body_source	unitless	Source of Inland Water Body shape, where: 1= HydroLAKES (Messager, M.L., Lehner, B., Grill, G., Nedeva, I., Schmitt, O. (2016): Estimating the volume and age of water stored in global lakes using a geo-statistical approach. Nature Communications: 13603. doi: 10.1038/ncomms13603. Data is available at www.hydrosheds.org.) 2= Global Lakes and Wetlands Database (Lehner, B. and Döll, P. (2004): Development and validation of a global database of lakes, reservoirs and wetlands. Journal of Hydrology 296/1-4: 1-22.) 3= Named Marine Water Bodies (ESRI http://mappingcenter.esri.com/index.cfm?fa=arcgisResources.gisData) 4=GSHHG Shoreline (Wessel, P., and W. H. F. Smith, A Global Self-consistent, Hierarchical, High-resolution Shoreline Database, *J. Geophys. Res., 101*, 8741-8743, 1996) 5= Global River Widths from Landsat (Allen and Pavelsky (2018) Global Extent of Rivers and Streams. *Science*. https://doi.org/10.1126/science.aat0636), 6=Reserved, 7=Reserved, 8=Reserved, 9=Reserved	5.3.1 (C)
P_delay_flag	unitless	Flag to indicate likelihood of severe range delay (0 = not likely, 1 = likely)	5.3.2 (B)
S_seg1_ID	counts	ID number of short segment	5.3.2 (C)
S_seg1_count	counts	Number of short segments	5.3.2 (C)
S_seg1_H	meters	Histogram array of short segment heights	5.3.2 (C)
S_seg1_modes	meters	Modes of arrayed histograms of short segments	5.3.2 (C)

Name	Units	Description	Section
sseg_stdev	meters	Standard deviation of signal photon heights per short segment	5.3.2(C)
sseg_stdev_thres	unitless	Threshold determined based on short segment signal photon height standard deviations, used to assign a short segment's sseg_mode_cnt_test value.	5.3.2(C)
sseg_multimode_mean	meters	Mean height of all the photons contained within multiple modes of short segment histogram.	5.3.2 (C)
ht_water_coarse	meters	Estimated coarse water surface height	5.3.2 (C)
n_1	R*4	Refractive index of air for a processed water body.	5.3.2 (C)
n_2	R*4	Refractive index of water for a processed water body.	5.3.2 (C)
c_adj	R*4	Adjustment for the speed of light through the water column, determined by n_1 / n_2 for each water body.	5.3.2 (C)
sseg_length	meters	Length of a short segment, measured from first (signal) photon in segment to last (signal) photon.	5.3.2 (D)
iw_seg_anom_flag	unitless	Flag characterizing an anomalous segment of a water body crossing (0=valid, 1=invalid/anomalous)	5.3.2 (D)
shore_buffer_start	unitless	Number of short segments at the beginning of water body transit to adjust from non-anomalous to anomalous.	5.3.2 (D)
shore_buffer_end	unitless	Number of short segments at the end of water body transit to adjust from non-anomalous to anomalous.	5.3.2 (D)
bckgrd_rate_avg	counts/sec	Average background rate over a small segment, as calculated from ATL03 rates	5.3.2 (E)
bckgrd_count_avg	counts	Average background count over a small segment	5.3.2 (E)

Name	Units	Description	Section
bckgrd_count_flag	unitless	A flag to indicate background is below a threshold (1) or not below a threshold (0) where threshold is bckgrd_threshold	5.3.2 (E)
bckgrd_dnsty_50sht	count	Background count in vertical profile	5.3.2 (E)
bckgrd_dnsty_50sht_bin	count	Background count in single bin	5.3.2 (E)
bckgrd_count_50sht_bin	count	Aggregate background count in a short segment histogram bin	5.3.2 (E)
L_surf_ID	unitless	Surface (long) segment to which a photon belongs.	5.3.3 (A)
L_surf_count	unitless	Number of surface (long) segments in a transect.	5.3.3 (A)
H_Lsurf_raw	meters	Photon height histograms of long segments	5.3.3 (A)
H_Lsurf_mode, H_Lsurf_stdev	meters	Calculated mode and standard deviation of surface (long) segments	5.3.3 (A)
H_long_mavg	meters	Smoothed histogram of long segments	5.3.3 (A)
surf_band_sigma	meters	Standard deviation of heights within near-surface band used to detrend	5.3.3 (A)
L_seg_count	counts	Number of long segments	5.3.3 (A)
L_seg_length	meters	Length of each long segment	5.3.3 (A)
L_seg_id	counts	Identifies to which long segment a signal photon belongs	5.3.3 (A)
H_Lsurf_ph_dens	meters	Array of surface (long) segment photon density histograms	5.3.3 (A)
H_mavg_a	meters	Array of smoothed photon density histograms based on ***H_mavg***_a steps	5.3.3 (A)
H_mavg_b	meters	Array of smoothed photon density histograms based on ***H_mavg_b*** steps	5.3.3 (A)
L_sub_ID	unitless	Subsurface (very long) segment to which a photon belongs.	5.3.3 (A)
L_sub_count	unitless	Number of subsurface (very long) segments in a transect.	5.3.3 (A)

Name	Units	Description	Section
H_Lsub_raw	unitless	Photon height histograms of subsurface (very long) segments	5.3.3 (A)
H_Lsub_mode H_Lsub_stdev	meters	Calculated mode and standard deviation of subsurface (very long) segments	5.3.3 (A)
H_Lsub_ph_dens	unitless	Array of subsurface (very long) segment photon density histograms	5.3.3 (A)
Bckgrd_count_atm_avg	counts	Array of the average atmospheric background for each long segment L_seg_ID	5.3.3 (B)
LSBR_up	unitless	Array of log of the surface to background rate toward the top of the wave	5.3.3 (B)
ph_density	m^{-2}	Photon density of long segment	5.3.3 (B)
ht_sbr_up	meters	Height at the first instance where the value of the LSBR moving from the mode toward the top of the wave meets a threshold for each long segment	5.3.3 (B)
LSBR_lo	unitless	Array of log of the surface to background rate toward the subsurface	5.3.3 (B)
ht_sbr_lo	meters	Height at the first instance where the value of the LSBR moving from the mode toward the subsurface for meets a threshold for each long segment	5.3.3 (B)
detrend_sigma	meters	Standard deviation of the Gaussian fit to the photon histogram for purposes of detrending	5.3.3 (C)
detrend_mean	meters	Mean height of the Gaussian fit to the photon histogram for purposes of detrending	5.3.3 (C)
detrend_amp	counts	Peak amplitude of the Gaussian fit to the photon histogram for purposes of detrending	5.3.3 (C)
H_detrend	meters	Histogram of detrended photon heights	5.3.3 (C)
Bckgrd_rate_atm	unitless	Normalized rate of background in atmosphere per designated bin size for each long segment.	5.3.3 (C)

Name	Units	Description	Section
detrend_band_flag	unitless	Flag indicating whether or not a given photon is within the elevation band being used to detrend (0 = not in band, 1= in band)	5.3.3 (C)
a_detrend,b_detrend	unitless	Coefficients (where y=ax+b) fit to detrending equation	5.3.3 (C)
Bckgrd_rate_subsurf	unitless	Normalized rate of background in subsurface per designated bin size for each long segment.	5.3.3 (C)
L_surf_ph_mirrored	meters	Long segment array of photons that includes all observed photons in the initial estimation of the surface domain as well as their mirrored counterparts.	5.3.3(C)
H_Lsurf_ph_mirrored_dens	counts	Histogram of long segment photons to be used in Gaussian fit of observed surface.	5.3.3(C)
mirror_threshold	photons	Array representing the minimum number, being min_mirror_cnt adjusted for actual length of long or very segment, of signal photons required to proceed in each step of mirroring approach to estimating observed surface mean and standard deviation.	5.3.3(C)
gauss_pk	unitless	Peak amplitude of photon histogram for purposing of detrending	5.3.3 (C)
P_ht_detrended	meters	Array of photons heights after removing trend.	5.3.3 (D)
h_detrend_surf	unitless	Histogram of detrended surface segment photon heights	5.3.3 (D)
h_detrend_subsurf	unitless	Histogram of detrended subsurface segment photon heights	5.3.3 (D)
h_detrend_surf_norm	unitless	Normalized histogram of detrended surface segment photon heights	5.3.3 (D)
h_detrend_subsurf_norm	unitless	Normalized histogram of detrended subsurface segment photon heights	5.3.3 (D)
gauss_pk2	counts	Peak amplitude of the normalized, detrended surface photon histogram	5.3.3 (D)

Name	Units	Description	Section
detrend_sigma2	meters	Standard deviation of the Gaussian fit to the normalized, detrended surface photon histogram	5.3.3 (D)
detrend_mean2	meters	Mean height of the Gaussian fit to the normalized, detrended surface photon histogram	5.3.3 (D)
detrend_amp2	counts	Peak amplitude of the Gaussian fit to the normalized, detrended surface photon histogram	5.3.3 (D)
gauss_pk2_Lsub	counts	Peak amplitude of the normalized, detrended subsurface photon histogram	5.3.3 (D)
detrend_sigma2_Lsub	meters	Standard deviation of the Gaussian fit to the normalized, detrended subsurface photon histogram	5.3.3 (D)
detrend_mean2_Lsub	meters	Mean height of the Gaussian fit to the normalized, detrended subsurface photon histogram	5.3.3 (D)
detrend_amp2_Lsub	counts	Peak amplitude of the Gaussian fit to the normalized, detrended subsurface photon histogram	5.3.3 (D)
W	unitless	Fraction of foam covered water surface	5.3.3 (D)
subsurface_h	meters	Height that marks a point at which all photon events below are solely subsurface returns and have no contribution to surface estimation	5.3.3 (D)
gamma_total	unitless	Total reflectance	5.3.3 (D)
γ^{wS}	unitless	Sun specular backscatter from wavy water surface back to receiver	5.3.3 (D)
gamma_surf	unitless	ATLAS specular backscatter from wavy water surface back to receiver	5.3.3 (D)
γ^{fS}	unitless	Sun lambertian backscatter from foam on water surface back to receiver	5.3.3 (D)

Name	Units	Description	Section
gamma_foam	unitless	ATLAS lambertian backscatter from foam on water surface back to receiver	5.3.3 (D)
γ^{uS}	unitless	Sun volume backscatter from the water column back to receiver	5.3.3 (D)
gamma_u	unitless	ATLAS volume backscatter from the water column back to receiver	5.3.3 (D)
γ^{bS}	unitless	Sun lambertian backscatter light from the bottom	5.3.3 (D)
γ^{bA}	unitless	ATLAS lambertian backscatter light from the bottom	5.3.3 (D)
R_SAS	unitless	Reflectance ratio	5.3.3 (D)
detrend_band_ph_mean	meters	Mean height of the detrended photons in the range over which the detrend line fitting was performed.	5.3.3(D)
Lsub_ph_mirrored	meters	Very long segment array of photons that includes all observed photons in the initial estimation of the surface domain as well as their mirrored counterparts.	5.3.3(D)
H_Lsub_ph_mirrored_dens	counts	Histogram of very long segment photons to be used in Gaussian fit of observed surface.	5.3.3(D)
inst_pulse	unitless	Instrument impulse response array	5.3.4 (A)
Subsurface_h	meters	Top height of subset of array of photons representing the subsurface.	5.3.4 (A)
subsurf_ph_mean	meters	Mean height of photons within the range of calculation of the subsurf_bottom value.	5.3.4 (A)
subsurf_ph_stdev	meters	Standard deviation of photons within the range of calculation of the subsurf_bottom value.	5.3.4 (A)
subsurf_ph_count	N/A	Number of qualified photons in the subsurface range used to estimate the subsurface bottom over which to deconvolve	5.3.4 (A)

Name	Units	Description	Section
subsurf_bottom	meters	Bottom height of the range over which to calculate the subsurface deconvolultion.	5.3.4 (A)
P_ht_long_subsurface	meters	Array of subsurface signal photons for each long segment.	5.3.4 (A)
P_ht_long_subsurf_mavg	meters	Smoothed array of subsurface signal photons for each long segment, smoothed by m_avg_d bins.	5.3.4 (A)
inst_pulse_norm	N/A	Normalized instrument impulse response array	5.3.4 (A)
alpha_unit	unitless	Decay coefficient of unit response shape	5.3.4 (A)
lidar_subsrf_bckscat_unit	unitless	Coefficient multiplier of unit exponential distribution.	5.3.4 (A)
alpha_obs	unitless	Decay coefficient of observation response shape	5.3.4 (A)
lidar_subsrf_bckscat_obs	unitless	Coefficient multiplier of observation exponential distribution.	5.3.4 (A)
alpha_model	unitless	Decay coefficient of modeled response shape	5.3.4 (A)
lidar_subsrf_bckscat_model	unitless	Coefficient multiplier of modeled exponential distribution.	5.3.4 (A)
alpha_unit_fit	unitless	Best fit unit response alpha value to minimize error between observations and model	5.3.4 (A)
lidar_subsrf_bckscat_unit_fit	unitless	Best fit unit response subsurface decay coeffecient multiplier value to minimize error between observations and model	5.3.4 (A)
beta_unit_fit	unitless	Best fit unit response beta (coeff divided by alpha) value to minimize error between observations and model	5.3.4 (A)
P_ht_long_surface	meters	Array of surface signal photons for each long segment.	5.3.4 (B)
sys_tot_resp_surface	unitless	Histogram of integrated response resulting from constrained deconvolution	5.3.4 (B)

Name	Units	Description	Section
HM_unit	meters	Mean wave height of response shape	5.3.4 (B)
sigma_unit	meters	Standard deviation of unit distribution.	5.3.4 (B)
HM_obs	meters	Mean wave height of observation response shape	5.3.4 (B)
sigma_obs	meters	Standard deviation of observation distribution.	5.3.4 (B)
HM_model	meters	Mean wave height of modeled response shape	5.3.4 (B)
sigma_model	meters	Standard deviation of modeled distribution.	5.3.4 (B)
HM_unit_fit	meters	Optimal unit response Mean wave height value to minimize error between observations and model	5.3.4 (B)
sigma_unit_fit	meters	Optimal unit response standard deviation to minimize error between observations and model	5.3.4 (B)
H_mode_fit	meters	The mode of the resulting best fit histogram model	5.3.4 (B)
H_unit_adj	meters	Delta height by which the apparent height of a short segment is adjusted to account for deconvolution analysis.	5.3.4 (B)
bottom_search_mean	meters	Average of photon heights that met criteria over which to execute search for water body subsurface anomalies and bottom	5.3.4 (A)
bottom_search_stdev	meters	Standard deviation of photon heights that met criteria over which to execute search for water body subsurface anomalies and bottom	5.3.4 (A)
bottom_search_ht	meters	Height(s) identified in long segments that mean criteria as possible water body bottom	5.3.4 (A)
sig_wv_ht	meters	Significant wave height	5.3.4 (C)
gauss_pk3	counts	Peak amplitude of the integrated system response histogram	5.3.4 (C)

Name	Units	Description	Section
detrend_sigma3	meters	Standard deviation of the Gaussian fit to integrated system response histogram	5.3.4 (C)
detrend_mean3	meters	Mean height of the Gaussian fit to the integrated system response histogram	5.3.4 (C)
detrend_amp3	counts	Peak amplitude of the Gaussian fit to the integrated system response histogram	5.3.4 (C)
sig_slope	unitless	Significant slope (slope at significant wave height)	5.3.4 (C)
obs_centroid_ht	meters	Centroid height of observation histogram, calculated over a specific range for use in fit bias estimation.	5.3.4 (C)
int_resp_centroid_ht	meters	Centroid height of integrated system response histogram, calculated over a specific range for use in fit bias estimation.	5.3.4 (C)
H_bias_fit	meters	Bias contribution from goodness of observation/system response fit	5.3.4 (C)
H_bias_EM	meters	Electromagnetic bias	5.3.4 (C)
spectral_peak	meters	Wavelength at the spectral peak	5.3.4 (C)
T_pk_atlas	seconds	The longest time between two sequential up-crossing surface signal photons within a long segment	5.3.4 (C)
T_pk	seconds	The longest time between two sequential up-crossing photons within a long segment	5.3.4 (C)
view_angle_norm	radians	Normalized satellite view angle	5.3.4 (C)
mean_sq_slope	m/m	Mean square slope of water surface	5.3.4 (C)
T_z_atlasmean_sq_ slope	seconds	The time interval between the first and the last signal photon within a long segment, divided by the minimum of the number of positive heights and the number of negative heights	5.3.4 (C)
T_z	seconds	Average zero up-crossing period	5.3.4 (C)

Name	Units	Description	Section
T_c_atlas	seconds	The time interval between the first and last signal photon within a long segment, divided by the total number of positive heights	5.3.4 (C)
T_c	seconds	Average crest period	5.3.4 (C)
M_zero	m^2	Water surface spectral moment	5.3.4 (C)
M_two	m^2/s^2	Water surface spectral moment	5.3.4 (C)
M_four	m^2/s^4	Water surface spectral moment	5.3.4 (C)
spec_width	unitless	Spectral width parameter	5.3.4 (C)
u_10	meters/sec	Wind speed calculated 10 meters above the surface	5.3.4 (D)
ξ	unitless	Standardized slope component	5.3.4 (D)
η	unitless	Standardized slope component	5.3.4 (D)
σ_{up}	unitless	Upwind mean standard deviation of slopes	5.3.4 (D)
σ_{cr}	unitless	Crosswind mean standard deviation of slopes	5.3.4 (D)
c_n	unitless	Expansion term coefficients for Gram-Charlier distribution [c_{21}, c_{03}, c_{40}, c_{04}, c_{22}]	5.3.4 (D)
σ_c,σ_u	unitless	RMS slopes contributing to Gram-Charlier distribution	5.3.4 (D)
$Surf\_Resp_M$	Meters	Modeled fit of total surface response including instrument pulse	5.3.4 (D)
z	Meters	Depth below mean surface	5.3.5 (A)
γ_uA (0)	unitless	Computed surface backscatter	5.3.5 (A)
K_A	unitless	ATLAS Subsurface attenuation coefficient	5.3.5 (A)
P_h _short_surface	photons	Isolated surface response of water to ATLAS pulse in short segment lengths	5.3.5 (A)
Segment_slope_trk_body	unitless	Slope of each of the surface (long) segments of the water body.	5.3.5 (A)

Name	Units	Description	Section
sseg_mean_lat	degrees	Mean latitude of all the photons in a short segment that meet the signal and height criteria for inclusion in the calculation	5.3.5 (A)
sseg_mean_lon	degrees	Mean longitude of all the photons in a short segment that meet the signal and height criteria for inclusion in the calculation	5.3.5 (A)
sseg_mean_ht	meters	Mean height of all the photons in a short segment that meet the signal and height criteria for inclusion in the calculation	5.3.5 (A)
sseg_mean_time	seconds	Mean time of all the photons in a short segment that meet the signal and height criteria for inclusion in the calculation	5.3.5 (A)
MET_U10M	m/s	ATL09 input	5.3.5 (A)
MET_U10M	m/s	ATL09 input	5.3.5 (A)
Snow_ice_ATL09	K	Based on ATL09 input	5.3.5 (A)
MET_TS_ATL09	unitless	Based on ATL09 input	5.3.5 (A)
u_derived	m/s	ATLAS derived wind speed	5.3.5 (B)
Output_shore_ flag	unitless	Possible bottom or vegetation reflectance due to proximity to shoreline 0 ≤ 100 m, 2>100m	5.3.5 (B)
vertXX_lat, vertXX_lon	latitude, longitude	The coordinates of planar verticies identified during the course of multibeam product calculation	5.3.5(B)
sseg_mean_atlas_azm	radians	Mean atlas azimuth for a given short segment based on photons satisfying signal threshold (index photon-fix this)	5.3.5 (C)
sseg_mean_atlas_zen	radians	Mean atlas zenith for a given short segment based on photons satisfying signal threshold	5.3.5 (C)
sseg_mean_solar_azm	degrees_ east	Mean solar azimuth for a given short segment based on photons satisfying signal threshold (????)	5.3.5 (C)
sseg_mean_solar_zen	degrees	Mean solar zenith for a given short segment based on photons satisfying signal threshold	5.3.5 (C)

Name	Units	Description	Section
QF_bias_fit	unitless	Flag related to goodness of fit bias	5.3.5 (C)
QF_bias_EM	unitless	Flag related to electromagnetic bias	5.3.5 (C)
QF_bias_Spec_Width	unitless	Flag related to spectral width	5.3.5 (C)

5.3 Processing Procedure for Parameters

5.3.1 Extract data and select next inland water body

The overall procedure is to process global inland water bodies for each ATL03 processing period. For each period, the ATL13 algorithm loops through the full suite of global regional basins. All water bodies within a given regional basin (a subset of the inland water body catalog from i=1 to ***num_iw_bdy***) intersected by new ATLAS transects within that processing period are fully analyzed before proceeding to the next regional basin. After all the water bodies in a given regional basin are analyzed, the algorithm moves to the next regional basin.

A) Start/ Identify Regional Basin
Each ATL13 water body to be analyzed is identified in a subsetted catalog, ***iw_bdy_catalog***, First, a geographic subset of the original ATL13 inland water body shape mask lakes is obtained based on the ATL13 Regional Basin Mask, where ***iw_bdy_region(region)*** is a static shapefile lake mask subset that will provided for use in ATL13. These lakes may then be filtered by some criteria to produce the processing ***iw_bdy_catalog***. The purpose of ***iw_bdy_catalog*** is to provide some measure of flexibility in which water bodies are analyzed, for instance very small lakes, misclassified lakes and wetlands, or ephemeral lakes. The constraints on ***iw_bdy_catalog*** will be determined based on experience gained on the performance of ATLAS during calibration and validation.

B) Extract and array all photons for all (n) ground tracks. Extract auxiliary data.

All requisite ATLAS and auxiliary data (identified in Table 5-1) associated with transects in the regional basin to be processed are to be extracted. This includes ATL03 parameters and data products including: photons, range products, geosegment characteristics, background noise, identification of signal photons, quality flags. Auxiliary data includes meteorologic (E.g. 10m wind and speed, direction) and hydrologic data (E.g. reservoir gauge heights), and ATL09 cloud products for those tracks.

The algorithm begins by identifying the intersections of any water bodies in ***iw_bdy_catalog*** with ground tracks during the processing period. The identification numbers of unique cycles that have crossed water bodies in the catalog are stored in array ***cycle,*** and ***grtrck*** will identify each of up to 6 ground track water body crossings for a given orbit overpass, where ***orbit_number(n) = (cycle(n) – 1) * 1387 + rgt(n)***. The algorithm is executed per water body as a nested loop where every individual ground track ***orbit_number(1:grtrck***) is processed per unique ***orbit_number***.

Analysis of each individual ground track occurs within a loop of orbits that exist over the given water body ***iw_bdy_id***. For each overpass of the water body (1:***cycle)***, the algorithm is applied to each individual ground track (***1:grtrck)*** that crosses ***iw_bdy_id*** during the processing period.

In order to determine which photons intersect with a water body, it is necessary to process the data associated with each ground track. Over a loop of all transects stored in ***cycle***, all photons and their characteristics for an individual ground track ***orbit_number(grtrck)*** are stored as array ***P = {P_time, P_lat, P_lon, P_ht, P_sig_flag}.*** Note that ***P_time*** = ***P_time_start*** + ***Elap_time***.

Geosegment-rate information is also extracted for each groundtrack ***grtrck*** as the loop is executed. A geosegment characteristic array is created for each groundtrack as ***GSeg*** = {***segment_id***, ***segment_ph_cnt***, ***surf_type, seg_ref_ph_lat, seg_ref_ph_lon, geoid, atlas_azm, atlas_zen, solar_azm, solar_zen}***. This array is tagged with the groundtrack and orbit identifiers being processed in each step in the loop. Based on the ***segment_id*** and the ***segment_ph_cnt*** stored in the geosegment array, a segment id, geoid value, and angle inputs are then assigned to each photon in array ***P*** as ***P_geoseg, P_geoid, P_atlas_azm, P_atlas_zen, P_solar_azm, and P_solar_zen***.

For each photon, assign a geoid-adjusted height ***P_ht_g = P_ht – P_geoid.***

<u>C) Identify next water body in catalog. Define intersection of ATL13 Inland Water Body Shape Mask and ATL03 Inland Water Mask.</u>

All six individual ground tracks of a given ATLAS transect must be included in the water body intersection analysis, as it is possible that the center reference track misses the water body, even though some number of neighboring beams actually observe the water body.

For each ground track ***RGT(grtrck),*** the geosegment reference photon location is used in order to determine if the geosegment is near enough to a water body to merit inclusion in the water surface height calculation. The reference photon location (***seg_ref_ph_lat, seg_ref_ph_lon***) is compared to the water bodies in ***iw_bdy_region(region),*** only in regions to be processed as identified by ***regions_to_process,*** and if the photon is within ***ref_dist_iw_bdy*** of a shape in the

ATL13 Inland Water Body Mask, the number of shapes ***ref_count_iw_bdy*** as well as the identifiers of those shapes ***ref_id_iw_bdy*** are added to the ***GSeg*** array for each ***segment_id***. If no lake is located within ***ref_dist_iw_bdy*** of the geosegment reference photon, ***ref_count_iw_bdy*** and ***ref_id_iw_bdy*** equal zero.

The first time that a given water body ***iw_bdy_region(region)*** is found to include a geosegment for analysis, obtain the ***ATL13_reference_ID*** from the ATL13 Inland Water Body Mask and determine ***inland_water_body_id***, ***inland_water_body_type***, ***inland_water_body_size***, ***inland_water_body_shape*** where ***ATL13_reference_ID*** is an aggregate of the following components:

digit 1 = ***inland_water_body_type***
digit 2 = ***inland_water_body_size***
digit 3 = ***inland_water_body_source***
digits 4 through 10 = ***inland_water_body_id*** (a 7-digit number)

Before proceeding, if ***inland_water_body_size*** = 0, reassign as ***inland_water_body_size*** = 9.

Test the water body against ***type_to_process***, ***size_to_process*** to determine whether or not to process the water body. If ***inland_water_body_type*** attribute obtained from ***ATL13_reference_ID*** is included in the ***type_to_process*** array, processing of that water body is required if ***size_to_process*** is included as any element in ***inland_water_body_size***(***inland_water_body_type***). Otherwise processing is not required.

For each transect, ***geoseg_edge_buffer is selected based on the type and size of the water body as geoseg_edge_buffer(inland_water_body_size, inland_water_body_type)*** If processing is required, mark the preceding ***geoseg_edge_buffer*** geosegments in the GSeg array with ***ref_count_iw_bdy*** and ***ref_id_iw_bdy*** to indication inclusion in the height calculation algorithm. Likewise, make the same adjustment to the first ***geoseg_edge_buffer*** geosegments encountered after determining that the water body has been exited. These provide a buffer of extra surface near both lake edges of the crossing for inclusion the height calculations.

Using the ATL13 Inland Water Body Shape Mask, identify the first and last points within the mask for each track as ***iw_masked_E1(iw_bdy_grtrck), iw_masked_N1(iw_bdy_grtrck), iw_masked_E2(iw_bdy_grtrck), iw_masked_N2(iw_bdy_grtrck)***. These are equivalent to the first photon of the first geosegment marked for water body analysis and the last photon of the last geosegment marked for analysis exiting the crossing. By definition, these will exist in the buffer space created by the addition of ***geoseg_edge_buffer*** geosegments on each edge crossing. The crossing length is ***iw_bdy_xlen*** is computed as a geospatial database calculation based on the location of the first and last points of each crossing of a water body. Based on the length of the crossing, look up the corresponding value for ***iw_bdy_xlen_flag*** to characterize the length of the crossing as:

1= ***iw_bdy_xlen***<=*50m*, 2= *50m*<***iw_bdy_xlen***<=*100m*, 3= *100m*<***iw_bdy_xlen***<=*200m*, 4= *200m*<***iw_bdy_xlen***<=*500m*, 5= *500m*<***iw_bdy_xlen***<=*1km*, 6= *1km*<***iw_bdy_xlen***<=*2km*, 7= *2km*<***iw_bdy_xlen***<=*5lm*, 8= *5km*<***iw_bdy_xlen***<=*10km*, 9= *10km*<***iw_bdy_xlen***<=*20km*, 10= *20km*<***iw_bdy_xlen***<=*50km*, 11= *50km*<***iw_bdy_xlen***<=*100km*, 12= ***iw_bdy_xlen***>*100km*

For clarity of output reporting, ***inland_water_body_id*** = ***crossed_id_iw_bdy***. With regard to the definition of a granule, one option is that data from any of the potential six ground tracks from a single ATLAS transect that cross a given inland water body are stored within a single granule. Additional ATLAS crossings of that same water body are stored in a separate granule, identified by orbit number, date, time, etc. (TBD – will work w/SIPS on this).

Resampling / Alignment of IRF

Extract the TEP characteristics for the region of the water body, selecting the spot recommened by ATL03, resampling to ***TEP_bin_size*** bin width, then arrayed as ***irf_time*** and ***irf_cnts***. Calculate the approximate standard deviation of the Gaussian portion of the resampled TEP histogram by fitting a Gaussian to the histogram and minimizing the error of fit over the range only where the amplitude of the Gaussian is between its peak, ***irf_gauss_pk*** and an amplitude equal to ***irf_gauss_pk_thres * irf_gauss_pk***. Once the error minimization has determined the best fit, the characteristics of the fit are recorded as ***irf_mean***, ***irf_sigma***, and ***irf_amp***. Calculate a second Gaussian fit, minimizing the error of fit over the range only where the amplitude of the Gaussian is between its peak, ***irf_gauss_pk*** and an amplitude equal to ***irf_gauss_pk_thres2 * irf_gauss_pk,*** in order to determine ***irf_mean2, irf_sigma2, and irf_amp2*** of the resampled TEP histogram**.**

Calculate the sum of the counts between ***irf_mean*** + ***irf_norm_range_up * irf_sigma*** and ***irf_mean – irf_norm_range_down *irf_sigma*** in ***array irf_cnts*** as ***irf_cnts_total***. Divide each bin in ***irf_cnts*** by ***irf_cnts_total*** to create array ***irf_cnts_norm***.

Determine desired beginning of IRF as ***IRF_start*** = ***irf_mean*** + ***irf_start_top*** * ***irf_sigma,*** and trim all IRF ***irf_time*** and ***irf_cnts_norm*** that preceeds ***irf_time*** = ***IRF_start,*** with the results defined as ***IRF_time_final*** and ***IRF_cnts_norm_final.***

Set ***inst_pulse_norm = IRF_cnts_norm_final.***

TEP_bin_size = 5 (cm)
irf_gauss_pk_thres = 0.2
irf_gauss_pk_thres2 = 0.5
irf_norm_range_up = 3
irf_norm_range_down = 8
irf_start_top = 3

5.3.2 Determine inland water segments viable for analysis for each ground track

A) Select next ground track
Sections 5.3.2 through 5.3.4 loop through analysis for single ground tracks (***1***:***iw_bdy_grtrck)*** determined to be within the water body identified in 5.3.1(A).

B) *[space reserved for future development]*

C) Histogram short segments of signal photons and establish coarse apparent water surface height.

For each ground track, ***P_ht_g (***only when ***P_sig_flag*** is equal to or greater than ***sig_threshold)*** is to be histogrammed (bin size = ***b1_sseg1***) in segments containing ***S_seg1(iw_body_type)*** signal photons over the telemetry window ***tlm_top_bandx*** to ***tlm_top_bandx – tlm_height_bandx***, resulting in ***S_seg1_count*** individual segments where ***S_seg1_ID(1:S_seg1_count)*** identifies the segment to which each photon is assigned. This assignment is based on transects uninterrupted by any exit from the ATL13 Inland Water Body Mask, and any such exit shall result in beginning a new analysis on the remainder of the water body, or until it is exited again. For each short segment constructed as follows, note the ***transect_ID*** which steps by one with each interruption to the crossing of the mask. In the case of a transect across a water body that begins and ends without exiting the mask, ***transect_ID***=1 for each short segment in the transect.

Based on the number of photons to be assigned to each segment (***S_Seg1(iw_body_type)***), sequentially loop through the photon array ***P(1:P_count)*** and assign a short segment ID number ***S_seg1_ID(1:S_seg1_count)*** to each photon as a new attribute column the working array ***P***. For each photon, if ***P_sig_flag*** is less than ***sig_threshold***, the (non-zero) ***S_seg1_ID*** is still assigned, but it does not count toward the ***S_Seg1(iw_body_type)*** photons necessary to complete the segment.
For additional photons that remain after construction of the regular short segments, aggregate the remaining leftover photons into an additional short segment if:

- The final full short segment preceding the remaining signal photons is non-anomalous
- The ***leftover_ph_count*** >= (***leftover_min_perc***)*s_seg1, where ***leftover_ph_cnt*** = the number of signal photons remaining beyond full short segment construction and ***leftover_min_perc*** = 0.10.

Once the final signal photon in the partial short segment has been identified, trim all photons that occur after that signal photon so that the partial short segment ends with its final signal photon. *Geosegment-based outputs (i.e., saturation fraction, POD/PPD flag, etc.) are calculated based on only the portion of geosegment(s) that overlaps the partial short segment.*

After finalizing the short segment, calculate the mean of the signal photons as ***leftover_sseg_mean_ht*** and set ***QF_IWP*** = 0. If abs(***leftover_sseg_mean_ht*** – ***ht_water_coarse***) > ***anmly_test***, mark the short segment as anomalous.

Write the all typical output to anom_ssegs group for the partial short segment with the following modifications:
anom_sseg_mode = Invalid (no histogram available)
anom_sseg_stdev = Standard deviation of the signal photons in the partial segment.
anom_sseg_sig_ph_cnt = NEW = Count of signal photons in short segment, full or partial.

If partial segment is non-anomalous, proceed with processing output written as follows for partial short segments to non-anomalous output group.

For all short segments, be they full or parital, non-anomalous or anomalous, write the signal photon count in the short segment to the appropriate output location as ***sseg_sig_ph_cnt***.

Based on the geosegment information assignment from ATL03, use ***ph_index_beg*** and ***segment_ph_cnt*** to determine to which geosegment the photon belongs and assign a value equal to ***segment_id*** as a new attribute column in array ***P***. Based on the locations of the first and last photons in each small segment, calculate its length as ***sseg_length(1:S_seg1_count).*** Estimate the standard deviation of the height of each short segment as ***sseg_stdev(S_seg1_ID)*** = standard devation (signal photon heights(1:***S_Seg1(iw_body_type)***)), including the heights of all photons in the segment of ***P_sig_flag*** >= ***sig_threshold***. Note the start and end locations of each short segment as ***sseg_start_lat***, ***sseg_start_lon***, ***sseg_end_lat***, and ***sseg_end_lon***, where the photon used to define each may be signal or non-signal.

Based on the standard deviation, assign the value of ***sseg_stdev_thres*** as:
If 0 < ***sseg_stdev(S_seg1_ID)*** <= 0.25, ***sseg_stdev_thres*** = ***1***
If 0.25 < ***sseg_stdev(S_seg1_ID)*** <= 0.50, ***sseg_stdev_thres*** = ***2***
If 0.50 < ***sseg_stdev(S_seg1_ID)*** <= 0.75, ***sseg_stdev_thres*** = ***3***
If 0.75 < ***sseg_stdev(S_seg1_ID)*** <= 1.0, ***sseg_stdev_thr***es = ***4***
If 1.0 < ***sseg_stdev(S_seg1_ID)*** <= 1.5, ***sseg_stdev_thres*** = ***5***
If 1.5 < ***sseg_stdev(S_seg1_ID)***, ***sseg_stdev_thres*** = ***6***

Array the histograms of each small segment ***S_seg1_ID(1:S_seg1_count)*** in ***S_seg1_H(1:S_seg1_count)*** and calculate the modes as ***S_seg1_modes(1:S_seg1_count)***.

For all short segments, the initial status of ***anom_sseg_trigger_flag(S_seg1_ID)*** should be set to invalid. Once the short segment undergoes any of the anomaly tests described below, its value of ***anom_sseg_trigger_flag(S_seg1_ID)*** corresponding the element index of the given test performed as described in Table 5-4b shall be set to either "0" (non-anomalous) or "1" (anomalous).

If a short segment histogram has more than one mode, take the following steps to find a single ***S_seg1_modes*** solution for that segment:

1) If there are more than ***sseg_mode_freq_test*** modes in a short segment ***S_seg1_ID***, mark the short segment as anomalous by setting ***anom_flag(S_seg1_ID)*** = 1 for the short segment.
2) If the count of photons in the bins found to be modes is less than ***sseg_mode_cnt_test(sseg_stdev_thres)***, mark the short segment as anomalous by setting ***anom_flag(S_seg1_ID)*** = 1 for the short segment.
3) If the height difference between the upper-most occurring mode and the lower-most occurring is greater than ***sseg_mode_spread_test***, mark the short segment as anomalous by setting ***anom_flag(S_seg1_ID)*** = 1 for the short segment.
4) If the count of photons in the bin found to be mode of the short segment is less than ***sseg_mode_cnt_test(sseg_stdev_thres)***, mark the short segment as anomalous by setting ***anom_flag(S_seg1_ID)*** = 1 for the short segment.
5) If none of the exclusionary tests above apply, calculate a single mode by first finding the mean of all the signal photons (where ***P_sig_flag*** is equal to or greater than ***sig_threshold)*** that exist within the bins indicated as multi-mode solutions, ***sseg_multimode_mean***. After calculating ***sseg_multimode_mean***, designate the bin that

the mean value falls within as the single-mode solution ***S_seg1_modes*** for the short segment.

Test for anomalous short segments due to abnormally long segment length where the length of the segment exceeds ***sseg_length_test(inland_water_body_type***). If the length of a short segment, ***sseg_length***, as calculated by the distance from the reference photon in the geosegment of first (may be signal or non-signal) photon to the reference photon of the geosegment that includes the last photon (may be signal or non-signal) of the short segment, is greater than ***sseg_length_test(inland_water_body_type)***, mark the short segment as anomalous by setting ***anom_flag(S_seg1_ID)*** = 1 for the short segment.

The coarse apparent height of the water surface is estimated by histogramming (bin size ***b2_sseg1***) ***S_seg1_modes(1:S_seg1_count)*** and identifying the mode of that histogram as ***ht_water_coarse***. In the event of a multi-mode occurrence at this step, average the modes to produce ***ht_water_coarse*** and set ***ht_water_coarse_flag*** equal to the difference between the highest and lowest mode (measured in number of bins).

For the water body being processed,
n_1 = ***refr_idx_air***
n_2 = ***refr_idx_water***(1) when ***inland_water_body type*** = {6,7}
n_2 = ***refr_idx_water***(2) when ***inland_water_body type*** = {1,2,5}
c_adj = n_1/n_2

D) Test for height anomalies (including shore) within the ground track

This algorithm tests for along-track height anomalies due to land or other man-made structures. Water heights are not expected to change substantially between short segments. Changes from surface type also will exhibit potential change in surface reflectance. Analysis will thus examine a combination of relative (***S_seg1(iw_body_type)*** photon count) segment height analysis, signal-to-noise ratio, and apparent reflectance, to determine if a non-water anomaly has occurred. If so, this portion of ground track will be skipped.

Within the working array ***P,*** non-water contribution to height measurement such as shore, islands, bridges, etc. need to be removed from consideration by assigning and appropriate ***anom_flag*** values to short segments. These anomalous contributions will be identified using the histograms in ***S_seg1_H(1:S_seg1_count)***, with the set of parameters to be used based on the length of transect flag, ***iw_bdy_xlen_flag***.

If the absolute value of the difference between ***S_seg1_modes(S_seg1_ID)*** and that of ***ht_water_coarse*** is greater than ***anmly_test(iw_bdy_xlen_flag)***, an individual short segment ***S_seg1_ID(1:S_seg1_count)*** is identified as an anomalous segment, and ***anom_flag(S_seg1_ID)*** = 1 for the short segment.

Test the water body to determine if as many as ***shore_buffer*** non-anomalous short segment(s) at either edge of the body are to be designated as anomalous, where ***shore_buffer_start*** is the number of heretofore non-anomalous short segments nearest the start of the transect to mark as anomalous and ***shore_buffer_end*** is the number to mark as anomalous nearest the end of the transect. As part of this calculation, an accounting of short segments that have passed all anomaly testing so far is performed where ***valid_sseg_count*** = the count of short segments where ***anom_flag*** = 0. Determine ***shore_buffer_start*** and ***shore_buffer_end*** through the following process:

If ***water_body_type*** = 1 or 2 (lake or reservoir), and ***water_body_size*** <= 4, and ***valid_sseg_count*** >= (***L_sub*** / ***S_seg1(iw_body_type)***) + 2 * ***shore_buffer***:

> Set ***shore_buffer_start*** = the count of first ***shore_buffer*** non-anomalous short segment(s) inside the water body with ***sseg_length*** < ***shore_buffer_sseg_length*** meters inside the water body from the transect beginning. Set ***anom_flag*** = 1 for ***shore_buffer_start*** short segments inside the transect. (note if shore_buffer_start = 0, no adjustment is made to existing short segments where ***anom_flag =*** 0)
>
> Set ***shore_buffer_end*** = the count of last ***shore_buffer*** non-anomalous short segment(s) inside the water body with ***sseg_length*** < ***shore_buffer_sseg_length*** meters at end of the transect toward end of the water body. Set ***anom_flag*** = 1 for ***shore_buffer_end*** short segments at water body exit.
>
> Bodies of type 1 and 2 and their included short segments that do not satisfy all of the above criteria will not be subject to ***anom_flag*** adjustment due to shore buffering.

If ***water_body_type*** = 4 (ephemeral) or 5 (river), ***shore_buffer_start*** = ***shore_buffer_end*** = 0 (zero).

> No adjustment due to shore buffering is made to the ***anom_flag*** array in this case.

If ***water_body_type*** = 6 or 7 (est/bay, coastal), and ***valid_sseg_count*** >= (***L_sub*** / ***S_seg1(iw_body_type)***) + 2 * ***shore_buffer***:

> Set ***shore_buffer_start*** = the count of first ***shore_buffer*** non-anomalous short segment(s) inside the water body with ***sseg_length*** < ***shore_buffer_sseg_length*** meters inside the water body from the transect beginning. Set ***anom_flag*** = 1 for ***shore_buffer_start*** short segments inside the transect.
>
> Set ***shore_buffer_end*** = the count of last ***shore_buffer*** non-anomalous short segment(s) inside the water body with ***sseg_length*** < ***shore_buffer_sseg_length*** meters at end of the transect toward end of the water body. Set ***anom_flag*** = 1 for ***shore_buffer_end*** short segments at water body exit.

Bodies of type 6 and 7 and their included short segments that do not satisfy all of the above criteria will not be subject to ***anom_flag*** adjustment due to shore buffering.

E) Compute background count and saturation fraction per short segment.

Short segment rate background calculation:

Convert background input data to a 50-shot background density by creating array ***bckgrd_dnsty_50sht*** where each element is equal to ***bckgrd_counts_reduced / bckgrd_int_height_reduced***.

The background density array per 50 shots over each histogram bin is therefore calculated as ***bckgrd_dnsty_50sht_bin*** = ***bckgrd_dnsty_50sht * b1_sseg1***.

For each short segment ***S_seg1_ID(1:S_seg1_count)***, estimate the background count by first identifying all occurrences of 50-shot ***bckgrd_dnsty_50sht_bin***overlap within that short segment and then calculating the total of those occurrences as ***bckgrd_count_50sht_bin (S_seg1_ID).*** To accomplish this, loop through each short segment ***S_seg1_ID***, and at each iteration then loop through all of the 50-shot ***bckgrd_dnsty_50sht_bin (1:n)*** values**.** Based on the start and end time of each short segment and each 50-shot background count calculation, determine if ***bckgrd_dnsty_50sht_bin (i)*** is relevant to the short segment. The beginning and end of each short segment should be considered ***P_time*** of the first and final signal photons, which defined the length of that short segment. The beginning and end of each bckgrd count estimation is defined by ***bckgrd_delta_time(i)*** and ***bckgrd_delta_time(i)***+.005.

If the ***bckgrd_dnsty_50sht_bin (i)*** tabulation does not overlap the short segment (in time) at all, ignore, and iterate to the next value, ***bckgrd_dnsty_50sht_bin (i+1)***.

If ***bckgrd_dnsty_50sht_bin (i)*** partially overlaps the short segment, calculate the percent of the short segment which is overlapped as ***sseg_overlap(i)***. If ***bckgrd_dnsty_50sht_bin (i)*** is fully contained within a short segment, set ***sseg_overlap(i)*** = 1. Once all bckgrd counts have been looped through, calculate the total ***bckgrd_ count_50sht_bin (S_seg1_ID)*** as:

bckgrd_ count_50sht_bin (S_seg1_ID) = ∑(bckgrd_dnsty_50sht_bin *sseg_overlap)$_{1\text{-}n}$

Note: If a ***bckgrd_dnsty_50sht_bin (i)*** begins before a ***S_seg1_ID*** and ends after that short segment, set ***bckgrd_count_50sht_bin (S_seg1ID)*** = ***bckgrd_dnsty_50sht_bin (i),*** with no averaging necessary.

Short segment rate saturation fraction calculation:

In order to estimate the full and near saturation fractions for each short segment ***segment_full_sat_fract(i)*** and ***segment_near_sat_fract(i)***, calculate the weighted average of the saturations of ***N_geoseg*** geosegments that overlap the short segment based on the total count of shots that overlap, ***N_pulses***.

Based on that number of unique pulses that overlap a short segment (***N_pulses***), calculate the weighted average of their contribution to the short segment saturation based on the saturation characteristics of the geosegment(***j***=1,***N_geoseg***) to which the sseg-overlapping pulses of that geosegment belong as:

segment_full_sat_fract(i) = Σ [***pulse_cnt***(j)****full_sat_fract***(j)] / ***N_pulses,***

where ***pulse_cnt***(j) = number of pulses in geosegment(j) which overlap the short segment and ***full_sat_fract*** is ATL03 input.

Similarly, estimate the near saturation fraction of the short segment as:

segment_near_sat_fract(i) = Σ [***pulse_cnt***(j)****near_sat_fract***(j)] / *N_pulses*

F) Short / Very Short Transect Contingencies

See description in Section 4.7.1.2.

The number of signal photons in a long segment, ***L_surf***, is equal to ***S_seg1(iw_body_type) * L_surf_muitlplier***. If ***short seg count*** < ***[L_surf / S_seg1(iw_body_type)]*** (ie, 1000/1000 = 10), use values for ***alpha_unit_fit*** and ***beta_unit_fit*** equal to those of the preceeding long segment. If no preceeding long segment exists, ***alpha_unit_fit*** = ***beta_unit_fit*** = invalid.

The following steps should also be taken in the case of short segments at the far end of the lake that are not assigned to a long (surface) segment, and their adjusted heights reported in the same way as outlined in this module.

min_sseg_threshold_short = 5
alpha_unit_default_short = 0.5
beta_unit_default_short = 0.02

For short transects where ***short seg count*** > ***min_sseg_threshold,*** the following procedure outlines the contingency approach.

Histogram the short segments as ***H_Lsurf_incomplete***, and fit an 80% height gaussian to establish ***L_surf_inc_mean*** and ***L_surf_inc_stdev***.

Detrend as would be done with complete long segment and histogram results to determine ***L_surf_inc_mean2*** and ***L_surf_inc_stdev2*** via an 80% height gaussian fit.

As in section 4.7.1.3,

Ht_surf_inc_adjustment* = *0

Calculate the standard deviation for each short segment as ***sigma_unit_fit = sqrt[(L_surf_inc_stdev2)^2 – (irf_sigma)^2].***

If ABS[(L_surf_inc_stdev2)^2 – (irf_sigma)^2] ≤ 0.000025, then sigma_unit_fit = 0.005***. If [(L_surf_inc_stdev2)^2 – (irf_sigma)^2] ≤ - 0.000025,*** then ***sigma_unit_fit*** is invalid**..**

Use values for ***H_bias_fit*** and ***H_bias_em*** equal to those of the preceeding long segment. If no preceeding long segment exists, ***H_bias_fit*** = ***H_bias_em*** = invalid.

The height adjustment value (***Ht_surf_inc_adjustment***) and is applied to each short segment ***S_Seg1_modes*** within the incomplete long segment, in conjuction with valid values of ***H_bias_fit*** and ***H_bias_EM***, to produce ***ht_water_surface*** and the program then advances to 5.3.5(C).

For very short transects where ***short seg count*** <= ***min_sseg_threshold,*** execute the same procedure as short transects, with the following changes:

1) ***Ht_surf_inc_adjustment*** = 0

2) Regardless of whether or not there is a preceding long segment, for each short segment in this case, set ***sigma_unit_fit = H_bias_fit = H_bias_em = invalid.***

5.3.3 Compute signal photon histogram of long segments per ground track

This purpose of this section is to identify a band of the water surface photons over which to detrend based on the mean water surface slope.

A) Compute signal densities and density histograms of long segments
Divide ***P*** into segments consisting of ***L_surf*** signal photons (where ***L_surf_count*** is the number of long "surface" segments) by adding a long segment ID ***L_surf_id*** to each photon in array as ***P(1:P_count).*** The assignment of ***L_surf_id*** to each photon will be done based on a simple aggregation of the short segments. That is, assign the ***L_surf_id*** = 1 to the all the photons in the first ***L_surf_count*** segments, ***L_surf_id*** =2 (if sufficient data exist) to the all the photons in the next ***L_surf_count*** short segments, and so on. All photons in anomalous short segments (***anom_flag*** =1) or that have been assigned no short segment are given a ***L_surf_id*** value of zero (0).

Histogram each long segment as ***H_Lsurf_raw(1:L_seg_count)*** using bin size ***bin_detrend*** and calculate the mode, ***H_Lsurf_mode(1:L_seg_count)***. If there is more than one mode, use the one nearest to the value of ***ht_water_coarse.*** If event that two mode options are equidistant from **ht_water_coarse**, set ***H_Lsurf_mode*** equal to the one at the higher height of those two modes.

Calculate the length of each long segment ***L_surf_length(1:L_surf_count)*** using the location of the first and last photon in the segment. Then estimate the photon density histograms of each long segment ***L_surf_ID(1:L_surf_count)*** as:
H_Lsurf_ph_dens = H_Lsurf_raw / bin_detrend / L_surf_length

Repeat over subsurface long segments of length ***L_sub*** photons as follows:
Divide ***P*** into segments consisting of ***L_sub*** signal photons (where ***L_sub_count*** is the number of long "subsurface" segments) by adding a long segment ID ***L_sub_id*** to each photon in array as ***P(1:P_count).*** The assignment of ***L_sub_id*** to each photon will be done based on a simple aggregation of the short segments. That is, assign the ***L_sub_id*** = 1 to the all the photons in the first ***L_sub_count*** segments, ***L_sub_id*** =2 (if sufficient data exist) to the all the photons in the next ***L_sub_count*** short segments, and so on. All photons in anomalous short segments (***iw_seg_anom_flag*** =0) or that have been assigned no short segment are given a ***L_sub_id*** value of zero (0).

If ***L_sub_count*** = 0 and ***L_surf_count*** >=1 calculate the surface and subsurface ranges for deconvolution, but skip the subsurface (very long) deconvolution detailed in 5.3.4(A). Instead, use default values for ***alpha_unit_fit*** and ***beta_unit_fit*** equal to ***alpha_unit_default*** and ***beta_unit_default***. Then proceed with surface (long) segment deconvolution detailed in 5.3.4(B) using these assigned subsurface parameters.

alpha_unit_default_med = 0.5
beta_unit_default_med = 0.02

Histogram each long segment as ***H_Lsub_raw(1:L_sub_count)*** using bin size ***bin_detrend*** and calculate the mode, ***H_Lsub_mode(1:L_sub_count)***. If there is more than one mode, use the one nearest to the value of ***ht_water_coarse.*** If event that two mode options are equidistant from **ht_water_coarse**, set ***H_Lsub_mode*** equal to the one at the higher height of those two modes.

Calculate the length of each long segment ***L_sub_length(1:L_sub_count)*** using the location of the first and last photon in the segment. Then estimate the photon density histograms of each long segment ***L_sub_ID(1:L_sub_count)*** as:
H_Lsub_ph_dens = H_Lsub_raw / bin_detrend / L_sub_length

B) [reserved for future development]

C) Compute range of water surface photons required for detrending.

An initial estimate of the mean and standard deviation of the water surface, based on the prior determination of ***coarse_water_ht,*** is calculated as described in the following five steps.

For ***inland_water_body_type*** = 1,2,6,7:

Step 1) In the long segment, identify all photons of ***P_sig_flag*** >= 2 within the vertical range ***coarse_water_ht*** to [***coarse_water_ht*** + ***coarse_surface_top***].

If there are fewer than ***min_mirror_cnt*** qualifying photons identified in this vertical range, extend the lower limit of the window to ***coarse_water_ht*** - ***min_mirror_multp(1)*** ****b1_sseg*** and re-identify photons, repeating with adjusted bottom limits of ***coarse_water_ht*** - ***min_mirror_multp(2)*** * ***b1_sseg*** and ***coarse_water_ht*** - ***min_mirror_multp(3)*** ****b1_sseg*** as are necessary until the minimum number of ***min_mirror_cnt*** photons are identified for analysis.

Create an array ***Lsurf_ph_mirrored*** that includes those photons as well as a synthetic set of mirrored photons at coarse_water_ht to [***coarse_water_ht*** - ***coarse_surface_bottom***], where the new photons occur at the same time as their observed counterpart, but at the opposite delta relative ***coarse_water_ht***.

Calculate the number of signal photons required to proceed as:
mirror_threshold(1) = (sum of ***sseg_sig_ph_count*** for each member short segment) / L_surf * ***min_mirror_cnt(1)***.

*If any long segment has fewer than **mirror_threshold(1)** photons to mirror then the long segment is discarded. All the indexing for long segments and very long segments are re-built from this point to the end of the transect. Restart processing with the first long segment.*

Histogram the photons of ***Lsurf_ph_mirrored*** at ***b1*** bin sizes as ***H_Lsurf_ph_mirrored_dens***, using a long segment length determined by the location of the first and last photon in the histogram, and calculate the approximate standard deviation of the photons within histogram as ***detrend_sigma*** by fitting a Gaussian to the histogram over the range of ***coarse_water_top*** to ***coarse_water_bottom***, and only where the amplitude of the Gaussian is between its peak, ***gauss_pk*** and an amplitude equal to ***gauss_pk_thres * gauss_pk***. Once the error minimization has determined the best fit, the characteristics of the fit are recorded for the long segment as ***detrend_mean***, ***detrend_sigma***, and ***detrend_amp***.

Step 2) For each observed photon in every long segment ***L_surf_ID(1:L_surf_count***), test whether or not it falls within the detrending band of elevation. If the height of the photon in ***P(1:P_count)*** is within the heights calculated as ***coarse_water_ht (***20220720t1) +/- (***detrend_width * detrend_sigma),*** it falls in the detrending band and so add descriptor ***detrend_band_flag*** = 1 in ***P(1:P_count).*** If it is not within the band or is non-signal/ anomalous, ***detrend_band_flag*** = 0 is added for this attribute to array table ***P***.

Calculate the number of signal photons required to proceed as:
mirror_threshold(2) = (sum of ***sseg_sig_ph_count*** for each member short segment) / L_surf * ***min_mirror_cnt(2)***.

*Check for a minimum of **mirror_threshold(2)** photons (selected photons and their mirrored) to fall within the detrending band, failing which the transect is exited. ATL13 will have no short segments belong to this discarded transect, and transect numbering will be contiguous. Processing will pickup on what is now the next transect (same water body or if last one of a water body was discarded then first transect of next water body)*

For ***inland_water_body_type*** = 5:

Calculate the approximate standard deviation of the photons within each long segment histogram ***H_Lsurf_ph_dens*** as: ***detrend_sigma(1:L_surf_count)*** by fitting a Gaussian to the histogram and minimizing the error of fit over the range only where the amplitude of the Gaussian is between its peak, ***gauss_pk*** and an amplitude equal to ***gauss_pk_thres * gauss_pk***. Once the error minimization has determined the best fit, the characteristics of the fit are recorded for the long segment as ***detrend_mean***, ***detrend_sigma***, and ***detrend_amp***.

For each observed photon in every long segment ***L_surf_ID(1:L_surf_count***), test whether or not it falls within the detrending band of elevation. If the height of the photon in ***P(1:P_count)*** is within the heights calculated as ***H_Lsurf_mode*** +/- (***detrend_width * detrend_sigma),*** it falls in the detrending band and so add descriptor ***detrend_band_flag*** = 1 in ***P(1:P_count).*** If it is not within the band or is non-signal/ anomalous, ***detrend_band_flag*** = 0 is added for this attribute to array table ***P***.

D) Detrend all photons based on water surface photons and compute histograms

Detrend all the data based on a line fit to only the narrow band of surface photons for each long segment.
Fit a trend line (default assume linear where y=ax+b) to each L_seg_ID(1:L_seg_count), using only photons where ***detrend_band_flag*** =1, to capture each segment's ***a_detrend, b_detrend(1:L_surf_count)***. Add ***P_ht_detrended*** for every photon in ***P*** as:
***P_ht_detrended*(1:P_count) = *P_ht_g*(1:P_count) –**
[*a_detrend*(1_P_count)*(*P_time*(1:P_count) + *b_detrend*(1:P_count)]

For ***inland_water_body_type*** = 1,2,6,7
-- ***L_surf_P_ht_mirrored_detrended* = *Lsurf_ph_mirrored***(:) – **[*a_detrend* * *Lsurf_ph_mirrored_time***(:) + ***b_detrend***]
--Calculate the mean height of the newly detrended mirrored photons ***L_surf_P_ht_mirrored_detrended*** as ***detrend_band_ph_mean***.

Based on the detrended heights for both sets (surface & subsurface) of long segments, calculate the histograms (***h_detrend_surf*** & ***h_detrend_subsurf***) of each, over the range ***detrend_max_h*** to ***detrend_min_h***.

Calculate the long segment background ***bckgrd_dnsty_50sht_bin_Lseg*** as the sum of all the ***bckgrd_count_50sht_bin*** values for each short segment in the long segment. Bckgrd_Dnsty_50sht_bin is the same for each bin in the histogram. For purposes of reporting, the average background removed from each short segment is defined as ***bckgrd_dnsty_50sht_bin_Sseg* = *bckgrd_dnsty_50sht_bin_Lseg*** / (***L_surf*** / ***S_seg1(iw_body_type)***).

Remove the background in the surface and subsurface histogram by subtracting ***bckgrd_dnsty_50sht_bin _Lseg*** from each bin in the histograms, creating arrays ***h_detrend_surf2*** and ***h_detrend_subsurf2***. Note that for any bin where removing the background results in a negative value, assign a count of zero.

Create normalized histogram ***h_detrend_surf_norm*** where each element is defined as:

h_detrend_surf_norm$_i$ ***= h_detrend_surf2***$_i$ ***/ ∑(h_detrend_surf2)***$_{1\text{-}n}$
and calculate the mode of the histogram as ***P_ht_detrend_surf_norm_mode.***

Create normalized histogram ***h_detrend_subsurf_norm*** where each element is defined as:

h_detrend_subsurf_norm$_i$ ***= h_detrend_subsurf2***$_i$ ***/ ∑(h_detrend_subsurf2)***$_{1\text{-}n}$
and calculate the mode of the histogram as ***P_ht_detrend_subsurf_norm_mode.***

For ***inland_water_body_type*** = 1,2,6,7:

Step 3) Calculate the approximate standard deviation of the photons within each long segment histogram ***L_surf_P_ht_mirrored_detrended*** as: ***detrend_sigma2(1:L_surf_count)*** by fitting a Gaussian to the histogram over the range [***detrend_band_ph_mean*** + ***coarse_detrended_width*detrend_sigma***] to [***detrend_band_ph_mean*** - ***coarse_detrended_width*detrend_sigma***], only where the amplitude of the Gaussian is between its peak, ***gauss_pk2*** and an amplitude equal to ***gauss_pk_thres * gauss_pk2***. Once the error minimization has determined the best fit, the characteristics of the fit are recorded for the long segment as ***detrend_mean2***, ***detrend_sigma2***, and ***detrend_amp2***.

Calculate the number of signal photons required to proceed as:
mirror_threshold(3) = (sum of ***sseg_sig_ph_count*** for each member short segment) / L_surf * ***min_mirror_cnt(3)***.

If the total number of photons (selected photons and the mirrored) after the above filter is under ***mirror_threshold(3)*** *for any long segment, then exit the transect. ATL13 will have no short segments belong to this discarded transect, and transect numbering will be contiguous. Processing continues on what is now the next transect (of either the same water body or if last one of a water body was discarded, then first transect of next water body)*

Step 4) For each very long segment, identify all photons in ***L_surf_P_ht_mirrored_detrended*** of ***P_sig_flag*** >= 2 for each member long segment (lseg(1:3)) within the vertical range ***detrend_band_ph_mean(lseg)*** to [***detreand_band_ph_mean(lseg)*** + ***coarse_surface_top***]. Create an array ***L_subsurf_P_ht_mirrored_detrended*** that includes those photons as well as a synthetic set of mirrored photons at ***detreand_band_ph_mean(lseg)*** to [***detreand_band_ph_mean(lseg)- coarse_surface_bottom***], where the new photons occur at the same time as their observed counterpart, but at the opposite delta relative ***detreand_band_ph_mean(lseg)***.

Calculate the number of signal photons required to proceed as:
mirror_threshold(4) = (sum of ***sseg_sig_ph_count*** for each member short segment) / L_sub * ***min_mirror_cnt(4)***.

If the total number of photons (selected photons and the mirrored) after the above filter is less than ***mirror_threshold(4)*** *for either long segment, then exit the transect. ATL13 will have no short segments belong to this discarded transect. Transect numbering will not show a gap. Processing will pickup on what is now the next transect (same water body or if last one of a water body was discarded then first transect of next water body)*

Step 5) Histogram the photons of ***L_subsurf_P_ht_mirrored_detrended*** ***~~Lsub_ph_mirrored~~*** at ***b1*** bin sizes as ***H_Lsub_ph_mirrored_dens***, using a long segment length determined by the location of the first and last photon in the histogram, and calculate the approximate standard deviation of the photons within histogram as ***detrend_sigma2_Lsub*** by fitting a Gaussian to the histogram over the range of max(***detreand_band_ph_mean***(lseg(1:3)))+3*max(***detrend_sigma2***(lseg(1:3))) to min(***detreand_band_ph_mean***(lseg(1:3)))-3*max(***detrend_sigma2***(lseg(1:3))), and only where the amplitude of the Gaussian is between its peak, ***gauss_pk*** and an amplitude equal to ***gauss_pk_thres * gauss_pk***. Once the error minimization has determined the best fit, the characteristics of the fit are recorded for the long segment as ***detrend_mean2_Lsub***, ***detrend_sigma2_Lsub***, and ***detrend_amp2_Lsub***.

Calculate the number of signal photons required to proceed as:
mirror_threshold(5) = (sum of ***sseg_sig_ph_count*** for each member short segment) / L_sub * ***min_mirror_cnt(5)***.

If the total number of photons (selected photons and the mirrored) for the very long segment after the above filter is less than ***mirror_threshold(5)****, then exit the transect. ATL13 will have no short segments belong to this discarded transect. Transect numbering will not show a gap. Processing will pickup on what is now the next transect (same water body or if last one of a water body was discarded then first transect of next water body). Note: Jyothi says there are no exits on this case. Since it came in with at least 600 photons the check is more for safety/consistency.*

For very long segments, isolate the photons from each member long segment that are 0-5 above lseg mean in array Lsub_ph_mirrored and histogram them as H_Lsub_mirrored_dens.

For ***inland_water_body_type*** = 5:
Calculate the approximate standard deviation of the photons within each long segment histogram ***h_detrend_surf_norm*** as: ***detrend_sigma2(1:L_surf_count)*** by fitting a Gaussian to the histogram and minimizing the error of fit over the range only where the amplitude of the Gaussian is between its peak, ***gauss_pk2*** and an amplitude equal to ***gauss_pk_thres * gauss_pk2***. Once the error minimization has determined the best fit, the characteristics of the fit are recorded for the long segment as ***detrend_mean2***, ***detrend_sigma2***, and ***detrend_amp2***.

Calculate the approximate standard deviation of the photons within each very long subsurface segment histogram ***h_detrend_subsurf_norm*** as: ***detrend_sigma2_Lsub(1:L_sub_count)*** by fitting a Gaussian to the histogram and minimizing the error of fit over the range only where the amplitude of the Gaussian is between its peak, ***gauss_pk2_Lsub*** and an amplitude equal to ***gauss_pk_thres * gauss_pk2_Lsub***. Once the error minimization has determined the best fit, the characteristics of the fit are recorded for the long segment as ***detrend_mean2_Lsub***, ***detrend_sigma2_Lsub***, and ***detrend_amp2_Lsub***.

5.3.4 Deconvolve instrument response from surface and subsurface signal histograms for each ground track

Subsurface attenuation is computed for the long segments in order to accumulate enough signal photons to determine a good fit. Specifically, the attenuation term will be computed as described in Sections 4.2.3 and 4.5.3.
Once the subsurface parameters are determined, the exponential is assumed to extend up into the Gaussian in order to correct the original assumption that all the photons in the near-Gaussian are surface photons. Analysis of MABEL data indicates that this computation only needs to be iterated once due to the small magnitude of the subsurface component.

A) Identify subsurface signal photons, estimate subsurface parameters
Estimate the amplitude parameter, β, and the attenuation coefficient, α, as described in Section 4.5.3., described here as alpha_XX and beta_XX, with c_l term represented by the parameter Lidar_subsrf_bckscat. The calculation of the subsurface deconvolution is done using the L_sub long segments.

Before beginning subsurface analysis, identify a potential water body bottom or other subsurface anomaly within a long segment by calculating the mean and standard deviation (***bottom_search_mean***, ***bottom_search_stdev***) of normalized photon counts

h_detrend_subsurf_norm for the bins within the subsurface range ***detrend_mean2 – bottom_search_start*detrend_sigma2*** and ***bottom_search_max***. This calculation is performed at a single bin height across multiple long segments in the case of the mean, and within a single long segment's vertical profile in the case of the standard deviation. The mean (***bottom_search_mean***) is calculated at each bin height over uninterrupted groups of long segements in a horizontal orientation, incorporating the binned normalized photon counts across long segments. The standard deviation, ***bottom_seach_stdev***, is calculated in a vertical orientation, where the binned normalized photon counts of each long segment determine the standard deviation to be used for testing each bin in that long segment.

After calculating these statistics, loop through every bin within that subsurface range for each value of ***bottom_search_threshold(i=1:3)*** and set ***bottom_search_ht*(*L_surf_ID,i)*** equal to the <u>minimum</u> height at which (***btm_mean_a* bottom_search_mean + (bottom_search_threshold(i)*bottom_search_sigma))*** is exceeded. If the criteria is not satisfied at any height in the range for a given long segment, set ***bottom_search_id*(*L_surf_ID,i)*** = invalid for that long segment.

bottom_search_start = 12
btm_mean_a = 2.0

The apparent (detrended) height of the significant anomaly for a long segment, ***subsurf_anom_ht***, is determined by the strictest criteria satisfied, ie, the greatest value for ***bottom_search_threshold*** at which an anomaly was found. Therefore ***subsurf_anom_ht(L_surf_ID)*** = ***bottom_search_ht(L_surf_ID,max(i))*** where valid. Satisfied ***bottom_search_threshold*** criteria values [3 5 7] correspond to ***QF_Subsurf_Anomaly*** flags of [3 2 1], respectively, as outlined in section 5.3.5 (C). If no anomaly is found at any threshold testing level, short segments comprising the long segment will be assigned QF_Subsurf_Anomaly = 999.

Apparent water depth is estimated as ***water_depth_app(for each sseg)*** = ***detrend_mean2(parent lseg) – subsurf_anom_ht (parent_lseg)*** + ***(HM_bias_EM(parent_lseg)*** + ***HM_bias_fit(parent_lseg).*** The water depth and the likelihood that the subsurface anomaly is bottom, ***QF_Subsurf_Anomaly***, are reported at the short segment rate as product output. If ***subsurf_anom_ht*** = invalid, then ***water_depth_app*** = invalid.

The distribution of the subsurface signal photons is initially approximated from the observed histogram below three standard deviations below the mode. The exponential will be fit (as described in section 4.5.3) only to the subsurface distribution from ***subsurface_h = mode(h_detrend_norm) – 3*detrend_sigma2*** down to ***subsurf_bottom*** or the bottom of the

water body, whichever is higher. In order to determine ***subsurf_bottom***, first compute the mean and standard deviation (***subsurf_ph_mean***, ***subsurf_ph_stdev***) for all photons in the long segment that occur below ***subsurface_h*** and have a signal classification (***P_signal_flag***) of ***subsurf_ph_class*** or higher. If the number of photons ***subsurf_ph_count*** that meet these criteria is not greater than ***subsurf_ph_count_threshold*** then the long segment should not go through subsurface deconvolution and the default alpha and beta (***alpha_unit_default_med, beta_unit_default_med)*** should be used for the long segment during the total system devonvolution, like as in the case of a medium contingency.
Assuming there are enough qualified subsurface photons to proceed, then the bottom of the subsurface calculation zone is designated as:
subsurf_bottom = ***subsurf_ph_mean*** – 3 * ***subsurf_ph_stdev***

The distribution of the subsurface signal photons of the observed histogram is initially approximated starting from below ~~three~~ eight standard deviations (detrend_sigma2) below the mode. The exponential will be fit (as described in section 4.5.3) only to the subsurface distribution from ***subsurface_h = mode(h_detrend_norm) – ~~3~~ 8 *detrend_sigma2*** down to ***subsurf_bottom*** or ~~the bottom of the water body~~***subsurf_bottom2_param***, whichever is higher. In order to determine ***subsurf_bottom***, first compute the mean and standard deviation (***subsurf_ph_mean***, ***subsurf_ph_stdev***) for all photons in the long segment that occur below ***subsurface_h*** and have a signal classification (***P_signal_flag***) of ***subsurf_ph_class*** or higher. If the number of photons ***subsurf_ph_count*** that meet these criteria is not greater than ***subsurf_ph_count_threshold*** then the long segment should not go through subsurface deconvolution and the default alpha and beta (***alpha_unit_default_med, beta_unit_default_med)*** should be used for the long segment during the total system devonvolution, like as in the case of a medium contingency.

subsurf_bottom2_param = 10 ~~15~~

However, if a water body bottom was previously identified, it should be employed to determine the bottom of the subsurface calculation zone instead. Therefore, if ***QF_Subsurf_Anomaly(L_surf_ID)*** = 1 for one long segment belonging to very long segment ***L_sub_ID***, set ***subsurf_bottom(L_sub_ID)*** = ***subsurf_anom_ht (L_surf_ID)*** + ***bottom_range_buffer * b_long***. If ***QF_Subsurf_Anomaly(L_surf_ID)*** = 1 for more than one long segment within the very long segment, use the maximum ***subsurf_anom_ht*** value (highest height) determined to be eligible by ***QF_Subsurf_Anomaly*** = 1.

If ***subsurf_bottom(L_sub_ID)*** > ***subsurface_h(L_sub_ID)***, do not process long segment ***L_sub_ID*** through the subsurface deconfovlution scheme to determine its attenuation characteristics. Instead, set ***alpha_unit*(L_sub_ID)** and ***lidar_subsrf_bckscat_unit*** (***L_sub_ID***) equal to default values ***alpha_unit_default_med*** and ***beta_unit_default_med.***

The isolated subsurface signal is arrayed as ***P_ht_long_subsurface***. Smooth the subsurface array via moving average where **m_avg_d** = 5 depth bins to create ***P_ht_long_subsurf_mavg***.

As per section 4.5.3, fit an exponential curve to the histogram and record ***alpha_resp(1:L_sub_count)*** and ***lidar_subsrf_bckscat_resp(1:L_sub_count)*** for each long segment ***L_sub_ID(1:L_sub_count).*** Any bin where ***bottom_search_id***(***L_surf_ID)*** is not equal to zero, and therefore marked as a subsurface anomaly, should be excluded from contributing to the fitting. In cases where either or both of ***alpha_resp or lidar_subsrf_bckscat_resp*** are outside the ranges of ***lidar_coeff_alpha_unit_min***(***inland_water_body_type***,2) to ***lidar_coeff_alpha_unit_max***(***inland_water_body_type***,2) and ***lidar_coeff_alpha_unit_min***(***inland_water_body_type***,1) to ***lidar_coeff_alpha_unit_max***(***inland_water_body_type***,1), respectively, end the subsurface deconvolution outlined in this section and set ***alpha_unit_fit*** = ***alpha_unit_default*** and ***beta_unit_fit*** = ***beta_unit_default***. If default values are utilized for this reason, mark the subsurface characteristic quality flags as:
QF_subsurface_attenuation = -2 if ***alpha_resp <***
lidar_coeff_alpha_unit_min(***inland_water_body_type***,2),
QF_subsurface_attenuation = 2 if ***alpha_resp >***
lidar_coeff_alpha_unit_max(***inland_water_body_type***,2),
otherwise ***QF_subsurface_attenuation*** = 0, and
QF_subsurface_backscat_ampltd = -2 if ***lidar_subsrf_bckscat_resp <***
lidar_coeff_alpha_unit_min(***inland_water_body_type***,1),
QF_subsurface_backscat_ampltd = 2 if ***lidar_subsrf_bckscat_resp >***
lidar_coeff_alpha_unit_max(***inland_water_body_type***,1),
otherwise ***QF_subsurface_backscat_ampltd*** = 0.

Begin iterated convolution of the instrument response and the unknown unit response within the framework of a constrained model (as described in 4.5.3, eq. 4.11) in a nested loop of ***alpha_unit*** from ***lidar_coeff_alpha_unit_min***(***inland_water_body_type***,2) to ***lidar_coeff_alpha_unit_max***(***inland_water_body_type***,2) in increments of ***lidar_coeff_alpha_unit_incr***(***inland_water_body_type***,2) within a loop of ***lidar_subsrf_bckscat_unit*** from ***lidar_coeff_alpha_unit_min***(***inland_water_body_type***,1) to ***lidar_coeff_alpha_unit_max***(***inland_water_body_type***,1) in increments of ***lidar_coeff_alpha_unit_incr***(***inland_water_body_type***,1). Before entering this loop, establish an initial deconvolution result where ***alpha_unit*** = ***lidar_coef_alpha_unit_initial*** for all body types. Once the deconvolution state is calculated based on ***lidar_coeff_alpha_unit_initial***, the full loop begins – based on water body type – at the ***alpha_unit*** described in ***lidar_coeff_alpha_unit_min***. (The step from ***lidar_coeff_alpha_unit_min*** to ***lidar_coeff_alpha_unit_min*** may vary depending on water body type.) The solution is noted when the absolute value of the standard error of the differences between the observed fit and the modeled fit curves using ***alpha_obs*** and ***alpha_model*** as well as ***lidar_subsrf_bckscat_obs*** and ***lidar_subsrf_bckscat_model*** is minimized. Although the convolution is performed over the entire vertical profile from ***subsurface_h*** to ***subsurf_bottom***, the error minimization is calculated only over the subsurface range represented by height range arrayed in ***P_ht_long_subsurface***. When this occurs, note values of ***alpha_unit_fit*** and ***lidar_subsrf_bckscat_unit_fit*** for each long segment ***L_sub_ID(1:L_sub_count).***

It is possible that the minimum error of the initial and looped deconvolution calculations was identified in the initial case where alpha equals ***lidar_coef_alpha_unit_initial***. If this is the case, set ***QF_subsurface_attenuation*** = -1. If the minimum error was found where ***alpha_unit*** = ***lidar_coeff_alpha_unit_max(inland_water_body_type***,2), set ***QF_subsurface_attenuation*** = -1. Otherwise, if the minimum error was found when ***alpha_unit*** falls between the initial and maximum values, ***QF_subsurface_attenuation*** = 0.

Similarly, if the minimum system error is found when ***lidar_subsrf_bckscat_unit*** equals ***lidar_subsurf_bckscat_unit_min(inland_water_body_type***,2), set ***QF_subsurface_backscat_ampltd*** = -1. If the minimum error was found where ***lidar_subsrf_bckscat_unit*** equals ***lidar_subsurf_bckscat_unit_max(inland_water_body_type***,2), set ***QF_subsurface_backscat_ampltd*** = 1. Otherwise, if the minimum error was found when ***lidar_subsrf_bckscat_unit*** falls between the minimum and maximum values, set ***QF_subsurface_backscat_ampltd*** = 0.

For reporting purposes, calculate ***beta_unit_fit(L_sub_ID) = lidar_subsrf_bckscat_unit fit(L_sub_ID) / alpha_unit fit(L_sub_ID)***, and, when default values of ***alpha_unit_fit*** and ***lidar_subsurf_bckscat_unit_fit*** were not required to be used:
subsurface_backscat_ampltd = lidar_subsurf_bckscat_unit_fit
Subsurface_attenuation = alpha_unit_fit where ***subsurface_backscat_ampltd*** and ***subsurface_attenuation*** are reported as ATL13 product output.
If default values of ***alpha_unit_fit*** and ***lidar_subsurf_bckscat_unit_fit*** were used, set ***subsurface_attenuation*** and ***subsurface_backscat_ampltd*** to invalid. The quality flags ***QF_subsurface_attenuation*** and ***QF_subsurface_backscat_ampltd*** should also be set to invalid when this occurs, unless the flag has access to an appropriate value to indicate the reason that default values were used.

If the solution is intractable, assign ***L_sub_flag***=1 to the L_seg_ID, and assume ***lidar_subsrf_bckscat_unit_fit***=1 and ***alpha_unit_fit***= 0.01 for the long segment.

B) Estimate water surface height statistics including mean, standard deviation, slope, and associated products

The distribution of the surface signal photons is initially approximated from the observed histogram from three standard deviations below the mode up and through 3 standard deviations of the mode + 1 meter. The full range of deconvolution for the at the surface segment scale begins at a top ***surface_top(L_surf_ID)*** = ***detrend_mode2_ht(L_surf_ID) + surf_top_param * detrend_sigma2(L_surf_ID) + surf_top_buffer.*** The bottom of the deconvolution range is determined as ***ht_sbr_lo_detrend(L_surf_ID) = subsurf_anom_ht(L_surf_ID) + bottom_range_buffer * b_long, if QF_Subsurf_Anomaly(L_surf_ID)*** = 1**.** If ***QF_Subsurf_Anomaly(L_surf_ID)*** does not equal (1), set ***ht_sbr_lo_detrend(L_surf_ID)*** equal to ***subsurf_bottom(L_sub_ID***) for the very long segment to which the long segment belongs.

Water surface mean height and standard deviation are estimated by fitting the histogram of a convolved model as described in 4.2 to the histogram of the observations.
The precise type of fit used to model the surface will depend on the description of the lake crossing, ***water_body_i_area*** and ***water_body_id_xlength***.

Assume a Gaussian surface height distribution where:
The distribution of the surface signal photons is initially approximated from the observed histogram isolated from 3*sigma above the mode to 2*sigma below the mode. The isolated surface signal is arrayed as ***P_ht_long_surface.*** Parameters of the exponential portion of the fit are as calculated as the optimal values determined in section 5.3.4 (A***).***

Begin iterated convolution of ***inst_pulse_norm*** (the normalized instrument response) and the unknown unit surface response within the framework of a constrained model (as described in 4.5.4) in a nested loop of mean heights ***HM_unit*** (***amp_mean_sig_min(2):amp_mean_sig_max(2)***) in increments of ***amp_mean_sig_incr(2)*** within loops of of ***sigma_unit_surf*** over the range of ***amp_mean_sig_min(3)*** to ***amp_mean_sig_max(3)*** by ***amp_mean_sig_incr(3)*** increments and amplitude fit range of ***amp_mean_sigma_min(1)*** to ***amp_mean_sigma_max(1)*** in steps of ***amp_mean_sigma_incr(1)***. The solution is noted when the absolute value of the standard error of the differences between the observed fit (***h_detrend_surf_norm***) and the modeled fit (***sys_tot_resp_surf***) curves using the absolute difference between ***HM_model*** (the mean height of the model) and that of the observation ***HM_obs*** in addition to the absolute difference between the standard deviation of the model ***sigma_model_surf*** and that of the observation ***sigma_obs_surf*** is minimized. The convolution is performed over the entire vertical profile from ***subsurface_h*** to ***LSBR_lo***, as is the error calculation.
When error is minimum over the surface profile range, set the ***HM_unit_fit*** equal to the ***HM_unit*** height and the ***sigma_unit_fit*** equal to the ***sigma_unit*** height.

Calculate the mode of the best fitted unit histogram as ***H_mode_fit***.
This process is repeated for every long segment ***L_surf_ID(1:L_surf_count)***. For each of the long segments, calculate the deconvolved surface response height adjustment as in 4.7.3.4,
A height adjustment value (***H_unit_adj***) is calculated for every long segment where ***L_surf_ID(1:L_surf_count)***.

H_unit_adj(L_surf_ID)=
HM_unit_fit(L_surf_ID) – irf_width_x*irf_sigma – detrend_mean3(L_surf_ID),

and ***irf_width_x*** = 3.

For transects that do not have a sufficient number of short segments to go through the full deconvolution necessary to produce ***H_unit_adj*** in this manner, set ***H_unit_adj*** = invalid.

C) Estimate other related variables
Compute other variables including significant wave height and biases. Significant wave height is calculated as ***sig_wv_ht*** = 4 * ***sigma_unit_fit***. For reporting of output***, stdev_water_surf = sigma_unit_fit.*** If ***sigma_unit_fit*** is invalid, then ***stdev_water_surf = sig_wv_ht*** = invalid***.*** For QF_IWP=0, estimate stdev_water_surf as the standard deviation of the signal photons in the partial short segment.

Calculate the approximate standard deviation of the photons within each long segment histogram ***sys_tot_resp_surf*** as: ***detrend_sigma3(1:L_surf_count)*** by fitting a Gaussian to the histogram and minimizing the error of fit over the range only where the amplitude of the Gaussian is between its peak, ***gauss_pk3*** and an amplitude equal to ***gauss_pk_thres * gauss_pk3***. Once the error minimization has determined the best fit, the characteristics of the fit are recorded for the long segment as ***detrend_mean3 detrend_sigma3***, and ***detrend_amp3***.

Calculate the goodness of fit of the constrained deconvolution for each long segment based on the centroid elevations of ***h_detrend_surf_norm*** (the observations) and ***best_tot_resp*** (the total integrated response***).*** Over the bin depths ***fit_bias_bin_hts(1:n)*** within the range ***detrend_mean3*** +/- ***ft_bias_range_coeff*detrend_sigma3***, calculate the goodness of fit bias as:
H_bias_fit = [SUM(1:n) (***h_detrend_surf_norm(i) * fit_bias_bin_hts(i)) / SUM(1:n) h_detrend_surf_norm(i)] -*** [***SUM(1:n)*** (***best_tot_resp(i) * fit_bias_bin_hts(i)) / SUM(1:n) besttot_resp(i)***]

Electromagnetic bias
H_bias_EM = -(3 * pi * ***sig_slope*** * (***view_angle_norm***^{2} – 1) * ***sigma_unit_fit)***

sig_slope = ***sigma_unit_fit / wvlen_spec_peak***, where
wvlen_spec_peak = T_pk_atlas * V_gt where ***T_pk_atlas*** is estimated as the longest time between two sequential up-crossings where only signal photons near the surface (within +/- 3****detrend_sigma2***) are included. The upcrossing times should only be considered in the identification of the maximum time between upcrossings when there is no interruption/gap (due to anomalies) in the short segments between them.

T_pk = (wvlen_spec_peak*2*pi/g)^0.5

view_angle_norm = altas_zen /(mean_sq_slope)^0.5

Depending on the value of ***sigma_unit_fit***, calculate ***mean_sq_slope*** as follows:
If ***sigma_unit_fit*** **<** 0.245m***,***
    mean_sq_slope **= 0.0549 *** ***sigma_unit_fit***^0.25
If 0.245**<=** ***sigma_unit_fit*** <= 0.885m***,***
    mean_sq_slope = 0.003 + 0.0724****(sigma_unit_fit***)^0.25
If ***sigma_unit_fit*** > 0.885m***,***
    mean_sq_slope = 0.069$\log_{10}$***[sigma_unit_fit]*** + 0.0748

Spectral Analysis

T_z_atlas = The average time between upcrossings, estimated as the average of all valid times between valid upcrossings (where no anomalous short segments exist between the two upcrossings).

T_z = (***T_z_atlas * V_gt * 2 * pi*** / ***g***)^0.5

T_c_atlas = Identify all valid crests (where no anomalous short segments exist between the two crests nor within the 3 photons necessary to define a crest) at photon(n) whose height > photon(n-1) & height> photon(n+1). Estimate ***T_c_atlas*** as the average of all valid times between valid crests.

T_c = (T_c_atlas * V_gt * 2 * pi / ***g***)^0.5

M_zero = (***sig_wv_ht/4***)^2
M_two = M_zero / (T_z / 2*pi)^2
M_four = M_two / (T_c / 2*pi)^2

spec_width = (1 – ***M_two***^2 / ***(M_zero*M_four***))^0.5

<u>D) Compute water reflectance</u>

Estimate the variance of the wave slope for each long segment as described in equation 5.15 as:
slope_var = 0.0549 * ***sigma_unit_fit***$^{0.25}$ when ***sigma_unit_fit*** ≤ 0.245
slope_var = 0.003 + 0.0724(***sigma_unit_fit***)$^{0.5}$ when $0.245 <$ ***sigma_unit_fit*** ≤ 0.885
slope_var = 0.069LOG$_{10}$[***sigma_unit_fit***] + 0.0748 when 0.885 m < ***sigma_unit_fit***

Estimate theoretical surface reflectance and atmospheric transmittance for long segments as described in Sections 3.1 and 4.2 and 4.6.3.

Based on Equation 4.14, estimate the wind speed ***u_10*** using ***sigma_unit_fit,*** and then use that result to estimate ***slope_var*** as defined in equation 4.15.

If ***u_10*** differs by more than 10 m/s any available modeled wind speed ***u_spd***, set ***T_atm_flag*** = 1.

gamma_surf = ***c_fresnel*** / (4*pi****slope_var***^{2}****atlas_azm***)
* exp(-tan^2(***atlas_azm***)/2****slope_var***^{2})

Calculate ***W*** as described in equation set 4.4.
Calculate foam backscatter as in Eqn 4.3.
gamma_foam = ***W*** * ***gamma_surf*** * (pi*10^{-6}) * ***u_spd***$^{2.55}$ * cos(***atlas_azm***) / pi

Calculate ***gamma_u*** as the sum of the scatter at each height in ***P_ht_long_subsurface***:
gamma_u = ***beta_unit_fit*** * ***alpha_unit_fit*** * ***c_adj*** * exp(-***alpha_unit_fit*** * ***P_ht_long_subsurface***)

Total theoretical surface reflectance is estimated as:
gamma_tot = (***gamma_surf****(1-**W**) + ***gamma_foam*** * ***W*** + ∑***gamma_u***

T_atm is estimated as the square root of the ratio of the observed apparent reflectance ***gamma_app*** and the theoretical reflectance ***gamma_tot.***

5.3.5 Inland Water Data Product Output

<u>A) Compute short segment water surface height products (~100 signal photons)</u>

The location of the reported statistics for the short segments will be determined by the mean location of all only the photons within the short segment where ***P_sig_flag*** is equal to or greater than ***sig_threshold*** and bounded by a surface range estimated for the individual short segment by ***S_Seg1_modes*** + ***sseg_surf_threshold****sigma_detrend*** to ***S_Seg1_modes – sseg_surf_threshold*sigma_detrend***. Calculate the mean lat, lon, height, and time (***sseg_mean_lat, sseg_mean_lon sseg_mean_ht, sseg_mean_time)*** for the photons where the sig_threshold and range boundary criteria are met. Select as an index photon the photon nearest the mean location and note that segment index photon location, time, and geoid and other natively geosegment-rate statistics as ***segment_lat***, ***segment_lon***, ***segment_delta_time***,***segment_geoid, segment_dac, segment_tide_ocean, segment_tide_equillibrium, segment_azimuth*** and **segment_ref_elev**.

Calculate the horizontal refraction adjustment to the location bottom of the water body short segment, ***delta_e_offset*** and ***delta_n_offset*** by:

incidence_angle = pi/2 - ***segment_ref_elev***

ref_refraction = $\sin^{-1}(n_1 * \sin($***incidence_angle***$) / n_2)$

slant_range = ***water_depth_app*** / cos(***incidence_angle***)

slant_range_corr = ***slant_range*** * n_1 / n_2

range_corr = sqrt(**slant_range_corr**^{2} + ***slant_range***^{2} - 2****slant_range_corr*slant_range*** *cos(***incidence_angle*** - ***ref_refraction***))

delta_z_angle = pi/2 – ***incidence_angle*** - $\sin^{-1}$(***slant_range_corr****(sin(***incidence_angle*** – ***ref_refraction***))/***range_corr***)

delta_y_offset = ***range_corr*** * cos(***delta_z_angle***)

bottom_e_offset = ***delta_y_offset*** * sin(***segment_azimuth***)
bottom_n_offset = ***delta_y_offset*** * cos(***segment_azimuth***)

Convert ***bottom_e_offset*** and ***bottom_n_offset*** distances (meters) to an actual bottom location in lat/lon based on apparent location ***sseg_mean_lat*** and ***sseg_mean_lon***, and write ***bottom_lat*** and ***bottom_lon*** results as output products at the short segment rate.

delta_z_offset = ***range_corr*** * sin(***delta_z_angle***)
water_depth = ***water_depth_app - delta_z_offset***

If ***water_depth_app = invalid,*** then ***water_depth = invalid*** for the short segment**.**

The height adjustment ***H_unit_adj*** estimated from deconvolution will be applied to the previously created short segments. For each short segment ***S_seg1_ID(1:S_seg1_count),*** adjust the histogram mode by the height adjustment value (***H_unit_adj***) for the long segment of which the short segment is a part. The product height for the short segment is ***S_Seg_ht_product = sseg_mean_ht + H_unit_adj + H_bias_fit + H_bias_EM - segment_fpb_correction.***

In a case where any of ***H_unit_adj, H_bias_fit***, ***H_bias_EM***, or ***segment_fpb_correction*** are invalid for any long segment on a water body transect, it is set to invalid for all short segments assigned to the long segment**,** the invalid term(s) excluded from the calculation of ***S_Seg_ht_product***, and processing continues with the subsequent long segment**.**

ht_ortho = S_seg_ht_product
segment_apparent_ht = sseg_mean_ht
segment_bias_EM = H_bias_EM
segment_bias_fit = H_bias_fit

The slope of each short segment***, Segment_slope_trk_bdy(S_seg1_ID)*** will be noted as the slope of the line fit used in the detrending module. Therefore set ***Segment_slope_trk_bdy(S_seg1_ID)*** equal to the ***a_detrend(L_surf_ID)*** of the ***L_surf_ID*** to which it corresponds.

Remove geoid adjustment to report geodetic height as ***ht_water_surface = ht_ortho*** + ***segment_geoid(S_seg1_ID).***

Estimate the wind speed for each long segment as described in eqution 4.14 as:
met_wind10_ATL13 = sqrt (***sigma_unit_fit*** / 0.005), reporting the long segment result at each short segment within as ATL13 output. If ***sigma_unit_fit*** = invalid for a given short segment, then ***met_wind10_ATL13*** = invalid for the short segment.

Compute the wind speed as defined by ATL09 input data as:
met_wind10_ATL09 = sqrt(***MET_U10M***^2 + ***MET_V10M***^2) where the ATL09 wind vectors used for a short segment are identified with the closest ***time_ATL09*** to ***sseg_mean_time*** for that short segment. Report the result at the short segment output rate.

Report the surface (skin) temperature at the short segment rate on the ATL13 product as ***met_ts_ATL09***, based on interpolated ATL09 input ***MET_TS***,

Report the snow/ice flag ***snow_ice_ATL09*** at the short segment rate as the largest value of the neighboring ATL09 ***snow_ice*** inputs to the short segment.

Retrieve cloud confidence flags below as derived in ATL09 and convert to ATL13 short segment rate using nearest neightbor : Cloud_Flag_ASR_ATL09, Cloud_Flag_Atm_ATL09, Layer_Flag_ATL09.

Determine full-width half-max (ns) for each short segment as ***segment_FWHM*** = 7.84 * ***stdev_water_surf***, where ***stdev_water_surf*** is the reported standard deviation for each short segment. The strength of the return signal is estimated as ***strength_ATL13_sseg*** = S_seg1*(0.7) / ***sseg_length***.

Based on these two parameters (nominally ***width*** and ***strength*** in CAL_19 table), identify the first photon bias correction ***ffb_corr*** in the **CAL_19** table and report ***segment_fpb_correction*** = 0.00015 *0.5* ***ffb_corr*** as ATL13 output for each short segment.

B) Compute Multi-Beam Water Height Data Products

Aspect and maximum slope (***aspect, max_slope***) will be calculated between each pair of strong beams as described in Section 3.4 and shown in Figure 3.5. Aspect and max slope will be reported at the centroid of each approximately equilateral triangular planar surface when there are sufficient beam data. Since the height of the triangle is the beam spacing or approximately 3 km, the length of the side is 2h/Sqrt(3) ~ 3.47 km, as described in Section 3.4.
Begin this calculation at the first instance of a reference photon on the center strong beam that satisfies the following conditions: 1) an outside strong beams exists over the water body 2) the crossing length ***iw_bdy_xlen*** of each is at least 3.5 km. 3) there are at least ***n_Seg_avg_plan*** heights reported within ***max_gseg_search*** geosegments on each side of the reference photon that has satisfied the above criteria. Note the location of this identified reference photon as one vertex of a triangle (***vert1a_lat, vert1a_lon***). If there is not sufficient coverage of a lake by multiple beams in this configuration, no multi-beam products will be reported.

At the first instance satisfied by the above criteria along a center strong beam, test one outside strong beam along a perpendicular, noting the reference photon of the equivalent geosegment on the other beam. Calculate the distance between the two index photons using the ph_dist_across, noted as perp1_dist. From the reference photon location on the adjacent beam, measure one half of the distance perp1_dist along that beam in each direction and note the reference photons of the geosegment that were landed in as the two other vertices of the triangle to be used in the planar calculation as (***vert1b_lat, vert1b_lon***) and (***vert1c_lat, vert1c_lon***). The direction of travel is the coordinate subset as "c." These two points, along with the original points (***vert1a_lat, vert1a_lon***) on the center beam are used to define the triangle. The height at each of these locations is defined for each as the weighted average (incorporating the reported distance from the triangle vertex) of the ***n_seg_avg_plan*** reported short segment heights ***H_unit_adj*** within ***max_gseg_search*** geosegments on each side of a given vertex point. Once the heights are known in three dimensional space, calculate the ***aspect*** and ***max_slope*** *of* the shape and report at (***plan_lat, plan_long***) at the centroid of the shape. Repeat for the other outside strong beam, if it exists, beginning the calculation again with the same point on the center beam. If there are not sufficient heights reported on the outside strong beam, move to the next geosegment on the center beam and start the testing of a new triangle construction.

After successfully constructing a triangle and calculating results, from vertex "c," create the next triangle with that location as one of two triangle vertices on the adjacent beam with a single vertex on the center beam. Then the process is repeated with a triangle once again with two vertices on the center beam and one on the adjacent. Create the next shape along track by advancing 3.5 km along the center beam from (***vert1a_lat, vert1a_lon***). Calculate a moving average of the ***n_Seg_avg_plan*** short segment heights ***H_unit_adj*** on either side of that point and repeat the creation of the same shape and execute the corresponding calculations of the planar characteristics.

Each calculated slope and aspect will be assigned a reporting location as (lat,lon) ***plan_lat*** and ***plan_lon*** at the centroid of the plane.

C) Error analysis and data quality
See description in Section 4.8. Based on calculations done previously in the algorithm, a number of quality flags will be created and provided in the output table.

QF_IWP(S_seg1ID) – describes the level of processing the inland water algorithm was able to perform on each short segment based on the data available, ranging from 7 to 1.
= 7 if ***L_sub_count*** > 0 (at least 30 short segments)
= 6 if ***L_sub_count*** = 0 and ***L_surf_count*** > 0 (10 to 29 short segments)
= 5 if ***L_surf_count*** =0 and ***S_seg1_count*** = 8-9 (8-9 short segments, be they the whole of the available crossing or the remainder after long/surface segment assignment)
= 4 if ***L_surf_count*** =0 and ***S_seg1_count*** =6-7 (6-7 short segments, be they the whole of the available crossing or the remainder after long/surface segment assignment)
= 3 if ***L_surf_count*** =0 and ***S_seg1_count*** =3-5 (3-5 short segments, be they the whole of the available crossing or the remainder after long/surface segment assignment)
= 2 if ***L_surf_count*** =0 and ***S_seg1_count*** <= 2 (2 short segments, be they the whole of the available crossing or the remainder after long/surface segment assignment)
= 1 if ***L_surf_count*** =0 and ***S_seg1_count*** <= 1 (1 short segment, be it the whole of the available crossing or the remainder after long/surface segment assignment)

min_sseg_threshold = 5

QF_Cloud – passed through quality flag from ATL09 (zero to 5)

QF_Bckgrd(S_seg1ID) – describes the degree of background photons present in each short segment, based on the background removed during long segment analysis.
= 0 if ***bckgrd_dnsty_50sht_bin_Sseg*** <= ***bckgrd_dnsty_threshold1***
= 1 if ***bckgrd_dnsty_threshold1*** > ***bckgrd_dnsty_50sht_bin_Sseg*** <= ***bckgrd_flag_threshold2***
= 2 if ***bckgrd_dnsty_threshold2*** > ***bckgrd_dnsty_50sht_bin_Sseg*** <= ***bckgrd_dnsty_threshold3***
= 3 if ***bckgrd_dnsty_threshold3*** > ***bckgrd_dnsty_50sht_bin_Sseg*** <= ***bckgrd_dnsty_threshold4***
= 4 if ***bckgrd_dnsty_threshold4*** > ***bckgrd_dnsty_50sht_bin_Sseg*** <= ***bckgrd_dnsty_threshold5***
= 5 if ***bckgrd_dnsty_threshold5*** > ***bckgrd_dnsty_50sht_bin_Sseg*** <= ***bckgrd_dnsty_threshold6***
= 6 if ***bckgrd_dnsty_50sht_bin*** > ***bckgrd_dnsty_threshold6***

bckgrd_dnsty_threshold1 = 0.001 (counts per bin per Sseg)
bckgrd_dnsty_threshold2 = 0.010 (counts per bin per Sseg)
bckgrd_dnsty_threshold3 = 0.050 (counts per bin per Sseg)
bckgrd_dnsty_threshold4 = 0.100 (counts per bin per Sseg)
bckgrd_dnsty_threshold5 = 0.300 (counts per bin per Sseg)
bckgrd_dnsty_threshold6 = 0.500 (counts per bin per Sseg)

QF_Ice(S_seg1ID) – describes the likelihood of ice on the water surface short segment.
= 0 if ***QF_Bckgrd*** <= 2
= 1 if 2 < ***QF_Bckgrd*** <= 4
= 2 if 4 < ***QF_Bckgrd***
= 3 if 4 < ***QF_Bckgrd*** and ***QF_Cloud*** > ***cloud_threshold1***

cloud_threshold1 = 4

QF_Subsurf_Anomaly
= 1 = Subsurface anomaly due to bottom likely
= 2 = Subsurface signal may indicate bottom or other anomaly
= 3 = Possible subsurface anomaly
= 999 = No subsurface anomaly detected

QF_Ht_Adj
= -4 if ***H_unit_adj*** **<** -0.20 (m)
= -3 if -0.20 ≤ ***H_unit_adj*** < -0.10
= -2 if -0.10 ≤ ***H_unit_adj*** < -0.05
= -1 if -0.05 ≤ ***H_unit_adj*** < -0.01
= 0 if -0.01 ≤ ***H_unit_adj*** < 0.01
= 1 if 0.01 ≤ ***H_unit_adj*** < 0.05
= 2 if 0.05 ≤ ***H_unit_adj*** < 0.10

= 3 if 0.10 ≤ ***H_unit_adj*** < 0.20
= 4 if 0.20 ≤ ***H_unit_adj***
= 5 if ***H_unit_adj*** is invalid

QF_Bias_Fit
= -3 when ***H_bias_fit*** < -0.10 (m)
= -2 when -0.10 ≤ ***H_bias_fit*** < -0.05
= -1 when -0.05 ≤ ***H_bias_fit*** < -0.01
= 0 if -0.01 ≤ ***H_bias_fit*** < 0.01
= 1 if 0.01 ≤ ***H_bias_fit*** < 0.05
= 2 if 0.05 ≤ ***H_bias_fit*** < 0.10
= 3 if 0.10 ≤ ***H_bias_fit***
= 4 if _***H_bias_fit*** is invalid

QF_Bias_EM
= -3 when ***H_bias_EM*** < -0.10 (m)
= -2 when -0.10 ≤ ***H_bias_EM*** < -0.05
= -1 when -0.05 ≤ ***H_bias_EM*** < -0.01
= 0 if -0.01 ≤ ***H_bias_EM*** < 0.01
= 1 if 0.01 ≤ ***H_bias_EM*** < 0.05
= 2 if 0.05 ≤ ***H_bias_EM*** < 0.10
= 3 if 0.10 ≤ ***H_bias_EM***
= 4 if _***H_bias_EM*** is invalid

QF_Spec_Width
= 0 if ***spec_width*** < 0.5
= 1 if ***spec_width*** ≥ 0.5

QF_Sseg_Length
= 0 if ***sseg_length*** < 50 (meters)
= 1 if 50 ≤ ***sseg_length*** < 150 (meters)
= 2 if 150 ≤ ***sseg_length*** < 300 (meters)
= 3 if 300 ≤ ***sseg_length***

QF_Lseg_Length
= 0 if ***Lseg_length*** < 500 (meters)
= 1 if 50 ≤ ***Lseg_length*** < 1500 (meters)
= 2 if 150 ≤ ***Lseg_length*** < 3000 (meters)
= 3 if 3000 ≤ ***Lseg_length***

QF_stdev_lseg
= 0 if ***detrend_sigma2*** < 0.5 (meters)
= 1 if 0.5 ≤ ***detrend_sigma2*** < 1.5 (meters)
= 2 if 1.5 ≤ ***detrend_sigma2*** < 2.5 (meters)
= 3 if 2.5 ≤ ***detrend_sigma2*** < 3.5 (meters)
= 4 if 3.5 ≤ ***detrend_sigma2*** < 4.5 (meters)
= 5 if 4.5 ≤ ***detrend_sigma2*** < 5.5 (meters)
= 6 if 5.5 ≤ ***detrend_sigma2*** < 6.5 (meters)
= 7 if 6.5 ≤ ***detrend_sigma2*** < 7.5 (meters)
= 8 if 7.5 ≤ ***detrend_sigma2*** < 8.5 (meters)
= 9 if 8.5 ≤ ***detrend_sigma2***

For short transects (where ***detrend_sigma2*** is not calculated), apply the above flag based on the value of ***L_surf_inc_stdev2*** instead.

QF_stdev_vlseg
= 0 if ***detrend_sigma2_Lsub*** < 0.5 (meters)
= 1 if 0.5 ≤ ***detrend_sigma2_Lsub*** < 1.5 (meters)
= 2 if 1.5 ≤ ***detrend_sigma2_Lsub*** < 2.5 (meters)
= 3 if 2.5 ≤ ***detrend_sigma2_Lsub*** < 3.5 (meters)
= 4 if 3.5 ≤ ***detrend_sigma2_Lsub*** < 4.5 (meters)
= 5 if 4.5 ≤ ***detrend_sigma2_Lsub*** < 5.5 (meters)
= 6 if 5.5 ≤ ***detrend_sigma2_Lsub*** < 6.5 (meters)
= 7 if 6.5 ≤ ***detrend_sigma2_Lsub*** < 7.5 (meters)
= 8 if 7.5 ≤ ***detrend_sigma2_Lsub*** < 8.5 (meters)
= 9 if 8.5 ≤ ***detrend_sigma2_Lsub***

Estimate the angles relevant to each reported short segment by averaging the values for all photons where the signal threshold is met. This will produce ***sseg_mean_atlas_azm***, ***sseg_mean_atlas_zen***, ***sseg_mean_solar_azm***, and ***sseg_mean_solar_zen*** for use in bias calculation.

5.4 ATL13 Inland Surface Water Output Variables

Table 5-4 ATL13 Along Track (Short Segment) Output Parameters (/gtx/)

Name	Units	Description	ATBD Source
ATL13_reference_id	N/A	Unique aggregate reference number for each shape in the ATL13 Inland Water Body Mask, where digit 1 = type, digit 2 = size, digit 3 = source, and digits 4-10 = shape id	5.3.1 (C)
inland_water_body_id	N/A	Identifying signature of an individual inland water body. Each body of water is represented by a unique numeric value.	5.3.1 (C)
inland_water_body_type	N/A	Type of Inland Water Body, where 1=Lake, 2=Known Reservoir, 3=(Reserved for future use), 4=Ephemeral Water, 5=River, 6=Estuary or Bay, 7=Coastal Water	5.3.1 (C)
inland_water_body_size	N/A	Size of Inland Water Body, where 1=Area>10,000 km^2, 2=10,000>A≥1,000, 3=1,000>A≥100, 4=100>A≥10, 5=10>A≥1, 6=1>A≥0.1, 7=0.01>A, 9 = Not Assigned	5.3.1 (C)

Name	Units	Description	ATBD Source
inland_water_body_source	N/A	Source of Inland Water Body shape, where: 1= HydroLAKES (Messager, M.L., Lehner, B., Grill, G., Nedeva, I., Schmitt, O. (2016): Estimating the volume and age of water stored in global lakes using a geo-statistical approach. Nature Communications: 13603. doi: 10.1038/ncomms13603. Data is available at www.hydrosheds.org.) 2= Global Lakes and Wetlands Database (Lehner, B. and Döll, P. (2004): Development and validation of a global database of lakes, reservoirs and wetlands. Journal of Hydrology 296/1-4: 1-22.) 3= Named Marine Water Bodies (ESRI http://mappingcenter.esri.com/index.cfm?fa=arcgisResources.gisData) 4=GSHHG Shoreline (Wessel, P., and W. H. F. Smith, A Global Self-consistent, Hierarchical, High-resolution Shoreline Database, *J. Geophys. Res., 101*, 8741-8743, 1996) 5=Global River Widths from Landsat (Allen and Pavelsky (2018) Global Extent of Rivers and Streams. *Science*. https://doi.org/10.1126/science.aat0636), 6=Reserved, 7=Reserved, 8=Reserved, 9=Reserved	5.3.1 (C)
iw_bdy_region	N/A	ATL13-created shapefile representing relevant bodies of water over which to implement the ATL13 water surface finding algorithm only within a region of processing interest	5.3.1 (A)
ht_water_surf	meters	Water surface height, reported for each short segment (default length = approximately 100 signal photons) with reference to WGS84 ellipsoid	5.3.5 (A)
segment_lat	degrees	Latitude of reporting location for all short segment statistics	5.3.5 (A)
segment_lon	degrees	Longitude of reporting location for all short segment statistics.	5.3.5 (A)
segment_delta_time	seconds	Time of reporting for all short segment statistics.	5.3.5 (A)
segment_geoid	meters	Applicable geoid value at reporting location for all short segment statistics.	5.3.5 (A)

Name	Units	Description	ATBD Source
sseg_mean_lat	degrees	Mean latitude of the signal-qualified photons in a short segment.	5.3.5 (A)
sseg_mean_lon	degrees	Mean longitude of the signal-qualified photons in a short segment.	5.3.5 (A)
sseg_mean_time	seconds	Mean time of the signal-qualified photons in a short segment.	5.3.5 (A)
segment_dac	meters	Dynamic atmospheric correction (DAC) includes inverted barometer (IB) effect (±5 cm). Although available at short segment rate for all water body types, value is provide mainly for transitional tidal and coastal water (types 6 and 7) and the largest lakes of Type 1 (~> 10,000 km^2) for user's discretion.	5.3.5 (A)
segment_tide_ocean	meters	Ocean tides including diurnal and semi-diurnal (harmonic analysis (±4 m). Although available at short segment rate for all water body types, value is provide mainly for transitional tidal and coastal water (types 6 and 7) and the largest lakes of Type 1 (~> 10,000 km^2) for user's discretion.	5.3.5 (A)
segment_tide_equillibrium	meters	Long period equilibrium tide self-consistent with ocean tide model (± 0.04 m). Although available at short segment rate for all water body types, value is provide mainly for transitional tidal and coastal water (types 6 and 7) and the largest lakes of Type 1 (~> 10,000 km^2) for user's discretion.	5.3.5 (A)
subsurface_attenuation	m^{-1}	Subsurface attenuation coefficient, reported per long segment (default length = 10 short segments = approximately 1000 signal photons).	5.3.4 (A)
segment_slope_trk_bdy	m/m	Along track water body surface slope, reported per short segment ID per water body.	5.3.5 (A)
ht_ortho	meters	Orthometric height EGM2008 converted from ellipsoidal height.	5.3.5 (A)
stdev_water_surf	meters	Derived standard deviation of water surface, calculated over long segments (when available) with result reported at each short segment location tag contained within.	5.3.3 (D)

Name	Units	Description	ATBD Source
sig_wv_ht	meters	Significant wave height (per short segment)	5.3.3 (D)
water_depth	meters	Depth from the mean water surface to detected bottom.	5.3.4 (A)
max_slope	N/A	Maximum slope of planar triangular surface between adjacent strong beams (deferred).	5.3.5 (B)
aspect	rad	Direction of slope of planar surface with respect to North between adjacent strong beams (deferred)	5.3.5 (B)
plan_lat	degrees	Latitude of reporting location for multi-beam planar statistics (deferred)	5.3.5 (B)
plan_lon	degrees	Longitude of reporting location for multi-beam planar statistics (deferred)	5.3.5 (B)
err_ht_water_surf	meters	Precision per 100 inland water photons: Eqn 4.29 (deferred)	4.9.1, 5.3.5 (C)
err_slope_trk	unitless	Error included in segment_slope_trk_local. (deferred)	5.3.5 (C)
QF_IwP	unitless	describes the level of processing the inland water algorithm was able to perform based on the data available, ranging from zero to 3.	4.8.1, 5.3.5 (C)
QF_Cloud	unitless	passed through quality flag from ATL09 (zero to 5)	4.8.2, 5.3.5 (C)
QF_Bckgrd	unitless	describes the degree of background photons present in each short segment. (Update wrt/ the sseg average bckgrd_count_flag)	4.8.3, 5.3.5 (C)
QF_Ice	unitless	Describes the likelihood of ice on the water surface short segment.	4.8.4, 5.3.5 (C)
QF_Subsurf_Anomaly	unitless	= 1 = Subsurface anomaly due to bottom likely = 2 = Subsurface signal may indicate bottom or other anomaly = 3 = Possible subsurface anomaly	5.3.4 (A)

Name	Units	Description	ATBD Source
QF_Bias_Fit	unitless	Set based on the value of the goodness of fit bias estimated as the difference between the centroid elevations of the observed surface water histogram and fitted integrated water surface model histogram. The flag values are set as follows: = -3 if H_bias_fit < -0.10 (m); -2 if -0.10 <= H_bias_fit < -0.05;-1 when -0.05 <= H_bias_fit < -0.01; 0 if -0.01 <= H_bias_fit < 0.01 (m); 1 if 0.01 <= H_bias_fit < 0.05; 2 if 0.05 < H_bias_fit < 0.10; 3 if 0.10 <= H_bias_fit; 4 if H_bias_fit is invalid.	4.8.6
QF_Bias_EM	unitless	Set based on threshold checks for the estimated electromagnetic height bias. The flag is set as follows: -3 if H_bias_EM < -0.10 (m); -2 if -0.10 < H_bias_EM < -0.05; -1 if -0.05 <= H_bias_EM < -0.01; 0 if -0.01 <= H_bias_EM < 0.01 (m); 1 if 0.01 <= H_bias_EM < 0.05; 2 if 0.05 <= H_bias_EM < 0.10; 3 if 0.10 < H_bias_EM; 4 if H_bias_EM is invalid.	4.8.7
QF_Spec_Width	unitless	Spectral moments width flag, set as follows: 0 when spec_width is invalid; 1 when 0 <= spec_width <= 0.2; 2 when 0.2 < spec_width <= 0.3; 3 when 0.3 < spec_width <= 0.4; 4 when 0.4 < spec_width <= 0.5; 5 when 0.5 < spec_width <= 0.6; 6 when 0.6 < spec_width <= 0.7; 7 when 0.7 < spec_width <= 0.8; 8 when 0.8 < spec_width <= 0.9; 9 when 0.9 < spec_width.	4.8.8
QF_Sseg_Length	unitless	Length of short segments flag, set as follows: 0 if sseg_length < 10 (meters); 1 if 10 <= sseg_length < 20 (meters); 2 if 20 <= sseg_length < 30 (meters); 3 if 30 <= sseg_length < 50 (meters); 4 if 50 <= sseg_length < 75 (meters); 5 if 75 <= sseg_length < 100 (meters); 6 if 100 <= sseg_length < 150 (meters); 7 if 150 <= sseg_length < 200 (meters); 8 if 200 <= sseg_length < 300 (meters); 9 if 300 <= sseg_length.	4.8.9

Name	Units	Description	ATBD Source
QF_Lseg_Length	unitless	The Long Segment Length flag, set based on the length of the long segment. The flag is set as follows: 0 if Lseg_length < 500 (meters); 1 if 50 <= Lseg_length < 1500 (meters); 2 if 150 <= Lseg_length < 3000 (meters); 3 if 3000 <= Lseg_length	4.8.10
met_wind10_atl09	m/s	Wind speed magnitude at 10m height from ATL09 input.	5.3.5 (A)
met_wind10_atl13	m/s	Wind speed at 10m height, based on derived water surface wave height.	5.3.5 (A)
met_ts_atl09	K	Surface (skin) temperature from ATL09	5.3.5 (A)
snow_ice_atl09	unitless	NOAA snow/ice flag scaled by ATL09 (0=ice-free water, 1=snow-free land, 2=snow, 3=ice)	5.3.5 (A)
cloud_flag_asr_atl09	unitless	Cloud probability from ASR	5.3.5 (A)
cloud_flag_atm_atl09	unitless	Cloud flag from backscatter profile	5.3.5 (A)
layer_flag_atl09	unitless	Consolidated cloud flag	5.3.5 (A)
segment_fpb_correction	meters	First photon bias correction. May be applied at user discretion by subtracting from mean height products ht_ortho and ht_water_surf.	5.3.5 (A)
transect_ID	unitless	Transect within a water body to which the short segment rate output belongs.	5.3.2 (C)
sseg_start_lat	degrees	Latitude at which the short segment begins. May be a signal or non-signal photon.	5.3.2 (C)
sseg_start_lon	degrees	Longitude at which the short segment begins. May be a signal or non-signal photon.	5.3.2 (C)
sseg_end_lat	degrees	Latitude at which the short segment ends. May be a signal or non-signal photon.	5.3.2 (C)
sseg_end_lon	degrees	Longitude at which the short segment ends. May be a signal or non-signal photon.	5.3.2 (C)

Name	Units	Description	ATBD Source
segment_full_sat_fract	unitless	The fraction of pulses within the short segment determined to be fully saturated based on ATL03 geosegment rate input.	5.3.2 (E)
segment_near_sat_fract	unitless	The fraction of pulses within the short segment determined to be nearly saturated based on ATL03 geosegment rate input.	5.3.2 (E)
segment_azimuth	radians	The direction, eastwards from north, of the laser beam vector as seen by an observer at the laser ground spot viewing toward the spacecraft (i.e., the vector from the ground to the spacecraft). When the spacecraft is precisely at the geodetic zenith, the value will be 99999 degrees.	5.3.5 (A)
QF_ht_adj	unitless	Flag representing the range of height, defined in 5.3.5 (C), which has been added to the apparent surface height due to frame of reference scaling during deconvolution analysis.	5.3.5 (C)
segment_apparent_ht	meters	Apparent height of the short segment, before adjustments are made by the algorithm, based on an average of heights within a designated range of the short segment mode.	5.3.5 (A)
segment_bias_EM	meters	Electromagnetic bias. *(Has been applied to ht_ortho and _ht_water_surf products)*	5.3.5 (A)
segment_bias_fit	meters	Bias contribution from goodness of observation/system response fit. *(Has been applied to ht_ortho and _ht_water_surf products)*	5.3.5 (A)
segment_fpb_correction	meters	First photon bias correction. *(Has been applied to ht_ortho and ht_water_surf products)*	5.3.5 (A)
segment_dem_ht	m	DEM height reported at the short segment rate.	5.3.5 (A)
segment_dem_source	unit-less	Flag equal to the source of the selected photon of prioritized source where: 0 = None; 1 = Arctic; 2 = MSS; 3 = Global; 4 = Antarctic.	5.3.5 (A)
segment_geoid_free2mean	meters	Value to convert segment geoid heights from the mean-tide system to the tide-free system. Subtract this value from mean-tide system segment_geoid (on ATL13) to get geoid heights in the tide-free system. Applicable value at reporting location for all short segment statistics.	5.3.5 (A)

Name	Units	Description	ATBD Source
segment_tide_earth_free2mean	meters	Segment rate value to convert solid earth tide from the tide-free system that was applied in ATL03 to photon heights to the ht_water_surf to the mean-tide system. Subtract value from ht_water_surf to reference it in the mean-tide system. Applicable value at reporting location for all short segment statistics.	5.3.5 (A)
segment_quality	unitless	Four-element array of describing, for each short segment n, the count of photons qualifying in each quality group. (n,1) = nominal, (n,2) = possible afterpulse, (n,3) = possible impulse response effect, (n,4) = possible TEP	5.3.5 (A)
segment_id_beg	unitless	First ATL03 segment_id associated with the photons within this inland water segment.	5.3.5 (A)
segment_id_end	unitless	Last ATL03 segment_id associated with the photons within this inland water segment.	5.3.5 (A)
segment_podppd_flag	unitless	Composite POD/PPD flag that indicates the quality of input geolocation products for the utilized ATL03 segments on an ATL13 short segment output basis. A non-zero value may indicate that geolocation solutions are degraded or that ATLAS is within a calibration scan period (CAL). The ATL03 sigma values should indicate the degree of uncertainty associated with the degradation. Possible non-CAL values are: 0=NOMINAL; 1=POD_DEGRADE; 2=PPD_DEGRADE; 3=PODPPD_DEGRADE; possible CAL values are: 4=CAL_NOMINAL; 5=CAL_POD_DEGRADE; 6=CAL_PPD_DEGRADE; 7=CAL_PODPPD_DEGRADE;	4.5.5.1, 4.8.1
segment_ref_elev	radians	Elevation of the unit pointing vector for the reference photon in the local ENU frame in radians. The angle is measured from east-north plane and positive towards up.	5.3.5 (A)
bottom_lat	degrees	Latitude of actual bottom location, based on the apparent bottom ***sseg_mean_lat*** / ***sseg_mean_lon*** location corrected for refraction effects.	5.3.5 (A)

Name	Units	Description	ATBD Source
bottom_lon	degrees	Longitude of actual bottom location, based on the apparent bottom ***sseg_mean_lat*** / ***sseg_mean_lon*** location corrected for refraction effects.	5.3.5 (A)
sseg_sig_ph_cnt	N/A	Count of signal photons in short segment, full or partial.	5.3.1 (C)
QF_stdev_lseg	N/A	Quality flag indicating the magnitude of standard deviation (SD) of observed detrended heights of the long segment to which the short segment belongs, where 0: SD < 0.5 (meters), 1: 0.5 ≤ SD < 1.5, 2: 1.5 ≤ SD < 2.5, 3: 2.5 ≤ SD < 3.5, 4: 3.5 ≤ SD < 4.5, 5: 4.5 ≤ SD < 5.5, 6: 5.5 ≤ SD < 6.5, 7: 6.5 ≤ SD < 7.5, 8: 7.5 ≤ SD < 8.5, 9: 8.5 ≤ SD. It is recommended that a user consider this flag in conjunction with the water body type and size to best determine if the observed surface standard deviation is reasonable or whether results should be considered questionable.	5.3.5 (C)
subsurface_backscat_ampltd	unitless	Subsurface backscatter amplitude, described in section 4.5.3, reported per long segment (default length = 10 short segments = approximately 1000 signal photons).	5.3.4 (A)

Name	Units	Description	ATBD Source
QF_subsurface_attenuation	unitless	Quality flag indicating whether or not the reported subsurface attenuation was constrained during deconvolution by the minimum (initial) limit in the possible range (QF=-1), the maximum limit in the possible range (QF = 1), or was allowed to settle on a solution within the possible range (QF=0). For analysis prior to deconvolution of the subsurface attenuation fit to the observations, the flag indicates whether the value determined by attempting to fit the observations was below (QF= -2), above (QF= 2), or within (QF=0) the possible range of expected values. When the default value for subsurface attenuation is chosen due to any condition other than those defined by an existing quality flag, QF=invalid.	5.3.4 (A)
QF_ subsurface_backscat_ampltd	unitless	Quality flag indicating whether or not the reported subsurface backscatter amplitude was constrained during deconvolution by the minimum limit in the possible range (QF=-1), the maximum limit in the possible range (QF = 1), or was allowed to settle on a solution within the possible range (QF=0). For analysis prior to deconvolution of the backscatter amplitude fit to the observations, the flag indicates whether the value determined by attempting to fit the observations was below (QF= -2), above (QF= 2), or within (QF=0) the possible range of expected values. When the default value for backscatter amplitude is chosen due to any condition other than those defined by an existing quality flag, QF=invalid.	5.3.4 (A)

Name	Units	Description	ATBD Source
QF_stdev_vlseg	N/A	Quality flag indicating the magnitude of standard deviation (SD) of observed detrended heights of the very long segment to which the short segment belongs, where 0: SD < 0.5 (meters), 1: 0.5 ≤ SD < 1.5, 2: 1.5 ≤ SD < 2.5, 3: 2.5 ≤ SD < 3.5, 4: 3.5 ≤ SD < 4.5, 5: 4.5 ≤ SD < 5.5, 6: 5.5 ≤ SD < 6.5, 7: 6.5 ≤ SD < 7.5, 8: 7.5 ≤ SD < 8.5, 9: 8.5 ≤ SD. It is recommended that a user consider this flag in conjunction with the water body type and size to best determine if the observed surface standard deviation is reasonable or whether results should be considered questionable.	5.3.5 (C)
RGT	unitless	The reference ground track (RGT) is the track on the Earth at which a specified unit vector within the observatory is pointed. Under nominal operating conditions, there will be no data collected along the RGT, as the RGT is spanned by GT2L and GT2R. During slews or off-pointing, it is possible that ground tracks may intersect the RGT. The ICESat-2 mission has 1,387 RGTs.	5.3.1 (B)
cycle_number	unitless	Tracks the number of 91-day cycles in the mission, beginning with 01. A unique orbit number can be determined by subtracting 1 from the cycle_number, multiplying by 1,387 and adding the RGT value.	5.3.1 (B)

5.5 Anomalous Along Track (Short Segment) Output Parameters

Table 5-5 Anomalous Short Segment Output Parameters (/gtx/anom_ssegs/)

Name	**Units**	**Description**	**ATBD Source**
ATL13_reference_id	N/A	Unique aggregate reference number for each shape in the ATL13 Inland Water Body Mask, where digit 1 = type, digit 2 = size, digit 3 = source, and digits 4-10 = shape id	5.3.1 (C)
transect_ID	N/A	Transect within a water body to which the short segment rate output belongs.	5.3.1 (C)
anom_sseg_length	m	Length of the short segment, based on end points computed by the average of ***sseg_endpoint_avg_n*** signal photons.	5.3.1 (C)
anom_sseg_time	sec	Time of the short segment (mean of signal class ≥2 ph time)	5.3.1 (C)
anom_sseg_lat	degrees	Latitude of the short segment (mean of signal class ≥2 ph Lats)	5.3.1 (C)
anom_sseg_lon	degrees	Longitude of the short segment (mean of signal class ≥2 ph Lons)	5.3.1 (C)
coarse_transect_ht	m	Coarse water height of transect.	5.3.1 (C)
anom_sseg_mode	m	Height of anomalous short segment as determined by histogram bin mode	5.3.1 (C)
anom_sseg_ht_delta	m	Height difference between anom_sseg_mode of the anomalous short segment and the transect coarse_transect_ht	5.3.1 (C)
anom_sseg_mean_ht_ortho	m	Orthometric height of anomalous short segment as determined by the mean of photon orthometric heights in the anomalous short segment with signal classification ≥2	5.3.1 (C)
anom_sseg_stdev	m	Standard deviation of anomalous short segment photon height in the anomalous short segment with signal classification ≥2	5.3.1 (C)
anom_sseg_start_lat	degrees	Start latitude of the anomalous short segment, based on the average latitude of the first ***sseg_endpoint_avg_n*** signal photons in the segment.	5.3.1 (C)

Name	Units	Description	ATBD Source
anom_sseg_start_lon	degrees	Start longitude of the anomalous short segment, based on the average longitude of the first ***sseg_endpoint_avg_n*** signal photons in the segment.	5.3.1 (C)
anom_sseg_end_lat	degrees	End latitude of the anomalous short segment, based on the average latitude of the last ***sseg_endpoint_avg_n*** signal photons in the segment.	5.3.1 (C)
anom_sseg_end_lon	degrees	End longitude of the anomalous short segment, based on the average longitude of the last ***sseg_endpoint_avg_n*** signal photons in the segment.	5.3.1 (C)
anom_sseg_trigger_flag	N/A	Nine element array describing justification for short segment classification as anomalous, where for each element 0 = not triggered as anomalous and 1 = triggered as anomalous due to any of the following causes: [element 1=coarse ht difference, element 2=abnormal length, element 3= histogram mode spread, element 4=histogram mode count, element 5=histogram mode intensity, element 6=invalid long segment, element 7=shore buffer designation, element 8=insufficient signal phs, element 9 = transect coarse water height unavailable against which to test short segment height]	5.3.1 (C)
anom_sseg_quality	N/A	Four-element array of describing, for each anomalous short segment n, the count of photons qualifying in each quality group. (n,1) = nominal, (n,2) = possible afterpulse, (n,3) = possible impulse response effect, (n,4) = possible TEP	5.3.1 (C)
anom_sseg_sig_ph_cnt	N/A	Count of signal photons in anom short segment, full or partial.	5.3.1 (C)
RGT	unitless	The reference ground track (RGT) is the track on the Earth at which a specified unit vector within the observatory is pointed. Under nominal operating conditions, there will be no data collected along the RGT, as the RGT is spanned by GT2L and GT2R. During slews or off-pointing, it is possible that ground tracks may intersect the RGT. The ICESat-2 mission has 1,387 RGTs.	5.3.1 (B)

Name	Units	Description	ATBD Source
cycle_number	unitless	Tracks the number of 91-day cycles in the mission, beginning with 01. A unique orbit number can be determined by subtracting 1 from the cycle_number, multiplying by 1,387 and adding the RGT value.	5.3.1 (B)

6.0 PRE-LAUNCH DATA PRODUCT RESULTS USING HIGH ELEVATION AIRBORNE PROTOTYPE ATLAS OBSERVATIONS

6.1 Typical ATL13 examples using MABEL

Given that MABEL's sampling design scales well with ATLAS, it has proven to be an important instrument for testing the ATL13 algorithm. This section summarizes the results of three diverse applications of ATL13 to the high elevation MABEL photon counting data (Jasinski et al., 2016). The cases include one estuary, the Chesapeake Bay; one coastal region, the Atlantic Ocean at Virginia Beach; and one reservoir, Lake Mead including bathymetry identification. Cases also differ by time of overflight and turbidity.

6.1.1 **Inland Estuary – Chesapeake Bay**

The Chesapeake Bay transects is shown in Figure 6.1. The case represents a mid-day observation on September 25, 2013 with moderate wind and turbidity with mostly clear sky conditions. The transect consists of a one minute acquisition along an 8 km reaches in the middle of the bay near NOAA's Gooses Reef buoy. There were no land crossings and water depth was greater than 10 m.

Plots of the georeferenced MABEL photon cloud returns from the atmosphere through the water column with respect to the WGS84 Geodetic height are shown in Figure 6.2.
.

Figure 6-1 Location map of high altitude MABEL flights over Chesapeake Bay in 2013 near Gooses Reef buoy. Base map from Google Earth

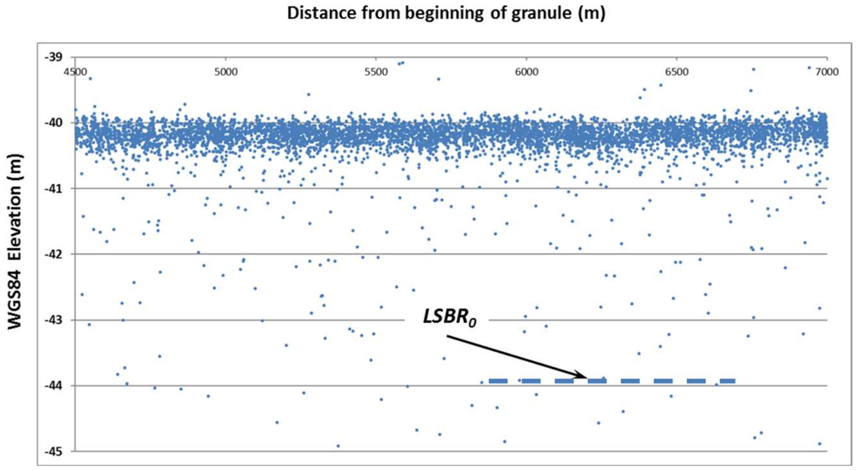

Figure 6-2 MABEL 2013 data, Chesapeake Bay Near Gooses Reef buoy. (Jasinski et al., 2016)

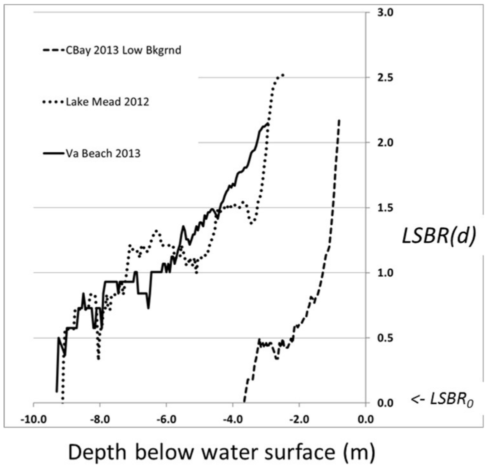

Figure 6-3 Signal to background ratio profiles versus depth, LSBR(d), for cases presented in this study, expressed in Log_{10} base. Also indicated is the $LSBR_0$ threshold level. (Jasinski et al., 2016).

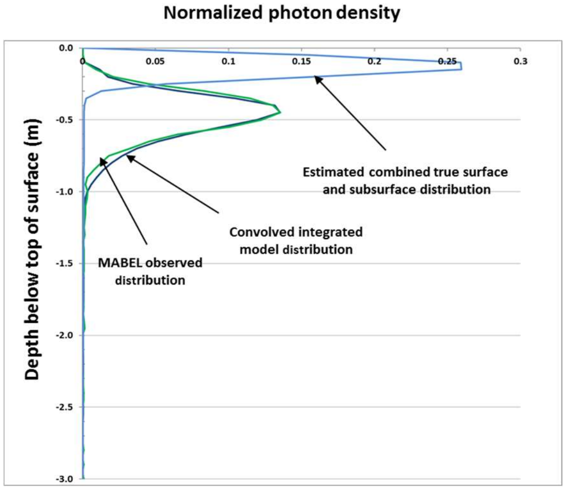

Figure 6-4 Histograms of the components of the best fit convolution model

for Chesapeake Bay case (Jasinski et al., 2016)

6.1.2 Near Shore – Atlantic Ocean at Virginia Beach

This case is an East-West transect extending from the Atlantic coast at Virginia Beach, just south of the mouth of the Chesapeake, eastward into the Atlantic on September 19, 2013 at 22:30 UTC (late afternoon local time). Figure 6.5 shows the transect location map which is situated just south of the mouth of the Chesapeake Bay. A 20 second segment of about 2000 MABEL photons is plotted in Figure 6.6. For this date, sky conditions were mostly clear, and wind from the East at 4.2 m/s. One additional feature not seen in the Chesapeake Bay cases is evidence of some wave structure throughout the transect. This is attributed to the MABEL flight being aligned nearly parallel to the wind direction. Histograms of the MABEL and integrated model are shown in Figure 6.7

Figure 6-5 Location map of high altitude MABEL flights over Site 2, Atlantic Ocean near Virginia Beach. Base map from Google Earth.

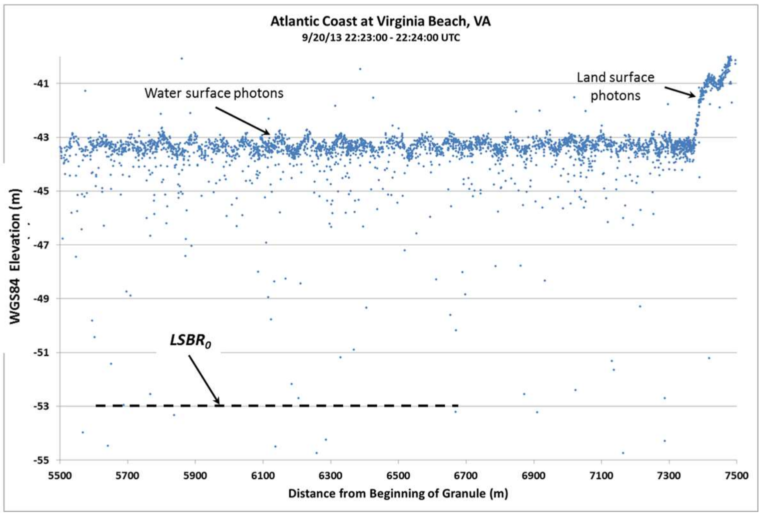

Figure 6-6 Along track profile of MABEL observed photons for Site 2, Atlantic Coast at Virginia Beach. $LSBR_0$ depth indicated at 9.3m below surface. (Jasinski et al., 2016).

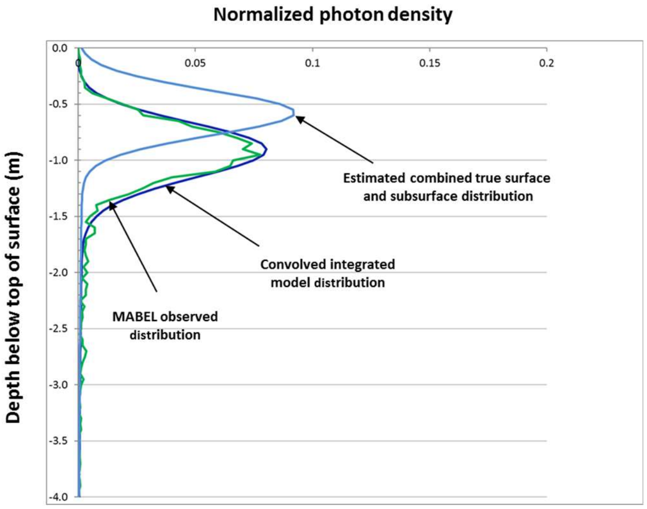

Figure 6-7 Histograms of components of the best fit convolution model for Virginia Beach case.

6.1.3 Reservoir – Lake Mead

This case represents a night flight over a relatively clear water body with turbidity equal to 1.6 NTU. The MABEL overpass of February 24, 2012 transected the western portion of Lake Mead in a Southwest to Northeast direction as shown in Figure 6.8. The transect represents two granules of data, or about 2 minutes of acquisition covering about 24 km.

The corresponding plot of the MABEL photons are shown in Figure 12 with the Southwest corner of the lake is on the left. During the flight approximately 91,000 photons were recorded. Because of the nighttime and clear sky conditions, there was an extremely low background count of 0.00008 m^{-2}. The photon cloud data plot and the resulting histograms of the MABEL and model solution are shown in Figures 6-9 and 6-10, respectively.

Figure 6-8 Location map of high altitude MABEL flights over Lake Mead in 2012. Base map from Google Earth.

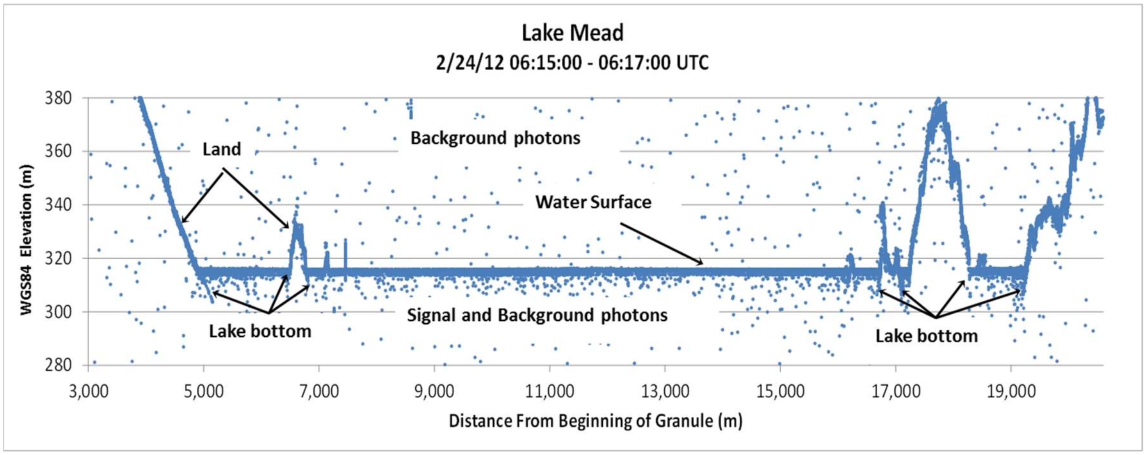

Figure 6-9 MABEL along track photon cloud retrieval from Lake Mead in 2012 (after Jasinski et al., 2016).

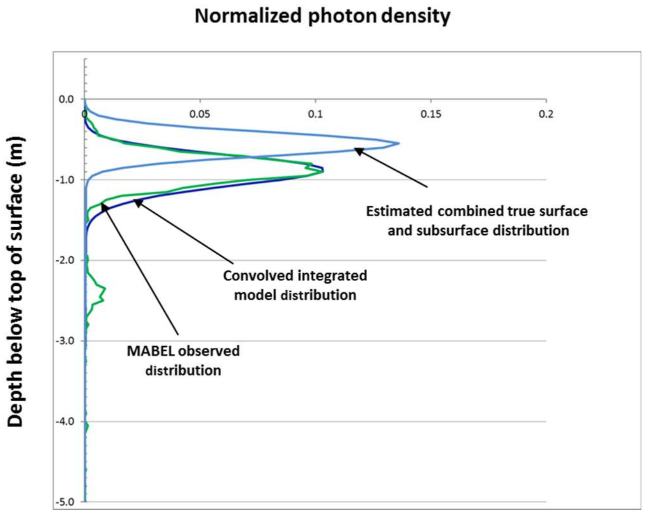

Figure 6-10 Histograms of components of the best fit convolution model for Lake Mead, 2012 case.

MABEL was designed as a high altitude prototype of the ICESat-2 ATLAS sensor, and thus the above results can be expected to be similar to those retrieved from ATLAS.

6.1.4 Bathymetry – Lake Mead

Unlike the previous cases, it was first shown that the bathymetry of Lake Mead is very apparent from MABEL photons in the vicinity of shorelines of many lake edges and islands (Jasinski et al., 2016). To view this more clearly, the southwest shore of Figure 6-9 is expanded in Figure 6-11 below. Prior to plotting, data were first processed to remove an instrument after pulse at about 1.4 m depth. The apparent near-shore bottom of the lake is observed as an extension of the shoreline to a depth of nearly 9 m. True depth would be calculated after correcting for refraction and speed of light.

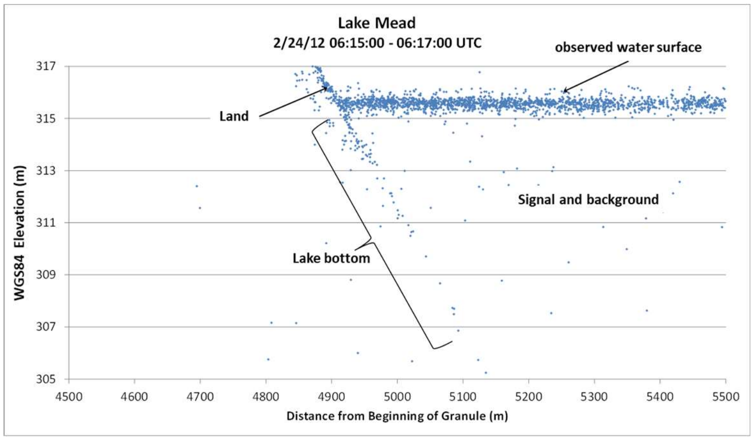

Figure 6-11 Bathymetry of Lake Mead. Expanded view of MABEL photon observations at land water crossing on the southwest shore. Results show penetration of the 532-nm channel into the water column and the presence of lake bottom to a depth of about 10 m.

7.0 REFERENCES

Allen, G.H. and T. M. Pavelsky, 2018: Global extent of rivers and streams. *Science* 361, 585–588. DOI: 10.1126/science.aat0636.

Allouis, T.; Bailly, J.-S.; Lesaignoux, A.; Feurer, D Assessing Water Surface Effects on LiDAR Measurements in very Shallow Rivers: A Theoretical Study Second Space for Hydrology Workshop - "Surface Water Storage and Runoff: Modeling, In-Situ data and Remote Sensing", Geneva (Switzerland), 12-14 November 2007.

Apel, J. R., 1994: An improved model of the ocean surface wave vector spectrum and its effects on radar backscatter. J. Geophys. Res., 99, 16 269–16 291.

ATL03 ATBD, Neumann et al.

Babin, M., and D. Stramski (2005). Variations in the mass-specific absorption coefficient of mineral particles suspended in water. *Limnology and Oceanography*, **49**, 756-767.

Barrick, D.E., Rough Surface Scattering Based on the Specular Point Theory, *IEEE Trans. Antenn. and Propagation*, vol AP-16, pp. 449-454, July 1968.

Barton. J and M. Jasinski, Sensitivity of Depth-Integrated Satellite Lidar to Subaqueous Scattering Remote Sens. 2011, 3, 1492-1515; doi:10.3390/rs3071492, July 2011.

Barton, J, and M. Jasinski (2009), Retrieval of inherent optical properties of turbid coastal waters using active and passive optical remote sensing, IEEE IGARSS, Cape Town, South Africa.

Bascom, W. 1964. Revised and updated edition, 1980. *Waves and Beaches.* Anchor Books, Anchor Press/Doubleday, Garden City, New York, 367 pp.

Bourassa, 1981.

Bourassa, M. A., D. M. Legler, and J. J. O'Brien, 1996: Comparison of ERS scatterometer winds and IMET observations. *Third Workshop on ERS Applications*, IFREMER, June, Brest, 27-42. Also http://coaps.fsu.edu/~bourassa/pubs/SWH_flux/SWH_flux.shtml

Bourassa, M. A., D. G. Vincent, W. L. Wood, 1999: A flux parameterization including the effects of capillary waves and sea state. J. Atmos. Sci., **56**, 1123-1139.

Birkett, C.M. and I.M. Mason, A new Global Lakes Database for a remote sensing programme studying climatically sensitive large lakes, J. Great Lakes Research, 21, No.3, pp.307-318., 1995.

Birkett, C.M., C. Reynolds, B. Beckley, and B. Doorn, From Research to Operations: The USDA Global Reservoir and Lake Monitor, Chapter 2 in 'Coastal Altimetry', Springer Publications, eds. S. Vignudelli, A.G. Kostianoy, P. Cipollini and J. Benveniste, Springer Publications, ISBN 978-3-642-12795-3, 2010.

Breon, F. M., and Henriot, N., Spaceborne observations of ocean glint reflectance and modeling of wave slope distributions, J. Geophys. Res., 111, C06005, doi: 10.1029/2005JC003343, 2006.

Bricaud, A. and A. Morel (1986). Light attenuation and scattering by phytoplanktonic cells: a theoretical modeling, *Applied Optics*, **25**, 571-580.
Buchheim, Oceanography, http://www.marinebiology.org/oceanography.htm.

Bufton, J. L., F. E. Hoge, and R. N. Swift (1983), Airborne measurements of laser backscatter from the ocean surface, Appl. Opt., 22, 2603–2618.

Bukata R P, Jerome J H , Kondratyev K Y and Pozdnyakov D V 1995 Optical properties and remote sensing of inland and coastal waters. CRC Press, 384pp.

Callaghan, A., G. de Leeuw, L. Cohen, and C. D. O'Dowd (2008), Relationship of oceanic whitecap coverage to wind speed and wind history, *Geophys. Res. Lett.*, *35*, L23609, doi:10.1029/2008GL036165.

Calmant, S., Seyler, F., & Cretaux, J. -F. (2008). Monitoring continental surface waters by satellite altimetry. Survey in Geophysics, 29, 247 −269, doi:10.1007/s10712-008-9051-1.

Caulliez, G*., and* C.-A. Guérin *(*2012*),* Higher-order statistical analysis of short wind wave fields*,* J. Geophys. Res.*,* 117*, C06002, doi:*10.1029/2011JC007854.

Churnside, J.H., Konstantin Naugolnykh and Richard D. Marchbanks
" Optical remote sensing of sound in the ocean ", *Proc. SPIE* 9111, Ocean Sensing and Monitoring VI, 91110T (May 23, 2014); doi:10.1117/12.2052930;

Churnside, J.H., V. T.Viatcheslav, and J. J. Wilson, "Oceanographic lidar attenuation coefficients and signal fluctuations measured from a ship in the Southern California Bight," Appl. Opt. 37, 3105--3111 (1998).

E. R. Cook*, R. D. D'Arrigo, M. E. Mann,* J. Clim. 15*,* 1754 *(*2002*).*

Cox, C. and Munk, W.: Measurement of the Roughness of the Sea Surface from Photographs of the Sun's Glitter, J. Opt. Soc.Am., 14, 838-850, 1954.

Cox and Munk, 1953

Dobson et al, 1989

Donelan, M., J. Hamilton, and W. H. Hui, 1985; Directional spectra of wind–generated waves. Philos. Trans. R. Soc. Lond., A 315, 509–562.

Dudis, J., (1986). Electromagnetic Bias of Airborne Off-Nadir Laser Backscatter From the Ocean, J. Geoph. Res., 91, C9, 10750-10752.

Elfouhaily, T., B. Chapron, K. Katsaros, and D. Vandemark (1997), A unified directional spectrum for long and short wind-driven waves, J. Geophys. Res., 102(C7), 15781–15796, doi:10.1029/97JC00467.

Exton RJ, Houghton WM, Esaias WE, Harriss RC, Farmer FH, White HH. "Laboratory analysis of techniques for remote sensing of estuarine parameters using laser excitation". Appl Opt. 1983 Jan 1;22(1):54-64.

Gerstner, F. V. 1802. Theory of waves. Abhandlungen der Koenigl, boehmischen Gesellschaft der Wissenschaften zu Prag.

Gordon, H.R. (1982), Interpretation of airborne oceanic lidar: effects of multiple scattering, *Appl. Opt.* 21, 2996-3001.

Guenther, Gary C. and Thomas, Robert W.L., 1984, Prediction and Correction of Propagation-Induced Depth Measurement Biases Plus Signal Attenuation and Beam Spreading for Airborne Laser Hydrography, NOAA Technical Report NOS 106 Charting and Geodetic Services Series CGS 2.

Guenther, G.C., "Airborne Laster Hydrography: System design and performance factors," NOS, NOAA, Rockville, MD, NOAA Prof. Paper Ser., Mar. 1985.

Guenther, G.C., A. G. Cunningham, P. E. LaRocque, and D. J. Reid, "Meeting the accuracy challenge in Airborne LiDAR Bathymetry," in Proc. EARSel, Dresden, Germany, 2000.

Haltrin, V. I. (2001). *Emperical Relationship Between Aerosol Scattering Phase Funcion and Optical Thickness of Atmosphere Above the Ocean*. Stennis Space Center, MS, CA: Naval Research Laboratory.

Harding, D., and M. J. Jasinski (2004), ICESat observations of inland surface water stage, slope, and extent: A new method for hydrologic monitoring, paper presented at AGU fall meeting, San Francisco, Calif.

Hargreaves, B.R., 2003. Water column optics and penetration of UVR. *UV effects in aquatic organisms and ecosystems 1*, pp. 59-108.

Hasselmann, K, et al., 1973: Measurements of wind-wave growth and swell decay during the Joint North Sea Wave Proj.ect (JONSWAP), Deutch. Hydrogr. Z. Suppl. A8, 12, 95 pp.

Hinzman, L. D., Bettez, N., Bolton, W. R., Chapin, F. S., Dyurgerov, M. B., Fastie, C. L., Griffith, B., Hollister, R. D., Hope, A., Huntington, H. P. et al. (2005). Evidence and implications of recent climate change in northern Alaska and other arctic regions. Clim. Chang. 72, 251-298.

Hu, Y., Stamnes, K., Vaughan, M., Pelon, J., Weimer, C., Wu, D., Cisewski, M., Sun, W., Yang, P., Lin, B., Omar, A., Flittner, D., Hostetler, C., Trepte, C., Winker, D., Gibson, G., and Santa-Maria, M.: Sea surface wind speed estimation from space-based lidar measurements, Atmos. Chem. Phys., 8, 3593-3601, doi:10.5194/acp-8-3593-2008, 2008.

Huang, N. E., 1981: An estimate of the influence of breaking waves on the dynamics of the upper ocean. In Wave Dynamics and Radio Probing of the Ocean Surface, eds O. W. Phillips and K. Hasselmann, Plenum Press, London, UK, 295-312.

Hwang, P.A. 2005: Wave number spectrum mean square slope of intermediate-scale ocean surface waves, J. Geoph Res., 110, C10029, doi:10.1029/2005JC003002.

ICESat-2 Project office, Personal communication.

IPCC, 2014

M. Jasinski, J. Stoll, H. Gao, and C. Parrish, " NASA's ICESat-2 Inland Water Height Data Product for Satellite Lidar Hydrology, American Geophysical Meeting Fall Meeting, TH45L, San Francisco, CA, December 12, 2010.

M. Jasinski, J. Stoll, D. Hancock, J. Robbins, J. Nattala, T. Pavelsky, J. Morrison, B. Jones, M. Ondrusek, C. Parrish, and the ICESat-2 Science Team, (2021). Algorithm Theoretical Basis Document (ATBD) for Inland Water Data Products, ATL13, Version 5, Release Date August 21, 2021, NASA Goddard Space Flight Center, Greenbelt, MD, 120 pp.
https://doi: 10.5067/RI5QTGTSVHRZ.
Also see, https://nsidc.org/sites/nsidc.org/files/technical-references/ICESat2_ATL13_ATBD_r005.pdf.

(Suggested citation when using ATL13 Inland Water data products from NSIDC):
M. Jasinski, J. Stoll, D. Hancock, J. Robbins, J. Nattala, T. Pavelsky, J. Morrison, B. Jones, M. Ondrusek, C. Parrish, and the ICESat-2 Science Team, 2021. *ATLAS/ICESat-2 L3A Along Track Inland Surface Water Data, Release 5*. [Indicate subset used]. Boulder, Colorado USA. NASA National Snow and Ice Data Center Distributed Active Archive Center.
DOI:10.5067/ATLAS/ATL13.005 (August 2021b).

Jasinski, M. F., J. D. Stoll, D. W. Hancock, J. W. Robbins, and J. Nattala. 2019. "ATLAS/ICESat-2 L3A Inland Water Surface Height Data Products, ATL13, Version 2." NASA National Snow and Ice Data Center Distributed Active Archive Center, Boulder CO, **Version 2**.
https://doi.org/10.5067/ATLAS/ATL13.002
https://nsidc.org/data/atl13/versions/2. (October, 2019b).

Jasinski, M. F., J. D. Stoll, D. W. Hancock, J. W. Robbins, and J. Nattala. 2019. "ATLAS/ICESat-2 L3A Inland Water Surface Height Data Product, ATL13, Version 1." *NASA National Snow and Ice Data Center Distributed Active Archive Center, Boulder CO*, 89 https://doi/10.5067/ATLAS/ATL13.001. (May 2019a).

Jasinski, M.; Stoll, J.; Cook, W.; Ondrusek, M.; Stengel, E., and Brunt, K., 2016. Inland and near-shore water profiles derived from the high-altitude Multiple Altimeter Beam Experimental Lidar (MABEL). *In*: Brock, J.C.;Gesch, D.B.; Parrish, C.E.; Rogers, J.N., and Wright, C.W. (eds.), *Advances in Topobathymetric Mapping, Models,and Applications*. *Journal of Coastal Research*, Special Issue, No. 76, pp. 44–55. Coconut Creek (Florida), ISSN0749-0208.

Jezek, K. C., D. K. Perovich, K. M. Golden, C. Luther, D. G. Barber, P. Gogineni, T. C. Grenfell, A. K. Jordan, C. D. Mobley, S. V. Nghiem, and R. G. Onstott, "A broad spectral, interdisciplinary investigation of the electromagnetic properties of sea ice", *IEEE Transactions on Geoscience and Remote Sensing*, vol. 36, no. 5, pp.1633 -1641, 1998.

Johnsen et al, 1994

Kahma, K.K., 1981, "A study of the growth of the wave spectrum with fetch", J. Phys. Oceanogr., 11, 1503-1515.

Kay, S.; Hedley, J.D.; Lavender, S. Sun Glint Correction of High and Low Spatial Resolution Images of Aquatic Scenes: a Review of Methods for Visible and Near-Infrared Wavelengths. *Remote Sens.* **2009**, *1*, 697-730.

Kay, S., John Hedley, Samantha Lavender, and Alex Nimmo-Smith, "Light transfer at the ocean surface modeled using high resolution sea surface realizations," Opt. Express 19, 6493-6504 (2011) http://www.opticsinfobase.org/oe/abstract.cfm?URI=oe-19-7-6493.

Kirk J T O, 1994, Light and photosynthesis in aquatic ecosystems. Cambridge University Press, Cambridge, 410 pp.

Kwok, R., G. F. Cunningham, S. S. Manizade, W. B. Krabill (2012), Arctic sea ice freeboard from IceBridge acquisitions in 2009: Estimates and comparisons with ICESat, J. Geophys. Res., 117, C02018, doi:10.1029/2011JC007654.

Kwok, R., T. Markus, J. Morison, S. P. Palm, T. A. Neumann, K. M. Brunt, W. B. Cook, D. W. Hancock, and G. F. Cunningham. (2014), Profiling sea ice with Multiple Altimeter Beam Experimental Lidar (MABEL), J. Atmos. Oceanic. Technol., in press..

Lake Access www.lakeaccess.org.

Lancaster, R. S.*,* J. D. Spinhirne*, and* S. P. Palm *(*2005*),* Laser pulse reflectance of the ocean surface from the GLAS satellite lidar*,* Geophys. Res. Lett.*,* 32*, L22S10, doi:*10.1029/2005GL023732.

Le Méhauté, B. (1976), *An introduction to hydrodynamics and water waves*, Springer, ISBN 0387072322.

Lehner, B. and Döll, P. (2004): Development and validation of a global database of lakes, reservoirs and wetlands. Journal of Hydrology 296/1-4: 1-22.
Liu, P.C., 1970. Some features of wind waves in Lake Michigan. Limnol. Oceanogr., 15:257-72.

Liu, Y., X.-H. Yan, W. T. Liu, and P. A. Hwang, 1997: The probability density function of the ocean surface slopes and its effects on radar backscatter. J. Phys. Oceanogr., 27, 782–797.

Liu, Y., 1996: The spectrum of gravity–capillary waves, the probability density function of ocean surface slopes and their effects on radar backscatter. Ph.D. dissertation, University of Delaware, 140 pp.

Liu, Zhishen, "Estimate of maximum penetration depth of lidar in coastal water of the China Sea", Proc. SPIE 1302, Ocean Optics X, 655 (September 1, 1990); doi:10.1117/12.21476; http://dx.doi.org/10.1117/12.21476.

Longuet-Higgins, M. S., 1963: The generation of capillary gravity waves by steep gravity waves. J. Fluid Mech., 16, 138–159.

Longuet-Higgins, M. S. (1975), On the joint distribution of the periods and amplitudes of sea waves, J. Geophys. Res., 80(18), 2688–2694, doi:10.1029/JC080i018p02688.

Menzies, R. T.*, and* D. M. Tratt *(*1997*),* Airborne lidar observations of tropospheric aerosols during the Global Backscatter Experiment (GLOBE) Pacific circumnavigation missions of 1989 and 1990*,* J. Geophys. Res.*,* 102*(*D3*),* 3701–3714*, doi:*10.1029/96JD03405.

Menzies, R.T., David M. Tratt, and William H. Hunt, "Lidar In-space Technology Experiment measurements of sea surface directional reflectance and the link to surface wind speed," Appl. Opt. **37**, 5550-5559 (1998).

Messager, M.L., Lehner, B., Grill, G., Nedeva, I., Schmitt, O. (2016): Estimating the volume and age of water stored in global lakes using a geo-statistical approach. Nature Communications: 13603. doi: 10.1038/ncomms13603.

Mironov, A. S., M. V. Yurovskaya, V. A. Dulov, D. Hauser, and C. A. Guérin (2012), Statistical characterization of short wind waves from stereo images of the sea surface, J. Geophys. Res., 117, C00J35, doi:10.1029/2011JC007860.

Mobley C D 1994 Light and water; radiative transfer in natural waters. Academic Press, San Diego, 592pp. ISBN 0125027508.

Mobley, C.D., G.F. Cota, T.C. Grenfell, R.A. Maffione, W.S. Pegau, D.K. Perovich, 1998. Modeling light propagation in sea ice. IEEE Trans. Geosci. Rem. Sens., 36(5), 1743-1749.

Montes-Hugo MA, Weidemann A, Gould R, Arnone R, Churnside JH, Jaroz E; Ocean color patterns help to predict depth of optical layers in stratified coastal waters. J. Appl. Remote Sens. 0001;5(1):053548-053548-6. doi:10.1117/1.3634055.

Moore, K.D.; Voss, K.J.; Gordon, H.R. Spectral reflectance of whitecaps: Their contribution to water-leaving radiance. *J. Geophys. Res.* **2000**, *105*, 6493-6499.

Monzon, C., Donald W. Forester, Richard Burkhart, and Jim Bellemare »View Author Affiliations, Applied Optics, Vol. 45, Issue 27, pp. 7089-7096 (2006) http://dx.doi.org/10.1364/AO.45.007089

Morel, A., B. Gentili, H. Claustre, M. Babin, A. Bricaud, J. Ras, and F. Tieche, 2007. Optical properties of the "clearest" natural waters. *Limnology and oceanography*, Vol. 52, No. 1, pp. 217-229.

Munk, Walter H. (1950), "Origin and generation of waves", *Proceedings 1st International Conference on Coastal Engineering*, Long Beach, California: ASCE, pp. 1–4, ISSN 2156-1028Munk, W. (1950). "On the wind-driven ocean circulation". *J. Meteorology* **7**: 79–93.

Munk, 1956 referenced in Fig 2-3.

Nagle and White, USGS OFR 2016-1046.

Nayegandhi, A., "Challenges in determining water surface in airborne LIDAR topobathymetry", 15th Annual JALBTCX Workshop, June 2014.

Nave, R., Georgia State University, http://hyperphysics.phy-astr.gsu.edu/hbase/Waves/watwav2.html.

Parrish, C., Magruder, L.A., Neuenschwander, A., Forfinski-Sarkozi, N., Alonzo, M., and Jasinski, M. (2019) Validation of ICESat-2 ATLAS bathymetry and analysis of ATLS's bathymetric mapping performance. *Remote Sensing,* Vol. 11, Issue 14. DOI: 10.3390/rs11141634.

Pe'eri, S., J.V. Gardner, L.G. Ward, and J.R. Morrison, 1996. The seafloor: A key factor in LiDAR bottom detection. *IEEE Transactions on Geoscience and Remote Sensing*, Vol. 5, pp. 266–1271.

Pe'eri, S., C.E. Parrish, C. Azuike, L. Alexander, and A. Armstrong, 2014. Satellite Remote Sensing as Reconnaissance Tool for Assessing Chart Adequacy and Completeness Information. *Marine Geodesy*, Vol. 37, No. 3, pp. 293-314.

Pe'eri, S., J. V. Gardner, L. Ward, and R. Morrison, The seafloor: a key factor in lidar bottom detection, IEEE Trans. Geo. Rem. Sens., Vol. 49, No. 3, 2011.

Pe'eri, S., Lynnette V. Morgan, William D. Philpot, and Andrew A. Armstrong (*2011*) Land-Water Interface Resolved from Airborne LIDAR Bathymetry (ALB) Waveforms. Journal of Coastal Research: Special Issue 62: pp. 75 – 85.

Peterson, T. C., *et al.,* Recent changes in climate extremes in the Caribbean region, J. Geophys. Res., 107(D21*), 4601, doi:*10.1029/2002JD002251, 2002.

Petzold, T.J., (1972) Volume Scattering Functions for Selected Ocean waters. SI) Ref. 72-78, Scripps Inst Ocean., Visibility Lab., San Diego, Calif., 79 pp.

Plant, W. J. (1982), A relationship between wind stress and wave slope, J. Geophys. Res., 87(C3), 1961–1967, doi:10.1029/JC087iC03p01961.

Plant, W. J., A new interpretation of sea-surface slope probability density functions, J. Geophys. Res., 108 (C9), 3295-3298, 2003.

Ross, V., and D. Dion (2007), Sea surface slope statistics derived from Sun glint radiance measurements and their apparent dependence on sensor elevation, J. Geophys. Res., 112, C09015, doi:10.1029/2007JC004137.

Rowland, J. C.*, et al. (*2010*),* Arctic Landscapes in Transition: Responses to Thawing Permafrost*,* Eos Trans. AGU*,* 91*(*26*),* 229–230*, doi:*10.1029/2010EO260001.

Sathyendranath, S., L. Lazzara, and L. Prieur, Variations in the spectral values of specific absorption of phytoplankton, Limnol. Oceanogr., 32, 403-415, 1987.

Serreze, M. C., Walsh, J. E., Chapin, F. S. III, Osterkamp, T., Dyurgerov, M., Romanovsky, V., Oechel, W. C., Morison, J., Zhang, T. and Barry, R. G. (2000) Observational evidence of recent change in the northern high-latitude environment. Clim. Change, 46, pp. 159–207.

Su W, Charlock TP, Rutledge K., Observations of reflectance distribution around sunglint from a coastal ocean platform. Appl Opt. 2002 Dec 10; 41(35):7369-83.

Tayfun, M. A., 1980. Narrow-band nonlinear sea waves. J. Geophys. Res., 85, 1548-1552.

Tratt, D.M., Robert T. Menzies, Meng P. Chiao, Dean R. Cutten, Jeffry Rothermel, R. Michael Hardesty, James N. Howell, and Stephen L. Durden, "Airborne Doppler lidar investigation of the wind-modulated sea-surface angular retroreflectance signature," Appl. Opt. **41**, 6941-6949 (2002).

Wright, C. W., E. J. Walsh, D. Vandemark, W. B. Krabill, A. W. Garcia, S. Houston, M. Powell, P. Black, and F. D. Marks, 2001: Hurricane directional wave spectrum spatial variations in the open ocean. J. Phys. Oceanogr., 31, 2472-2488.

Wozniak, S. B., AND D. Stramski. 2004. Modeling the optical properties of mineral particles suspended in seawater and their influence on ocean reflectance and chlorophyll estimation from remote sensing algorithms. Appl. Opt. 43:3489–3503.

Wright, C.W., 2014. USGS EAARL-B: Missions, Calibration & Validation. 15th Annual JALBTCX Airborne Coastal Mapping and Charting Workshop, Mobile, AL, 10-12 June: http://shoals.sam.usace.army.mil/Workshop_Files/2014/Day2_pdf/1500_Wright.pdf (last date accessed: 06 Feb, 2015).

Wu, J.: Mean square slopes of the wind-distributed water surface, their magnitude, directionality, and composition, Radio Sci., 25, 37-48, 1990.

Young et al, 1994

Yurovskaya, M. V., V. A. Dulov, B. Chapron, and V. N. Kudryavtsev (2013), Directional short wind wave spectra derived from the sea surface photography, J. Geophys. Res. Oceans, 118, 4380–4394, doi:10.1002/jgrc.20296.

Zaneveld, 2011

Zhang G, Xie H, Kang S, Yi D and Ackley S F 2011 Monitoring lake level changes on the Tibetan Plateau using ICESat altimetry data (2003–2009) Remote Sens. Environ. 115, 1733–42.

Zhang, G.; Hongjie Xie ; Shuiqiang Duan ; Mingzhong Tian and Donghui Yi "Water level variation of Lake Qinghai from satellite and in situ measurements under climate change", J. Appl. Remote Sens. 5(1), 053532 (June 28, 2011). ; http://dx.doi.org/10.1117/1.3601363.

Zhang and Wang, Evaluation of sunglint models using MODIS measurements, J. Quant Spec & Radia. Trans 111(2010) 492-506.